RAMAN-ENCODED NANOPARTICLES FOR BIOMOLECULAR DETECTION AND CANCER DIAGNOSTICS

A Dissertation
Presented to
The Academic Faculty

by

Dominic O. Ansari

In Partial Fulfillment
Of the Requirements for the Degree
Doctor of Philosophy in Bioengineering

Georgia Institute of Technology

December 2008

RAMAN-ENCODED NANOPARTICLES FOR BIOMOLECULAR DETECTION AND CANCER DIAGNOSTICS

Approved by:

Dr. Shuming Nie, Advisor
Department of Biomedical Engineering
Georgia Institute of Technology and Emory University

Dr. Eberhard O. Voit
Department of Biomedical Engineering
Georgia Institute of Technology and Emory University

Dr. Cheng Zhu
Department of Biomedical Engineering
Georgia Institute of Technology and Emory University

Dr. Charles A. Parkos
Department of Pathology and Laboratory Medicine
Emory University

Dr. John A. Petros
Department of Urology
Emory University

Date Approved: September 16, 2008

To Mom, Dad, Alex, and Aki

ACKNOWLEDGEMENTS

First, I thank my advisor Dr. Shuming Nie for providing the support and academic freedom to pursue answers to interesting questions. I have learned much about scientific research and about life from him. I will always remember Shuming as a brilliant mentor who pushed me to my limits and helped me to understand that to know thyself is to know the world.

I also express my gratitude to my committee. I especially acknowledge Dr. Chuck Parkos whose support and advice has helped me grow as a budding scientist and physician. I thank Dr. John Petros, Dr. Eberhard Voit, and Dr. Cheng Zhu for their stimulating discussions and helpful insights over the years.

Next I convey my appreciation to the Nie research group members past and present for offering their insights and constructive criticism and help with experiments, especially Dr. Ximei Qian, Dr. Doug Stuart, Dr. Yun Xing, and Dr. Xiaohu Gao. I also want to mention Dr. Gloria Kim, Dr Gang Ruan, and Dr. Tushar Sathe for some great times at events ranging from potlucks to skydiving. Additional gratitude goes to MD/PhD students Eric Severson, Winston Lee, and Chris Corso for helpful comments that helped to shape this dissertation.

I am fortunate to have family and friends that have given me constant support and encouragement. I am especially grateful to my parents for their selfless love and

for instilling in me a sense of curiosity and an optimistic view of life. My magnificent brother Alex stimulates my creativity and keeps me grounded in the real world. Finally, my beautiful and extremely talented wife Aki has helped me remain focused and determined to achieve my goals while keeping a broad perspective on what is important in life. I thank her infinitely for her love and patience and look forward to our future together.

TABLE OF CONTENTS

LIST OF TABLES

LIST OF FIGURES

Page

LIST OF SYMBOLS AND ABBREVIATIONS

SYMBOLS

^{o}C	degree(s) Celsius
λ	wavelength
λ_{max}	wavelength of maximal optical absorption
λ_{SPR}	peak wavelength of surface plasmon resonance
$\Delta\upsilon$	frequency shift
$\overline{x}$	mean of x
σ_x	standard deviation of x
$\mathbf{x}$	the vector x
$\mathbf{Y}$	the matrix y
$\mathbf{x} \bullet \mathbf{Y}$	the dot product of x and y
$\mathbf{Y}^{\mathbf{T}}$	the transpose of y
$\mathbf{Y}^{\mathbf{-1}}$	the inverse of y

ABBREVIATIONS

7-AAD	7-amino-actinomysin

Ag	silver
AgNP	silver nanoparticle
Au	gold
AuNP	gold nanoparticle
A-PRENT	antibody conjugated PRENT
BBI	British Biocell International
BBS	bicarbonate buffered saline
BSA	bovine serum albumin
CCD	charge-coupled device
CE	chemical enhancement
COIN	composite organic inorganic nanoparticle
DLS	dynamic light scattering
DTNB	5-5′′-Dithio-*bis*(2-nitrobenzoic acid)
EFE	electromagnetic field enhancement
EIA	enzyme immunoassay
ELISA	enzyme-linked immunosorbent assay
EpCAM	epithelial cell adhesion molecule
FLISA	fluorescence-linked immunosorbent assay
FFPE	formalin-fixed paraffin-embedded
GAN	glass-coated analyte tagged nanoparticle
GOPS	3-glycidyloxypropyltrimethoxysilane
HOMO	highest occupied molecular orbital
HRP	horseradish peroxidase

ICC	immunocytochemistry
IHC	immunohistochemistry
IgG	immunoglobulin G
IgG-PEG-SH	IgG conjugated to PEG-SH
IR	infrared
ISA	immunosorbent assay
LOD	limit of detection
LOQ	limit of quantification
LSPR	localized surface plasmon resonance
LUMO	lowest unoccupied molecular orbital cv
ME	2-mercaptoethanol
MW	molecular weight
NHS	N-hydroxysuccinimide
NIR	near-infrared
NP	nanoparticle
PBS	phosphate buffered saline
PBS-T	0.05% Tween-20 in PBS
PEG	polyethylene glycol
PEG-NH_2	aminated polyethylene glycol
PEG-SH	thiolated polyethylene glycol
PEO	polyethylene oxide
PRENT	polymer-protected Raman-encoded nanoparticle tag
PRP	plasmon resonant metal nanoparticle

PVDF	polyvinylidene fluoride
AV-PE	Annexin V-Phycoerythrin
QD	semiconductor quantum dot
RIA	radio-immunoassay
RLISA	Raman-linked immunosorbent assay
RNR	reporter-to-nanoparticle ratio
RRS	resonance Raman scattering
SERS	surface-enhanced Raman scattering
SERRS	surface enhanced resonance Raman scattering
SG-AuNPs	Au NPs synthesized by seeded growth method
SNR	signal-to-noise ratio
SPR	surface plasmon resonance
TEM	transmission electron microscopy
UV	ultraviolet
v/v	volume by volume
vis	visible
w/v	weight by volume

SUMMARY

Assays that can quantify and localize disease-associated molecular biomarkers in biological substrates are important in both basic sciences and clinical medicine. Tagging biomarkers with targeted and optically encoded materials that generate light with distinct spectroscopic features not present in the biological substrate is an established and robust detection strategy. Optical assays are commonly performed with antibody-targeted organic dye contrast agents but the potential for precise quantification, long-term imaging, and multiplexed readouts is limited by chemical and optical instability, non-optimal spectral characteristics, and complicated synthetic chemistry of the dyes. Recent advances have provided the ability to precisely and reproducibly control the geometry and surface chemistry of nanometer-scale metal particles as well as a microscopic understanding of the effects of those manipulations on optical properties. When combined with a molecular insight of disease processes, these nanostructured materials have the potential to address the limitations of traditional technologies.

In this work we tested the hypothesis that a new class of optical tag termed polymer-protected Raman-encoded nanoparticle tags (PRENTs) confers advantages over existing optical technologies for practical molecular diagnostic applications. First, we developed a set of PRENTs through an efficient and modular design utilizing gold-nanoparticle-Raman reporter complexes protected and functionalized by polyethylene glycol

derivatives. The PRENTs provided optical readouts through surface enhanced Raman scattering (SERS) that were nearly two orders of magnitude brighter and more resistant to photodegradation than the fluorescence of semiconductor quantum dots under identical experimental conditions. We generated six distinct spectral signatures with a broader class of Raman reporters than is possible with silica coated SERS tags. Irreversible spectral changes and aggregation of PRENTs did not occur when subjected to harsh chemical conditions that can cause uncontrolled spectral changes and aggregation of dyes, quantum dots, and protein coated SERS tags. PRENTs were readily functionalized with antibodies and provided specific targeting and Raman spectral detection of cell surface biomarkers on living cancer cells at reasonable integration times. PRENTs were non-toxic to cells under conditions exceeding those required for sensitive molecular detection.

Second, we demonstrated that core nanoparticle geometry and molecular resonance could be used to improve brightness and peak intensities at a near-infrared excitation wavelength. In addition, adjusting the ratio of Raman reporters to nanoparticles in the initial step of PRENT preparation provided a fine adjustment of intensity over a wide range without causing a large change in aggregation state. A set of six NIR-PRENTs with distinct Raman spectral signatures was developed and further optimized for specific biological applications through the size-dependent Raman enhancement of gold nanoparticles.

Third, we developed a slide-based Raman-linked immunosorbent assay and demonstrated that antibody-conjugated PRENTs can quantify proteins with a limit of detection in the low ng/mL range. Three different antibody conjugation methods were evaluated in a bead-based immunoassay and the optimal one selected for further assay development. We used the RNR as a unique signal normalization procedure for PRENTs and showed that samples containing mixtures of different PRENTs could be unmixed into their relative concentrations with simple ordinary least squares modeling. Taken together, our results suggest that PRENTs have advantages useful for a broad array of applications in analytical chemistry, molecular biology, and cancer diagnostics, and provide insights for further assay development.

CHAPTER I

INTRODUCTION

1.1 Motivation

Assays that sense the presence, quantity, or location of specific disease-relevant biomolecules in biological substrates (e.g. cells, tissues, body fluids) are important in both basic sciences and clinical medicine. The most robust analytical assays detect biomolecules by tagging them with materials that generate a radioactive, electrical, or optical signal. Detecting the biomolecules directly is usually not practically feasible because of their low contrast from the surrounding substrate. Optical assays, in particular, provide an optimized combination of speed, sensitivity, robustness, and safety. An optically encoded tag is a material that generates light with distinct spectroscopic characteristics that are ideally not present in the detection substrate. The tags are directed to specific biomolecules by firmly attaching them to targeting ligands such as antibodies or nucleic acids. The most common optically encoded tags in use are organic molecules possessing strong light absorption (chromophores) or strong fluorescence (fluorophores). Absorbance based (e.g. colorimetric) assays using chromophores are widely used in diagnostic surgical pathology because they require relatively simple instrumentation, generate less background signal from formalin-fixed tissue specimens, and integrate well within the workflow of traditional morphologic analysis.[1] Because the amount of light detected is decreased with increasing tag concentration or in the presence of multiple

tags, absorbance assays have a dynamic range that is far below the range of protein expression exhibited by biological samples and are not ideally suited for quantification.[2-4] Multiplexed analysis, the simultaneous detection of multiple tagged biomolecules, is highly desirable in cases where there is a limited quantity of biological substrate, such as in needle biopsy, or where assay turnaround time is critical. The subtractive nature of absorbance assays and the broad, unstable, and overlapping nature of chromophore spectra severely limit multiplexed analysis. Although simultaneous staining of up to four colors has been demonstrated, precise quantification of tag signals is not available even under the most ideal conditions.[5] Organic dye fluorophores are the tag of choice in flow cytometry, immunosorbent assay, *in vivo* molecular imaging and most other fields of analysis because they are widely commercially available and produce bright readouts. Fluorescence assays are additive in nature but they suffer from the limited optical and chemical stability of organic dyes that can adversely affect quantitative analysis and long-term imaging.[6-8] The number of fluorescent tags that can be simultaneously resolved is further limited by the narrow excitation spectra and broad emission spectra inherent to organic dyes. Synthesis of novel organic dyes requires highly specialized expertise. There are few commercially available dyes efficiently excited at the longer light wavelengths (i.e. near-infrared) that can maximize signal-to-noise ratios in most biological tagging assays.[9,10] Moreover, each organic chromophore or fluorophore requires customized chemistry for conjugation to targeting ligands.

Recent advances in the physical sciences have provided nanostructured materials with unique optical properties that can address the limitations of traditional fluorophores and chromophores. Although the synthesis and applications of materials with dimensional

features on the 1 to 100 nm scale are not new,[11] the reproducible, and precise control of size and shape and the in depth experimental characterization of their effect on optical properties is a recent development and an ongoing area of intense research.[12-16]

1.2 Scope and organization

In this dissertation, we describe the development and characterization of a novel optical tagging technology composed of nanometer scale materials. Our overall *hypothesis* is that polymer-protected Raman-encoded nanoparticle tags (PRENTs), hybrid inorganic-organic nanomaterials protected and functionalized by polyethylene glycol derivatives and producing Raman spectroscopic readouts, have advantages over traditional optical technologies for practical molecular diagnostic applications. This dissertation has been divided into six chapters. Chapter 2 provides the background in surface enhanced Raman scattering and recent developments in nanostructured optical tags (quantum dots, plasmon resonant particles, and SERS tags) necessary to understand the questions, experiments, and conclusions in Chapters 3, 4, and 5. Chapter 3 describes the initial development and characterization of PRENTs, Chapter 4 reports the optimization of PRENTs for near-infrared excitation and detection, and in Chapter 5, we report the development of a quantitative Raman immunoassay using PRENTs, optimization of bioconjugation, and a brief demonstration of multiplexed detection. Finally, in Chapter 6 we recap with a brief summary of the conclusions of this dissertation and discuss future directions that did not fall within the scope of this work.

1.3 References

1. Taylor, C.R. and R.M. Levenson, *Quantification of immunohistochemistry - issues concerning methods, utility and semiquantitative assessment ii.* Histopathology, 2006. **49**(4): p. 411-424.

2. Rimm, D.L., *What brown cannot do for you.* Nature Biotechnology, 2006. **24**(8): p. 914-916.

3. McCabe, A., et al., *Automated quantitative analysis (aqua) of in situ protein expression, antibody concentration, and prognosis.* Journal of the National Cancer Institute, 2005. **97**(24): p. 1808-1815.

4. Cregger, M., A.J. Berger, and D.L. Rimm, *Immunohistochemistry and quantitative analysis of protein expression.* Archives of Pathology & Laboratory Medicine, 2006. **130**(7): p. 1026-1030.

5. van der Loos, C.M., *Multiple immunoenzyme staining: Methods and visualizations for the observation with spectral imaging.* J. Histochem. Cytochem., 2008. **56**(4): p. 313-328.

6. Goldman, R.D. and D.L. Spector, eds. *Live cell imaging*. 2005, Cold Spring Harbor Library Press: Cold Spring Harbor, NY.

7. Tsurui, H., et al., *Seven-color fluorescence imaging of tissue samples based on fourier spectroscopy and singular value decomposition.* Journal of Histochemistry & Cytochemistry, 2000. **48**(5): p. 653-662.

8. Johnson, I., *Fluorescent probes for living cells.* Histochemical Journal, 1998. **30**(3): p. 123-140.

9. Patonay, G. and M.D. Antoine, *Near-infrared fluorogenic labels - new approach to an old problem.* Analytical Chemistry, 1991. **63**(6): p. A321-A326.

10. Frangioni, J.V., *In vivo near-infrared fluorescence imaging.* Current Opinion in Chemical Biology, 2003. **7**(5): p. 626-634.

11. Faulk, W.P. and G.M. Taylor, *Immunocolloid method for electron microscope.* Immunochemistry, 1971. **8**(11): p. 1081-&.

12. Rosi, N.L. and C.A. Mirkin, *Nanostructures in biodiagnostics.* Chem. Rev., 2005. **105**(4): p. 1547-1562.
13. Penn, S.G., L. He, and M.J. Natan, *Nanoparticles for bioanalysis.* Current Opinion in Chemical Biology, 2003. **7**(5): p. 609-615.
14. Alivisatos, P., *The use of nanocrystals in biological detection.* Nature Biotechnology, 2004. **22**(1): p. 47-52.
15. Smith, A.M., et al., *Bioconjugated quantum dots for in vivo molecular and cellular imaging.* Advanced Drug Delivery Reviews, 2008. **60**: p. 1226-1240.
16. Wilson, R., *The use of gold nanoparticles in diagnostics and detection* Chemical Society Reviews, 2008.

CHAPTER 2

BACKGROUND

2.1 Optically encoded nanoparticle tags

The past decade has witnessed a rapid increase in molecular detection and diagnostic technologies utilizing inorganic nanoparticle (NPs). Metal and semiconductor colloidal NPs are of considerable interest because of their size, shape, and composition dependent optical properties and their dimensional similarities with biological macromolecules. When successfully protected and targeted, NP tags can improve the sensitivity, quantitative capabilities, and the throughput of biomolecular detection in a variety of formats when compared with conventional fluorescent and colorimetric probes. The development and biological application of quantum dots, plasmon resonant particles, and surface enhanced Raman tags have recently become an area of especially intense investigation. For all three technologies, an ongoing challenge is the development of surface chemistries that can simultaneously confer protection of NP stability and optical properties in biocompatible buffers and provide a stable linkage to targeting ligands with affinity to specific biomolecules.

2.2 Quantum dots

Quantum dots (QDs) are semiconductor NPs that exhibit size-dependent fluorescence excitation and emission spectra. Broad excitation spectra, narrow Gaussian-shaped emission spectra, brightness, and photostability have made QDs a popular choice as optical tags.

Semiconductors are typified by a finite energy gap (the bandgap) between a valence band, the highest energy level occupied by electrons at room temperature, and a conduction band, the lowest unoccupied electronic energy level (**Figure 2.1**). Absorption of a photon with sufficient energy can excite a negatively-charged electron to enter the conduction band and leave behind a positively charged hole in the valence band. Fluorescence occurs when the conduction band electron relaxes back to its ground state and recombines with a hole in the valence band, emitting a photon with the same energy as the bandgap. When one or more dimensions of the semiconductor are reduced to nanometer scale, the bandgap becomes size dependent in a phenomenon known as the "quantum confinement effect."[1] QDs are semiconductors with all three spatial dimensions in the nanometer size regime and their excitation and emission spectra shift to longer wavelengths (decreased energy) with increasing size (**Figure 2.2**).

Over the past thirty years, QDs have matured from an object of curiosity among a specialized group of physicists to a powerful research tool in a variety of disciplines spanning from optoelectronics to animal physiology. Early synthetic preparations of QDs

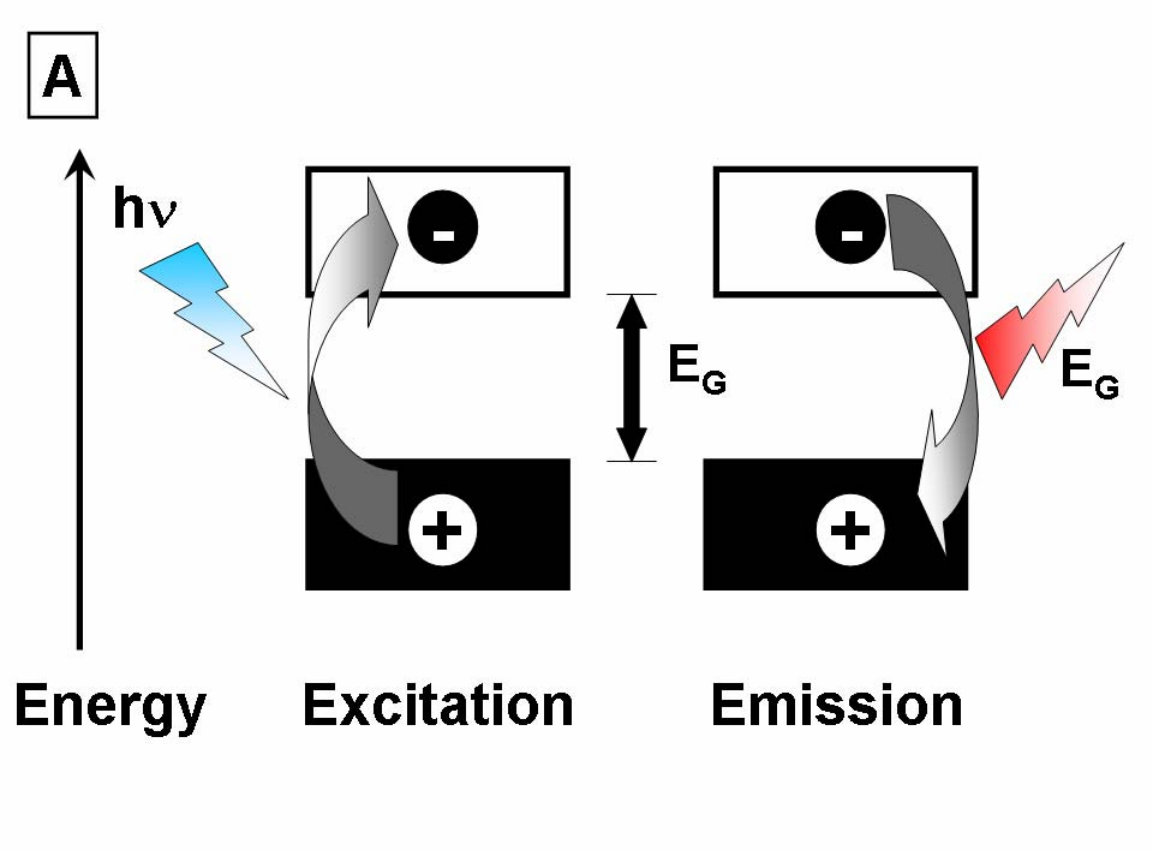

Figure 2.1: Schematic diagram of semiconductor photoluminescence. The shaded lower box represents the valence band and the unshaded upper box represents the conduction band. The space between the valence and conduction bands represents the bandgap energy $\mathbf{E_G}$. Fluorescence in semiconductors is depicted in two steps. Absorption of a photon of energy equal to or greater than that of the bandgap excites a negatively charged electron to enter the conduction band, leaving behind a positively charged hole in the valence band (**Excitation)**. A conduction band electron may relax back to its ground state by recombining with a hole, resulting in the emission of a photon with the same energy as the bandgap (**Emission**).

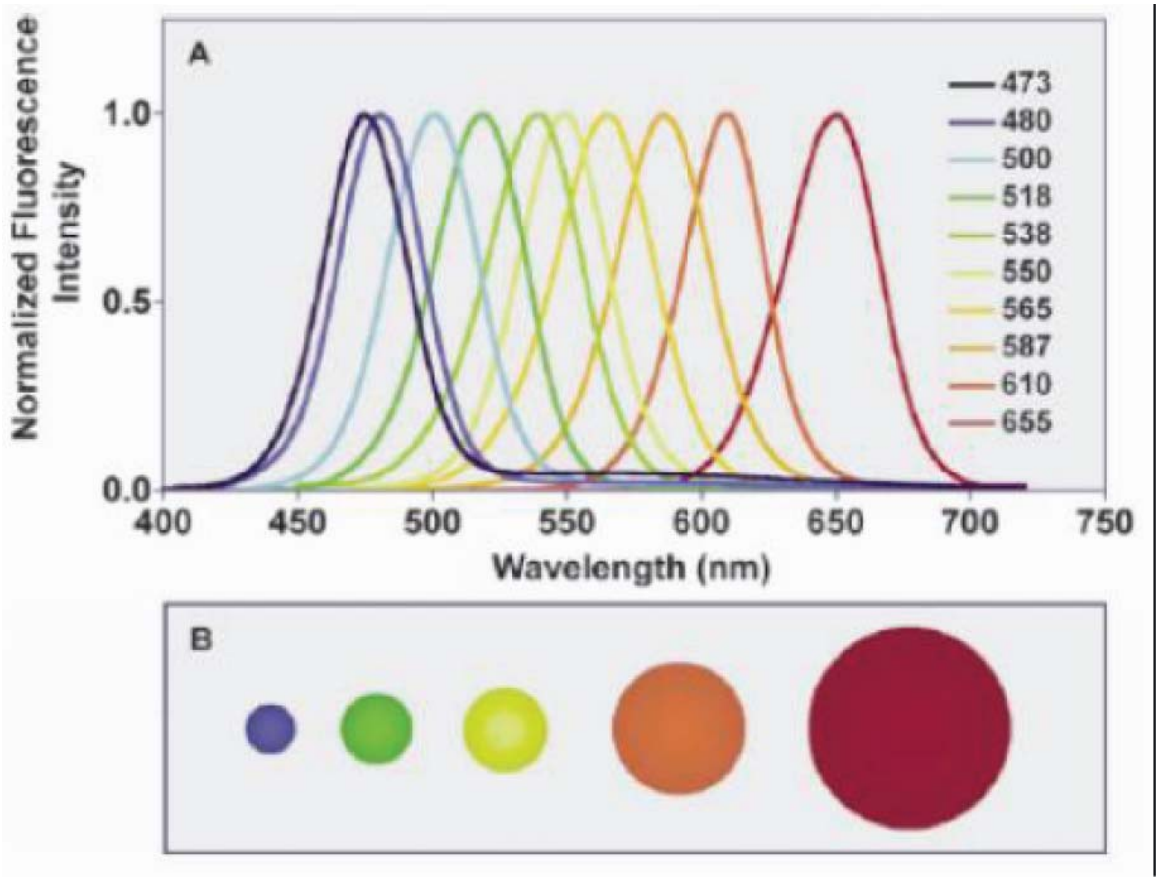

Figure 2.2: Size-tunable fluorescence emission of quantum dots. Fluorescence emission spectra of CdSe-ZnS quantum dots with increasing particle diameters Reprinted from Reference 2. © Royal Society of Chemistry

fell short of their theoretical potential due to poor fluorescence efficiencies and large size variations. In 1993, the introduction of cadmium selenide (CdSe) as a QD synthetic material enabled production of QDs with narrow size distribution and took full advantage of the size-dependent optical properties.[3] Because QDs have a long fluorescence lifetime and a large fraction of surface defects, they are prone to photochemical degradation. A major advance was the introduction of a core shell structure, with the shell material possessing a larger bandgap that confined the excitation to the core.[4-6] Core-shell QDs exhibit dramatically increased chemical stability, photoluminescence efficiency, and optical stability to prolonged illumination. However, these QDs are insoluble in water and therefore not suitable for biological applications. In 1998, two research groups independently reported procedures for rendering QDs water soluble and functionalized them with targeting ligands while retaining their optical properties.[7,8] These initial reports gave way to a dramatic increase in research aimed at further developing QDs specifically for biomolecular detection and imaging. QDs have been demonstrated as optical tags in numerous applications including fluorescence-linked immunosorbent assay (FLISA),[9-12] dynamic tracking of cell surface membrane receptors,[13,14] quantitative immunohistochemistry,[15-17] and *in vivo* tumor targeting and imaging.[18-20] Examples of quantum dot immunolabeling applications are shown in **Figure 2.3**. Key limitations of QDs for biological applications are the lack of high quality QDs that are efficiently excited at longer wavelengths and the potential toxicity of QDs.

2.3 Plasmon resonant particles

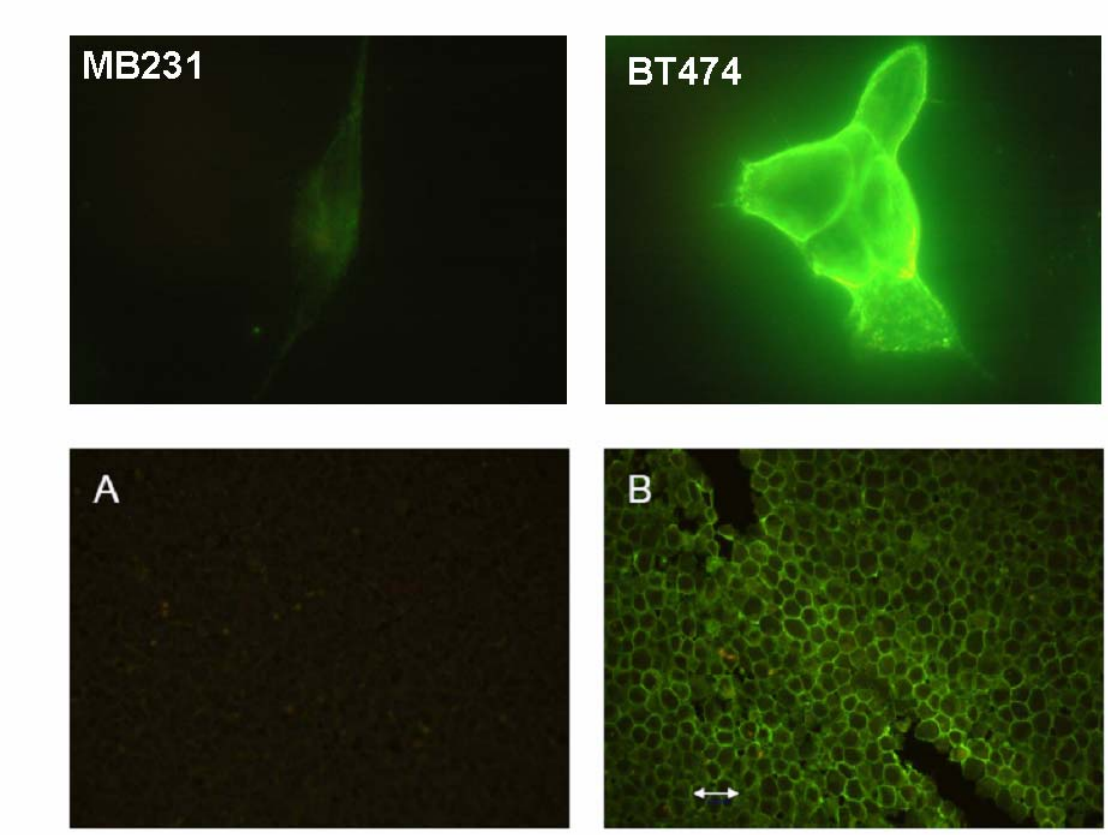

Fig 2.3: Quantum dot antibody conjugates for sensitive immunolabeling. Top panels: Fluorescence micrographs of optimally fixed **MB231** (low Her2 expression) and **BT474** (high Her2 expression) breast carcinoma cells labeled with Anti-Her2 IgG functionalized quantum dots. Images were taken under the same illumination conditions. **Bottom** panels: Fluorescence micrographs of sectioned formalin-fixed paraffin-embedded BT474 cells labeled with quantum dot-secondary antibody conjugates without a primary antibody **(A)** or after incubation with a Her2 primary antibody. Images A and B were taken under the same illumination conditions. (Ansari and Nie, unpublished data)

Plasmon resonant particles (PRPs) are 30-120 nm diameter gold (Au) or silver (Ag) NPs that scatter colored light when excited with white light. The scattering of a single 80 nm PRP can be as bright as the fluorescence of 10^5 QDs or 10^3 dye-doped beads (100 nm diameter).[21] PRPs exhibit robust photostability as a fundamental property. Scattering occurs incident light induces oscillations of electron distributions within the PRP, which in turn re-emits light in a random direction. Like QDs, PRPs can be size-tuned for emission of specific colors (wavelength bands) but their size-dependent optical effects are different in origin from QD optical properties.

In contrast to semiconductors, metals possess a single conduction band and lack a valence band or band gap. Metals are typically modeled as a three dimensional crystals of positively charged atomic cores encapsulated by a "sea" of mobile conduction electrons. When the size of the metal object is smaller than the wavelength of incident light (i.e. nanometer sized particles), the light can induce the conduction electrons to oscillate as a collective group across the metal surface.[22] The oscillations are called surface plasmons. Surface plasmons from monodisperse NPs are typified by a narrow range of resonance frequencies at which they absorb and scatter light most efficiently, a property well-explained by classical electromagnetic theory.[23-25] The frequency band of surface plasmon resonance (SPR) is strongly dependent on the NP material composition, size, shape, aggregation state, and surrounding environment.[26-30] For homogeneous spherical NPs much smaller than the incident light wavelength, both the scattering efficiency and the peak scattering wavelength increase with size.[31]

Ag and Au are used as materials for PRPs because they can satisfy the SPR condition at the visible excitation wavelengths (400-700 nm) commonly employed for biological detection and imaging.[30] Although methods for preparing Au and Ag NPs are well-established,[32-34] reproducible synthesis of monodisperse NPs at the size range required for efficient SPR remains a major challenge. For multiplexed biological assays, it is critical that PRP preparations be as homogeneous as possible with respect to size, shape, and composition and possess narrow scattering bandwidths. Recent advancements in seeded growth methods have yielded convenient procedures for fabricating monodisperse spherical and rod-shaped NPs useful as PRPs.[35-38] Another innovative synthetic approach is the growth of a thin layer of Au or Ag onto a dielectric (silica or latex) nanoparticle to form a "nanoshell." PRP.[29,39] In the nanoshell methodology, the SPR frequency can be tuned throughout the visible and near-infrared (NIR) spectral region by changing the relative dimensions of dielectric core and metal shell (**Figure 2.4**).[40]

In contrast to QDs, high quality PRPs can be synthesized in aqueous solution and are stable for months under ambient conditions. As prepared, PRPs are typically stabilized in solution by loosely-associated charged surface ligands. Thus, PRPs rapidly aggregate in ionic solutions such as assay buffers and cell culture media due to screening of the surface charges. In addition the PRP surfaces are subject to fouling by serum proteins, genomic DNA, and other non-specific biomolecules that do not serve a defined purpose in the tagging assay. A surface coating must be used to protect the PRP from aggregation and non-specific binding and be compatible with methods of attaching biomolecular

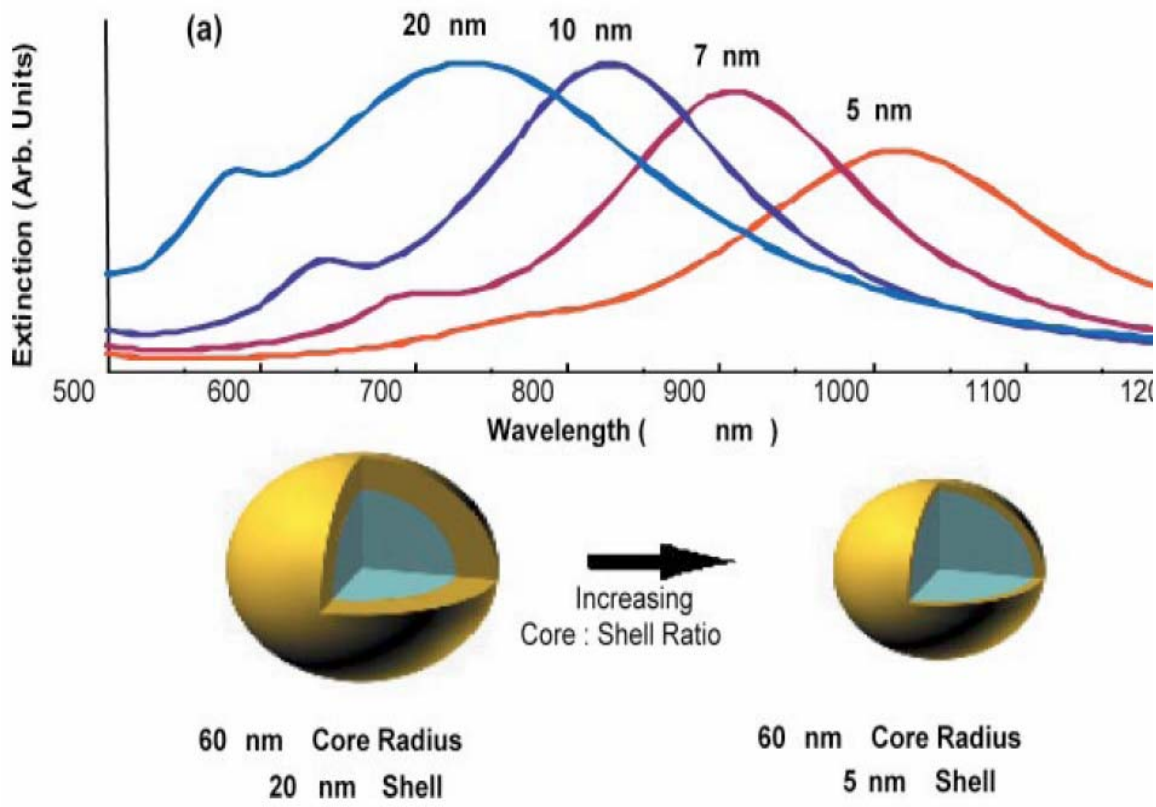

Figure 2.4: Size-tunable optical properties of nanoshell plasmon resonant particles (PRPs). Top: Extinction (sum of scattering and absorbance) spectra for nanoshell PRPs with a silica core of 60 nm radius and a gold shell thickness of 20 nm (cyan), 10 nm (dark blue), 7 nm (red), and 5 nm (orange). **Bottom**: Schematic diagram of nanoshell PRP structure. Reprinted from Reference 40. © Annual Reviews.

targeting ligands. Strategies for coating PRPs include simultaneous protection and targeting with proteins[41-43] or nucleic acids[44,45] and coating prior to targeting using silica,[46,47] carbohydrates,[48-50] or synthetic polymers.[51] Successful biological detection and diagnostic applications using PRPs as optical tags include DNA detection on microarrays,[52,53] imaging and counting of single molecular targets,[21,54] cell tagging for flow cytometry,[55] and combined imaging and photothermal ablation of live cancer cells (**Figure 2.5**).[56,57]

2.4 Surface enhanced Raman scattering tags

Surface enhanced Raman scattering tags (SERS tags) are hybrid inorganic-organic nanostructures that produce Raman scattered light when excited with monochromatic light. The attraction of SERS tags for biological application stems from fundamental photostability, a simple mechanism of generating a multitude of unique spectral signatures, and excitation at any light wavelength. SERS tags share with PRPs a common origin in the localized surface plasmons of metal NPs but additional mechanisms contribute to their unique optical properties.

Raman scattering

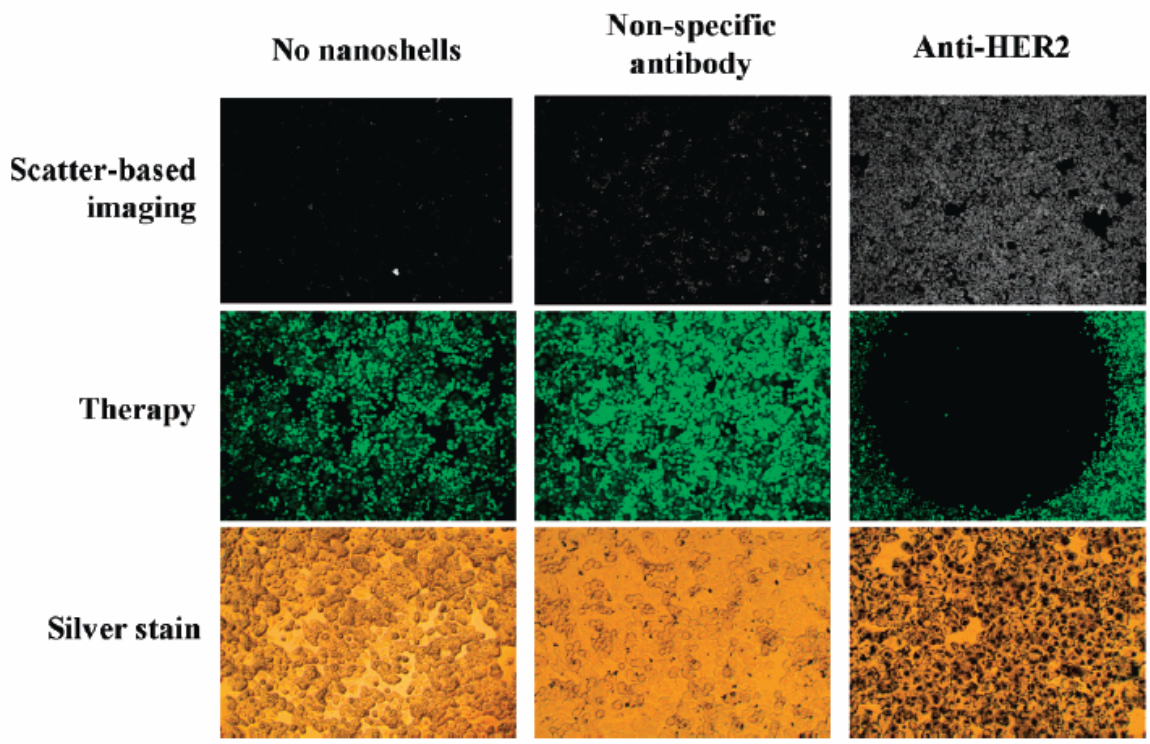

Figure 2.5. PRPs for combined imaging and therapy. Combined imaging and therapy of SK-BR3 breast cancer cells using Her2-targeted nanoshell PRPs. Darkfield micrographs of Her2 immunolabeling (top row), cell viability after near-infrared laser treatment and calcein staining (middle row), and brightfield micrographs of Her2 immunolabeling after silver staining (bottom row). Reprinted from Reference 56. © American Chemical Society

Light that is incident upon a molecule can be transmitted, absorbed, or scattered. Transmission occurs when the incident light does not interact with the molecule and passes straight through it. If the energy of a photon of the incident light matches the energy gap between the ground state of a molecule and an electronically excited state, absorption occurs. Scattering takes place when the oscillating electric and magnetic fields of the incident light cause oscillations of electron distributions within the molecule, that in turn re-emit light in a random direction (**Figure 2.6A**). Scattering differs from fluorescence and infrared absorption (IR) spectroscopy in that the incident light energy does not need to correspond with the energy of an electronic or vibrational transition. Electron cloud distortion induced by scattering changes the molecule's energy level to a "virtual state" that is determined by the frequency of the incident light energy (**Figure 2.6B**). In most cases the molecule rapidly returns to the same vibrational energy level from which it started. Thus, the vast majority of the scattered light has the same energy as the incident light and is known as elastic or Rayleigh scattering. Elastic Rayleigh (Mie) scattering is the type of scattering detected in PRP tagging assays. If nuclear motion is induced along with the electron cloud distortion, energy will be transferred from the incident photon to the molecule or vice versa and Raman scattering occurs.[58] The Raman scattering process is far less efficient than Rayleigh scattering, with typically 1 Raman scattered photon per 10^8-10^{10} incident photons. In most cases the Raman scattering process leads to an increase of energy by the molecule and the release of a photon with lower energy than the incident photon (Stokes Raman scattering). If the molecule is in a vibrationally excited state due to thermal energy, it may release energy to the Raman scattered photon (Anti-Stokes Raman scattering). The work in this

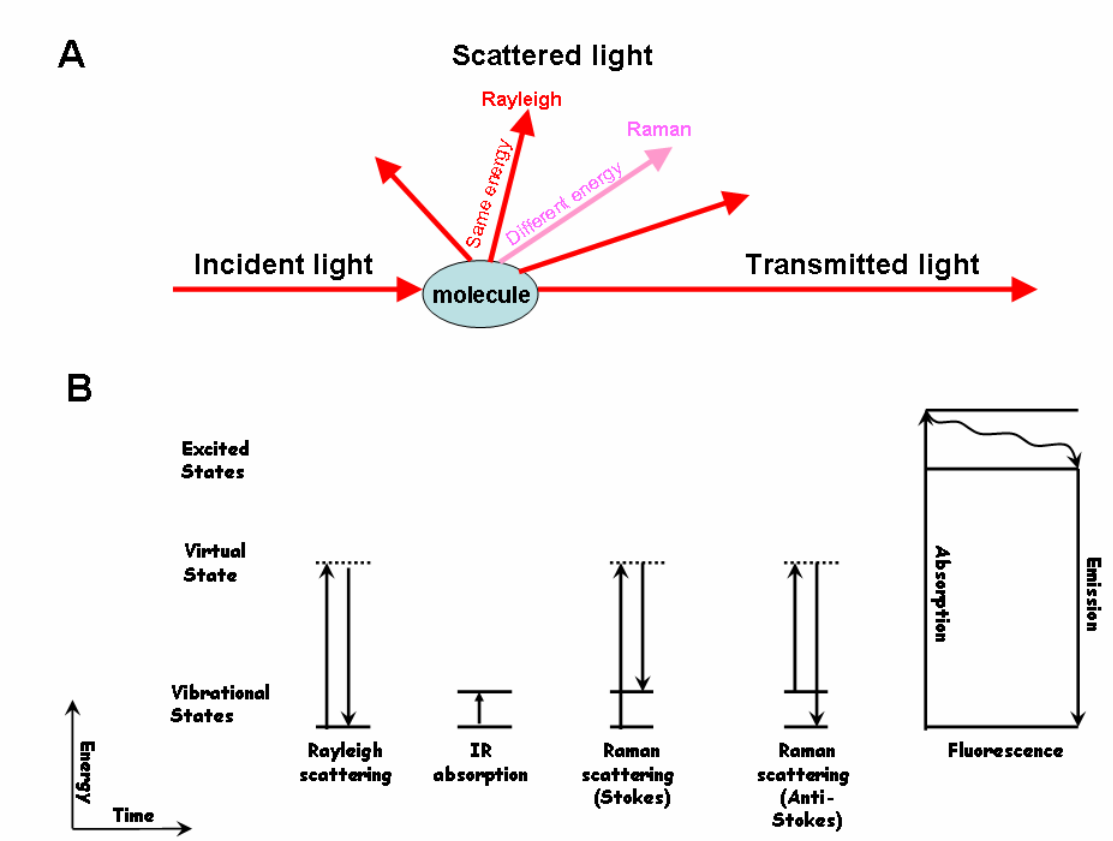

Figure 2.6: Interactions between photons and molecules. Schematic diagram of various interactions of a molecule with monochromatic light (**A**). Molecular energy diagram comparing Rayleigh scattering, infrared absorption, Raman scattering (Stokes and anti-Stokes), and fluorescence (**B**).

dissertation and from other SERS tag publications exclusively measures Stokes Raman scattering and the term "Raman scattering" is henceforth used as shorthand.

Conventionally, Raman spectra are reported as a plot of Raman scattering intensity as a function of "Raman shift" (**Figure 2.7**). The Raman shift is the difference in the energy of the excitation photons and the energy of Raman scattered light.

The traditional energy unit of the Raman shift is wavenumber, or the number of waves per centimeter (cm^{-1}). The absolute wavenumber is the reciprocal of the wavelength. Raman shift can be readily converted to wavelength by calculating

$$\lambda_{RS} = \frac{10^7}{\left(\frac{10^7}{\lambda_{ex}}\right) - \Delta\nu} \quad (1)$$

Here, λ_{RS} is the wavelength of the Raman scattering in nm, $\Delta\upsilon$ is the Raman shift in cm^{-1}, and λ_{ex} is the excitation wavelength in nm

Surface enhanced Raman scattering

The specificity of normal Raman scattering makes it a powerful molecular identification technique, but the signals are too weak for sensitive quantitative analysis at the ultra-low concentrations encountered in biological samples. Tagging the biomolecules with compounds possessing strong Raman cross-sections does not ameliorate this problem.[59] In the mid-1970s, it was first reported that the intensity of Raman scattering for a molecule may be dramatically increased when the molecule is placed in very close

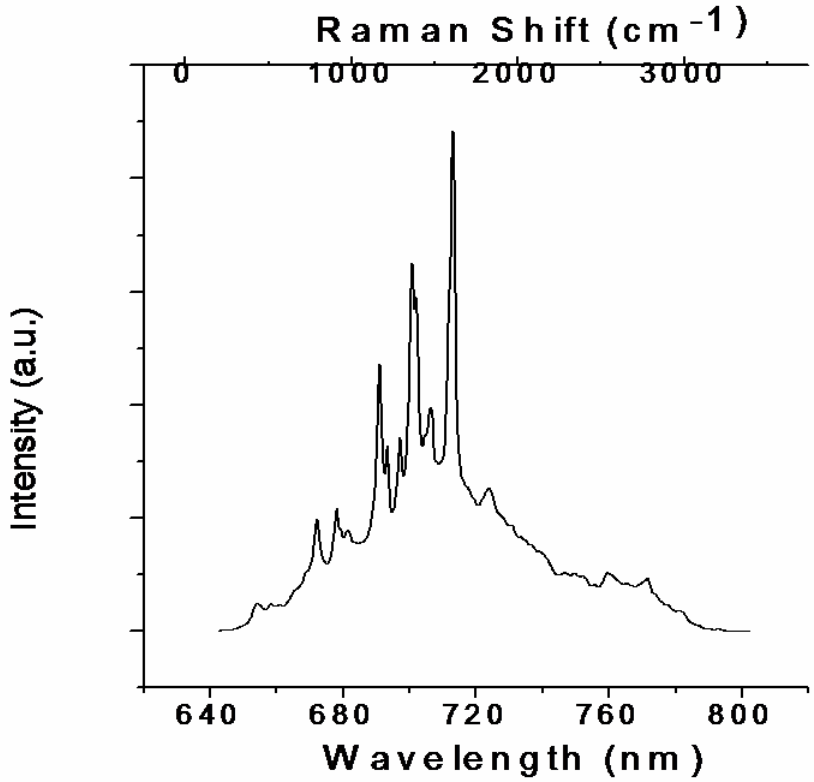

Figure 2.7: Plotting of Raman spectra. An example Raman spectrum with the energy of Raman scattered photons plotted on both relative wavenumber (Raman shift) and absolute wavelength scales.

proximity to a colloidal metal NP or roughened macroscale metal object with surface variation on the 10 to 100 nm scale.[60-62] This phenomenon is known as surface enhanced Raman scattering (SERS) and has since generated tremendous interest in the nanomaterials, spectroscopy, and analytical chemistry communities.[63-65] The enhancement factors in SERS can be enormous (on the order of 10^{14} to 10^{15}) and the once-unthinkable concept of single molecule detection with SERS has recently been achieved.[66,67] Under these conditions, Raman scattering can exceed the sensitivity of fluorescence.

The SERS effect is thought to arise from two mechanisms, one called electromagnetic field enhancement (EFE) and the other termed chemical enhancement (CE), which act in parallel. EFE accounts for the majority of the SERS enhancement and explains most of the observed features of SERS. Similar to the increased scattering intensity seen in PRPs, EFE is a manifestation of exciting localized surface plasmons in a metal nanostructure **(Figure 2.8)**. Monochromatic light that is resonant with a surface plasmon induces intense elastic light scattering. That scattered light is characterized by an electromagnetic field intensity that is extremely strong at certain portions of space near the metal NP surface. A molecule present in that space is excited by an enhanced field and produces more intense Raman scattered light than molecules outside that space. At low wavenumber shifts, the Raman scattered light can also excite the NP surface plasmon. The surface plasmon re-emits light at the Raman shifted wavelength with a further enhancement. Modest increases in the local field at the NP surface produce large Raman

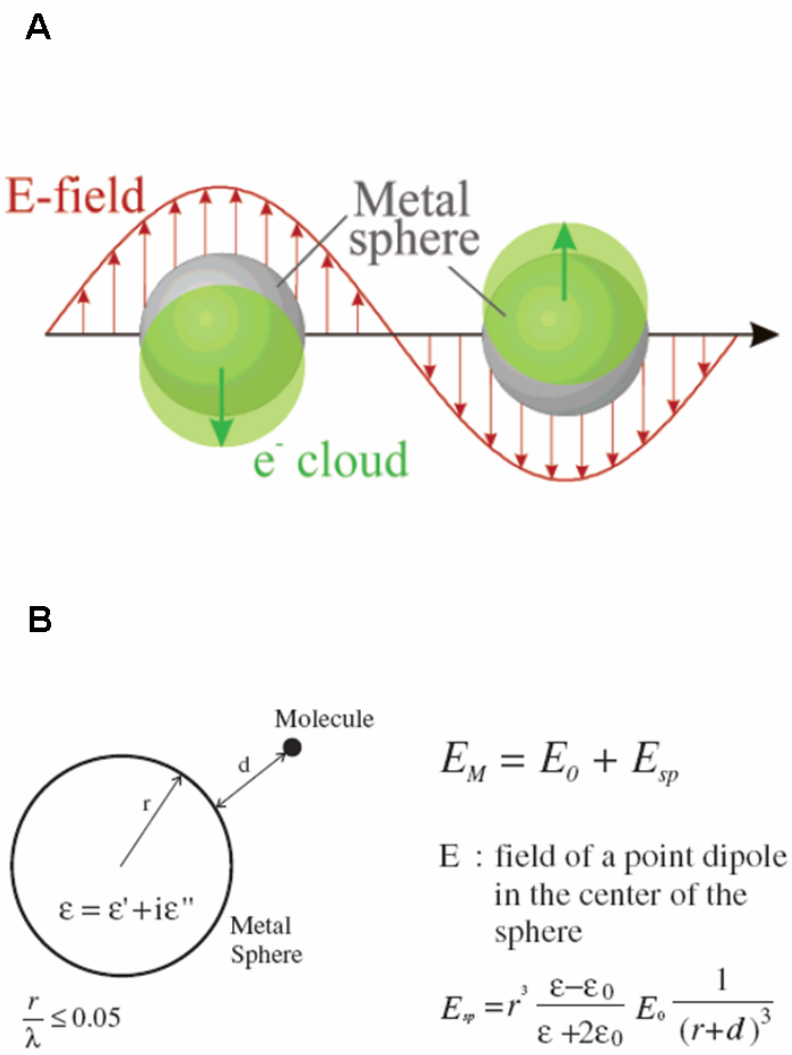

Figure 2.8. Schematic diagrams illustrating general features of electromagnetic field enhancement (EFE) in surface enhanced Raman scattering. (A) Surface plasmon resonance (SPR) occurs when the oscillation of the incident light electromagnetic field induces the collective oscillation of the conduction electrons of a metal nanoparticle As the wave front of the light passes, the NP electron density ("the cloud") is polarized to one side and oscillates in resonance with the light frequency. NP size and shape changes the electric field density on the NP surface, which in turn changes the oscillation frequency of the electrons. Reprinted from Reference 24. © American Chemical Society. (B) SPR generates elastically scattered light with an enhanced electromagnetic field relative to the incident light field. The scattered light induces Raman scattering of a molecule of distance *d* from the NP surface. The Raman scattered light field is enhanced by SPR as well. E_M, the electromagnetic field experienced by the molecule; E_o; incident light electromagnetic field E_{SP}, electromagnetic field induced by the surface plasmon; ε, dielectric constant of the metal NP ;ε_o, dielectric constant of the medium; λ, wavelength of incident light. Reprinted from Reference 65. © Institute of Physics.

scattering enhancements; it is commonly estimated that Raman enhancement scales with the fourth power of the original field enhancement.[63]

The Raman intensity of a molecule scales with the product of incident light electromagnetic field and the polarizability of the molecule.[64] Chemical enhancement (CE), the second mechanism of SERS, affects the latter. The 100-fold greater SERS enhancement of molecules directly adsorbed to a metal relative to SERS of molecules that lie on top of a monolayer of molecules attached to metal cannot be explained by invoking the distance dependence of EFE.[68,69] SERS enhancement also depends substantially on the chemical structure of the adsorbate, which cannot be accounted for by EFE.[70] CE generally has a much smaller effect than EFE. CE includes any effects associated with electronic coupling between the metal NP and its adsorbate. One model of CE is that excited electrons and holes in the metal NP generated by SPR can couple with the lowest unoccupied molecular orbital (LUMO) and highest occupied molecular orbital (HOMO) of the adsorbate (**Figure 2.9**).[71,72] Thus, charge transfer between metal NP and adsorbate can produce adsorbate electron excitation under conditions that would not occur if the adsorbate were free in solution. Relaxation of the excited electron to its ground state generates light emission (resonance Raman scattering).

SERS tags for biomolecular detection

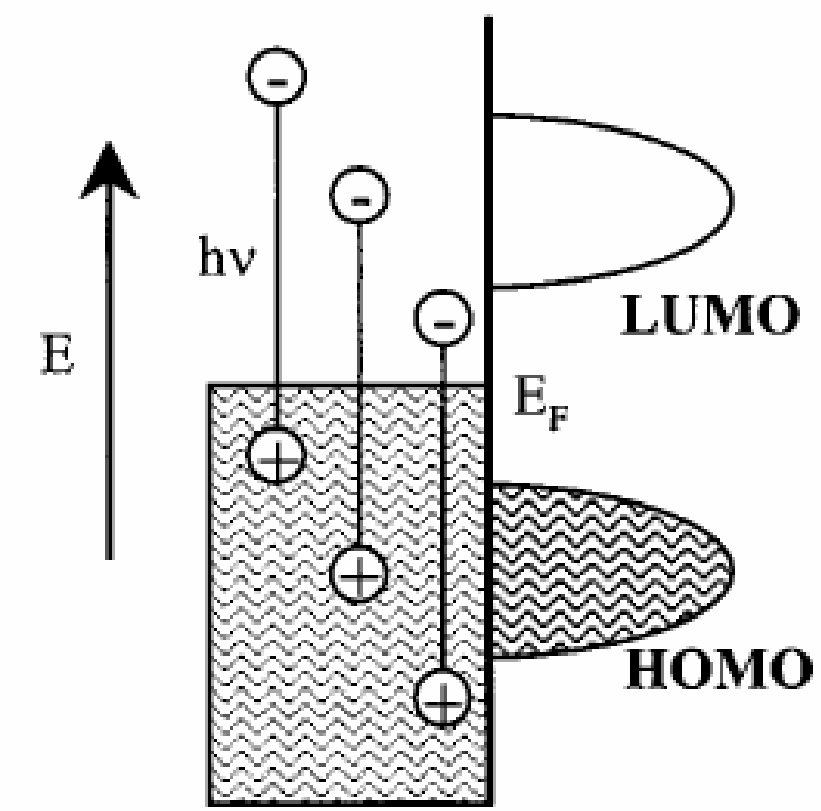

Figure 2.9: An example of chemical enhancement in SERS. Schematic diagram of relative energies of excited electron-hole pairs generated via surface plasmon resonance in the metal nanoparticle relative to the HOMO and LUMO of the chemisorbed molecule (adsorbate). HOMO, highest occupied molecular orbital; LUMO, lowest unoccupied molecular orbital. E_F, Fermi level.(highest energy state occupied by an electron at 0K) Reprinted from Reference 71. © American Chemical Society

Despite tremendous interest in the development of SERS tags for bioanalysis, research in this area has lagged behind that of QDs and PRPs. Not long ago, Raman experiments required expensive instrumentation custom built by individual investigators with specialized expertise in optics, electronics, and spectroscopy. Recent advances in optical hardware, optoelectronics, and computing have dramatically decreased the cost, space and expertise needed to perform sensitive and reproducible Raman spectroscopic measurements.[73-76] Concurrently, detailed microscopic investigations of the effects of NP size, shape, aggregation state, and material composition on SERS enhancement and methods of reproducibly controlling these parameters have been reported within the past few years.[77-85] Although many fundamental and practical questions remain, these studies have generated immense insight for assay development.

At a minimum a SERS tag is composed of an intrinsically strong Raman scattering molecule (called a Raman reporter) attached to a plasmon resonant metal NP and the NP-reporter complex protected from aggregation and non-specific binding by a suitable water-soluble surface coating (**Figure 2.10**). The Raman reporter generates the Raman spectral signature used to identify a biomolecular interaction whereas the metal nanostructure is used to amplify the Raman scattering signal for ultrasensitive detection. Efficient optical enhancement necessitates Raman reporter adsorption on the NP surface because CE requires chemical bonding and EFE is strongly distance-dependent (for some systems, $\mathrm{EFE} \propto (\mathrm{distance})^{-12}$).[65,86] Early approaches in developing SERS immunoassays

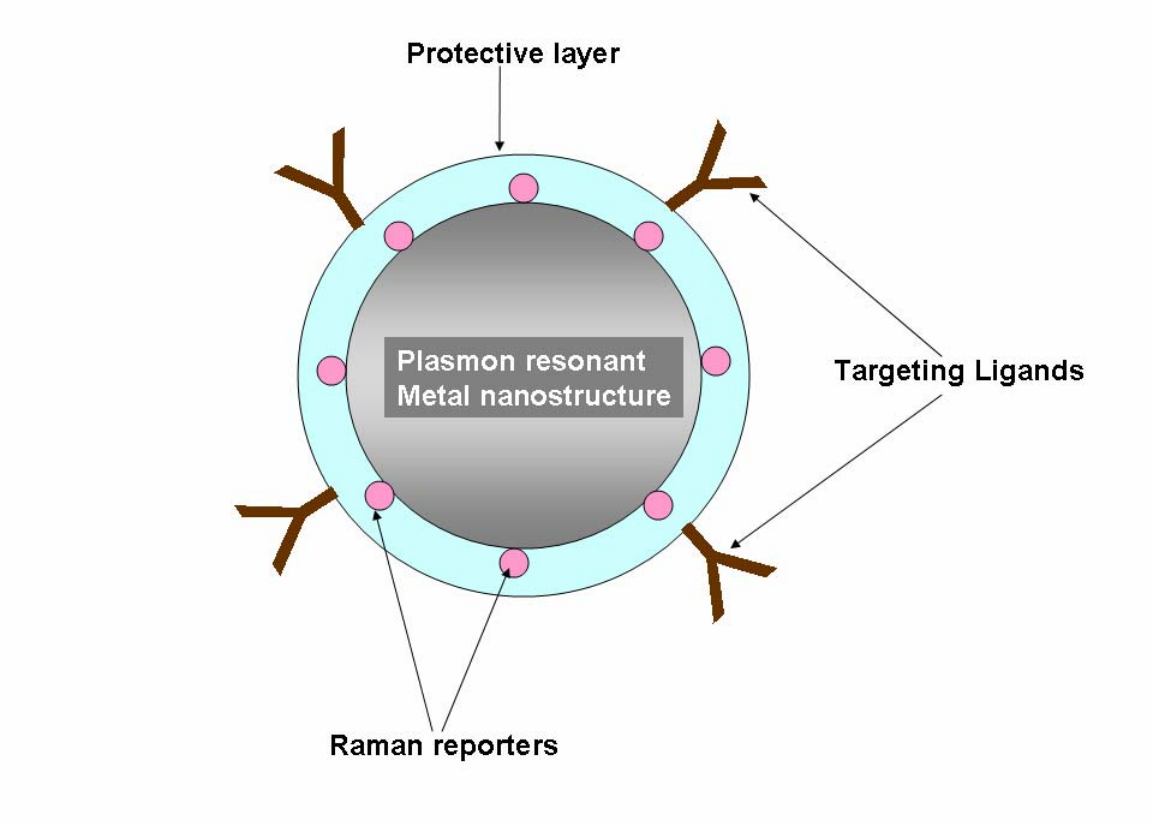

Figure 2.10: Protypical SERS tag. Schematic illustration showing generalized features of a targeted SERS tag suitable for optical tagging of biomolecules

are highly innovative but require external signal transduction via plasmonic coupling with an underlying metal substrate,[87-89] via *in situ* growth of nanoparticles with metal salts,[90-92] or via association with micrometer-scale polymeric matrices.[93,94] For SERS tags to complement or replace fluorescent and elastic-scattering tags in practical biomedical applications such as cytometry, immunohistochemistry, or *in vivo* imaging, the method of Raman signal generation must be completely self-contained and cannot require extensive modification by the end-user. Further, quantitative detection of disease-relevant molecules over a reasonable dynamic range necessitates that the SERS tag be bright but not be too much larger than the biomolecules of interest. For example, many proteins are ~10s of nanometers in size.

In 2003, Mulvaney, et al and Doering and Nie independently published the first reports of SERS tags meeting the standards described above.[95,96] Both groups prepared SERS tags by complexing AuNPs with Raman reporters and silane coupling agents, then growing a silica shell over the NP-reporter complex. This core-shell design sequesters the SERS tag from the external environment, guarding against uncontrolled spectral changes and aggregation. Mulvaney, et al used small organic molecules as reporters in their "glass-coated, analyte-tagged nanoparticles" (GANs) and showed that spectral output for the tags was linear with respect to laser power from 6 to 66 mW.[95] The GANS did not aggregate when transferred from water to organic solvents and the glass shell slowed the degradation of the AuNP core by aqua regia. Doering and Nie developed a set of especially bright SERS tags by using organosulfur chromophores as Raman reporters.[96] In comparison with SERS tags encoded with smaller organic compounds, the spectra of

chromophore-encoded tags are more complicated but are several orders of magnitude greater in intensity. The presence of an organosulfur group in the Raman reporter is necessary to prevent extensive reporter desorption from the AuNP surface during the silica coating procedure. The Raman spectra of these silica-coated SERS tags was unaffected by the presence of other SERS active chromophores added to the SERS tag solution. The silica layer of the SERS tags was conjugated to lectins and antibodies and the resulting conjugates used for cell and tissue labeling.[37] However, the signal-to-noise ratio of the labeling assays was not superior to assays using uncoated SERS tags.

A different approach was taken by Berlin and co-workers in developing a class of SERS tag that was coined composite organic-inorganic nanoparticles (COINS).[97] COINs were prepared by the simultaneous growth and aggregation of AgNP "seeds" in the presence of Raman reporters. In contrast to silica-encapsulated SERS tags, COINS could be encoded with Raman reporters lacking organosulfur groups. Mild aggregation was justified by theoretical and experimental work demonstrating enormously enhanced EFE at the junctions ("hot spots") between nanoparticle dimers and small clusters.[71,98,99] The COINs were protected from further aggregation through coating with cross-linked bovine serum albumin (BSA) and targeted by conjugation to IgG class antibodies. Antibody conjugated COINS were successfully employed in dual-analyte sandwich immunoassays and in immunohistochemistry of formalin-fixed paraffin-embedded tissue specimens.[97,100] It was recently reported that the signal to noise ratio of COIN staining in prostate tissue was superior to staining with an Alexa568 fluorophore conjugated to the same antibody.[101] However, the COIN staining showed much higher spot-to-spot variability

than the Alexa staining. Post-labeling of COIN stained tissue with fluorescent antibody against the COIN targeting ligand revealed the source of the variation: a significant proportion of the COINs bound to the target were not actually producing Raman signals.

2.5 References

1. Alivisatos AP. Semiconductor Clusters, Nanocrystals, and Quantum Dots. *Science*. 1996;271(5251):933-937.

2. Smith A, Nie S. Chemical analysis and cellular imaging with quantum dots. *ANALYST*. 2004;129(8):672-677.

3. Murray CB, Norris DJ, Bawendi MG. Synthesis and Characterization of Nearly Monodisperse Cde (e = S, Se, Te) Semiconductor Nanocrystallites. *Journal of the American Chemical Society*. 1993;115(19):8706-8715.

4. Dabbousi BO, RodriguezViejo J, Mikulec FV, et al. (CdSe)ZnS core-shell quantum dots: Synthesis and characterization of a size series of highly luminescent nanocrystallites. *Journal of Physical Chemistry B*. 1997;101(46):9463-9475.

5. Peng XG, Schlamp MC, Kadavanich AV, Alivisatos AP. Epitaxial growth of highly luminescent CdSe/CdS core/shell nanocrystals with photostability and electronic accessibility. *Journal of the American Chemical Society*. 1997;119(30):7019-7029.

6. Hines MA, Guyot-Sionnest P. Synthesis and characterization of strongly luminescing ZnS-Capped CdSe nanocrystals. *Journal of Physical Chemistry*. 1996;100(2):468-471.

7. Chan WC, nbsp, W, Nie S. Quantum Dot Bioconjugates for Ultrasensitive Nonisotopic Detection. *Science*. 1998;281(5385):2016-2018.

8. Bruchez M, Moronne M, Gin P, Weiss S, Alivisatos AP. Semiconductor Nanocrystals as Fluorescent Biological Labels. *Science*. 1998;281(5385):2013-2016.

9. Goldman E, Anderson G, Tran P, et al. Conjugation of luminescent quantum dots with antibodies using an engineered adaptor protein to provide new reagents for fluoroimmunoassays. *Analytical Chemistry*. 2002;74(4):841-847.

10. Ding S, Chen J, Jiang H, et al. Application of Quantum Dot-Antibody Conjugates for Detection of Sulfamethazine Residue in Chicken Muscle Tissue. *J. Agric. Food Chem.* 2006;54(17):6139-6142.

11. Agrawal A, Sathe T, Nie S. Single-Bead Immunoassays Using Magnetic Microparticles and Spectral-Shifting Quantum Dots. *J. Agric. Food Chem.* 2007;55(10):3778-3782.

12. Kerman K, Endo T, Tsukamoto M, et al. Quantum dot-based immunosensor for the detection of prostate-specific antigen using fluorescence microscopy. *Talanta*. 2007;71(4):1494-1499.

13. Dahan M, Levi S, Luccardini C, et al. Diffusion dynamics of glycine receptors revealed by single-quantum dot tracking. *Science*. 2003;302(5644):442-445.

14. Lidke D, Nagy P, Heintzmann R, et al. Quantum dot ligands provide new insights into erbB/HER receptor-mediated signal transduction. *Nature Biotechnology*. 2004;22(2):198-203.

15. Xing Y, Chaudry Q, Shen C, et al. Bioconjugated quantum dots for multiplexed and quantitative immunohistochemistry. *Nat. Protocols*. 2007;2(5):1152-1165.

16. Ghazani AA, Lee JA, Klostranec J, et al. High throughput quantification of protein expression of cancer antigens in tissue microarray using quantum dot nanocrystals. *Nano Letters*. 2006;6(12):2881-2886.

17. Byers RJ, Di Vizio D, O'Connell F, et al. Semiautomated multiplexed quantum dot-based in situ hybridization and spectral deconvolution. *Journal of Molecular Diagnostics*. 2007;9(1):20-29.

18. Gao XH, Cui YY, Levenson RM, Chung LWK, Nie SM. In vivo cancer targeting and imaging with semiconductor quantum dots. *Nature Biotechnology*. 2004;22(8):969-976.

19. Cai W, Shin DW, Chen K, et al. Peptide-Labeled Near-Infrared Quantum Dots for Imaging Tumor Vasculature in Living Subjects. *Nano Lett.* 2006;6(4):669-676.

20. Akerman ME, Chan WCW, Laakkonen P, Bhatia SN, Ruoslahti E. Nanocrystal targeting in vivo. *Proceedings of the National Academy of Sciences of the United States of America*. 2002;99(20):12617-12621.

21. Schultz S, Smith DR, Mock JJ, Schultz DA. Single-target molecule detection with nonbleaching multicolor optical immunolabels. *Proceedings of the National Academy of Sciences of the United States of America*. 2000;97(3):996-1001.

22. Eustis S, El-Sayed MA. Why gold nanoparticles are more precious than pretty gold: Noble metal surface plasmon resonance and its enhancement of the radiative and

nonradiative properties of nanocrystals of different shapes. *Chemical Society Reviews*. 2006;35(3):209-217.

23. Gustav M. Beiträge zur Optik trüber Medien, speziell kolloidaler Metallösungen. *Annalen der Physik*. 1908;330(3):377-445.

24. Kelly KL, Coronado E, Zhao LL, Schatz GC. The optical properties of metal nanoparticles: the influence of size, shape, and dielectric environment. *J. Phys. Chem. B.* 2003;107(3):668–677.

25. Victor I. Klimov. *Semiconductor and metal nanocrystals*. CRC Press; 2003.

26. Mulvaney P. Surface Plasmon Spectroscopy of Nanosized Metal Particles. *Langmuir*. 1996;12(3):788-800.

27. Mock J, Barbic M, Smith D, Schultz D, Schultz S. Shape effects in plasmon resonance of individual colloidal silver nanoparticles. *Journal of Chemical Physics*. 2002;116(15):6755-6759.

28. Lazarides AA, Lance Kelly K, Jensen TR, Schatz GC. Optical properties of metal nanoparticles and nanoparticle aggregates important in biosensors. *Journal of Molecular Structure: Theochem*. 2000;529(1-3):59-63.

29. Oldenburg SJ, Averitt RD, Westcott SL, Halas NJ. Nanoengineering of optical resonances. *Chemical Physics Letters*. 1998;288(2-4):243-247.

30. Lee K, El-Sayed M. Gold and Silver Nanoparticles in Sensing and Imaging: Sensitivity of Plasmon Response to Size, Shape, and Metal Composition. *J. Phys. Chem. B*. 2006;110(39):19220-19225.

31. Yguerabide J, Yguerabide EE. Light-scattering submicroscopic particles as highly fluorescent analogs and their use as tracer labels in clinical and biological applications - I. Theory. *Analytical Biochemistry*. 1998;262(2):137-156.

32. Turkevich J, Stevenson PC, Hillier J. A Study of the Nucleation and Growth Processes in the Synthesis of Colloidal Gold. *Discussions of the Faraday Society*. 1951;(11):55-&.

33. Frens G. Controlled Nucleation for Regulation of Particle-Size in Monodisperse Gold Suspensions. *Nature-Physical Science*. 1973;241(105):20-22.

34. Lee PC, Meisel D. Adsorption and surface-enhanced Raman of dyes on silver and gold sols. *J. Phys. Chem.* 1982;86(17):3391-3395.

35. Brown KR, Natan MJ. Hydroxylamine seeding of colloidal Au nanoparticles in solution and on surfaces. *Langmuir*. 1998;14(4):726-728.

36. Brown KR, Lyon LA, Fox AP, Reiss BD, Natan MJ. Hydroxylamine seeding of colloidal au nanoparticles. 3. Controlled formation of conductive Au films. *Chemistry of Materials*. 2000;12(2):314-323.

37. Doering W. Ph.D. Dissertation. Indiana University. Dept of Chemistry. 2003.

38. Nikoobakht B, El-Sayed M. Preparation and growth mechanism of gold nanorods (NRs) using seed-mediated growth method. *Chemistry of Materials*. 2003;15(10):1957-1962.

39. Neeves A, Birnboim M. Composite Structures for the Enhancement of Nonlinear-Optical Susceptibility. *Journal of the Optical Society of America B-Optical Physics*. 1989;6(4):787-796.

40. West JL, Halas NJ. Engineered nanomaterials for biophotonics applications: Improving sensing, imaging, and therapeutics. *Annual Review of Biomedical Engineering*. 2003;5:285-292.

41. Hayat MA. *Colloidal Gold: Principles, Methods, and Applications*. Academic Press; 1990.

42. Hayat MA. *Immunogold-Silver Staining*. CRC Press; 1995.

43. Walton I, Norton S, Balasingham A, et al. Particles for multiplexed analysis in solution: Detection and identification of striped metallic particles using optical microscopy. *Analytical Chemistry*. 2002;74(10):2240-2247.

44. Cao Y, Jin R, Mirkin C. DNA-modified core-shell Ag/Au nanoparticles. *Journal of the American Chemical Society*. 2001;123(32):7961-7962.

45. Li Z, Jin R, Mirkin C, Letsinger R. Multiple thiol-anchor capped DNA-gold nanoparticle conjugates. *Nucleic Acids Research*. 2002;30(7):1558-1562.

46. LizMarzan L, Giersig M, Mulvaney P. Synthesis of nanosized gold-silica core-shell particles. *Langmuir*. 1996;12(18):4329-4335.

47. Obare S, Jana N, Murphy C. Preparation of polystyrene- and silica-coated gold nanorods and their use as templates for the synthesis of hollow nanotubes. *Nano Letters*. 2001;1(11):601-603.

48. Nath S, Kaittanist C, Tinkharn A, Perez J. Dextran-coated gold nanoparticles for the assessment of antimicrobial susceptibility. *Analytical Chemistry*. 2008;80(4):1033-1038.

49. Lee S, Perez-Luna V. Surface-grafted hybrid material consisting of gold nanoparticles and dextran exhibits mobility and reversible aggregation on a surface. *Langmuir*. 2007;23(9):5097-5099.

50. Hone D, Haines A, Russell D. Rapid, Quantitative Colorimetric Detection of a Lectin Using Mannose-Stabilized Gold Nanoparticles. *Langmuir*. 2003;19(17):7141-7144.

51. Shan J, Tenhu H. Recent advances in polymer protected gold nanoparticles: synthesis, properties and applications. *Chemical Communications*. 2007;(44):4580-4598.

52. Taton T, Lu G, Mirkin C. Two-color labeling of oligonucleotide arrays via size-selective scattering of nanoparticle probes. *Journal of the American Chemical Society*. 2001;123(21):5164-5165.

53. Bao P, Frutos A, Greef C, et al. High-sensitivity detection of DNA hybridization on microarrays using resonance light scattering. *Analytical Chemistry*. 2002;74(8):1792-1797.

54. Oldenburg S, Genick C, Clark K, Schultz D. Base pair mismatch recognition using plasmon resonant particle labels. *Analytical Biochemistry*. 2002;309(1):109-116.

55. Siiman O, Burshteyn A. Preparation, Microscopy, and Flow Cytometry with Excitation into Surface Plasmon Resonance Bands of Gold or Silver Nanoparticles on Aminodextran-Coated Polystyrene Beads. *J. Phys. Chem. B*. 2000;104(42):9795-9810.

56. Loo C, Lowery A, Halas N, West J, Drezek R. Immunotargeted nanoshells for integrated cancer imaging and therapy. *Nano Letters*. 2005;5(4):709-711.

57. Huang X, El-Sayed IH, Qian W, El-Sayed MA. Cancer cell imaging and photothermal therapy in the near-infrared region by using gold nanorods. *J Am Chem Soc*. 2006;128(6):2115-20.

58. Smith E, Dent G. *Modern Raman Spectroscopy: A Practical Approach*. Hoboken, NJ: Wiley; 2005.

59. Sijtsema N, Duindam J, Puppels G, Otto C, Greve J. Imaging with extrinsic Raman labels. *Applied Spectroscopy*. 1996;50(5):545-551.

60. Fleischm.M, Hendra PJ, McQuilla.Aj. Raman-Spectra of Pyridine Adsorbed at a Silver Electrode. *Chemical Physics Letters*. 1974;26(2):163-166.

61. Jeanmaire DL, Vanduyne RP. Surface Raman Spectroelectrochemistry .1. Heterocyclic, Aromatic, and Aliphatic-Amines Adsorbed on Anodized Silver Electrode. *Journal of Electroanalytical Chemistry*. 1977;84(1):1-20.

62. Albrecht MG, Creighton JA. Anomalously Intense Raman-Spectra of Pyridine at a Silver Electrode. *Journal of the American Chemical Society*. 1977;99(15):5215-5217.

63. Campion A, Kambhampati P. Surface-enhanced Raman scattering. *Chemical Society Reviews*. 1998;27(4):241-250.

64. Moskovits M. Surface-enhanced Raman spectroscopy: a brief retrospective. *Journal of Raman Spectroscopy*. 2005;36(6-7):485-496.

65. Kneipp K, Kneipp H, Itzkan I, Dasari RR, Feld MS. Surface-enhanced Raman scattering and biophysics. *Journal of Physics-Condensed Matter*. 2002;14(18):R597-R624.

66. Doering WE, Nie SM. Single-molecule and single-nanoparticle SERS: Examining the roles of surface active sites and chemical enhancement. *Journal of Physical Chemistry B*. 2002;106(2):311-317.

67. Kneipp K, Wang Y, Kneipp H, et al. Single molecule detection using surface-enhanced Raman scattering (SERS). *Physical Review Letters*. 1997;78(9):1667-1670.

68. Sanda P, Warlaumont J, Demuth J, et al. Surface-Enchanced Raman-Scattering from Pyridine on Ag(111). *Physical Review Letters*. 1980;45(18):1519-1523.

69. Persson BNJ. On the theory of surface-enhanced Raman scattering. *Chemical Physics Letters*. 1981;82(3):561-565.

70. Moskovits M. Surface-enhanced spectroscopy. *Reviews of Modern Physics*. 1985;57(3):783.

71. Michaels AM, Jiang J, Brus L. Ag nanocrystal junctions as the site for surface-enhanced Raman scattering of single Rhodamine 6G molecules. *Journal of Physical Chemistry B*. 2000;104(50):11965-11971.

72. Kneipp J, Kneipp H, Kneipp K. SERS - a single-molecule and nanoscale tool for bioanalytics. *Chemical Society Reviews*. 2008;37(5):1052-1060.

73. Young M, Stuart D, Lyandres O, Glucksberg M, Van Duyne R. Surface-enhanced Raman spectroscopy with a laser pointer light source and miniature spectrometer. *Canadian Journal of Chemistry-Revue Canadienne De Chimie*. 2004;82(10):1435-1441.

74. Gift AD, Ma J, Haber KS, McClain BL, Ben-Amotz D. Near-infrared Raman imaging microscope based on fiber-bundle image compression. *Journal of Raman Spectroscopy*. 1999;30(9):757-765.

75. Pelletier MJ. *Analytical applications of Raman spectroscopy*. Blackwell Science Ltd.; 1999.

76. Harris C. Raman on the run. *Analytical Chemistry*. 2003;75(3):75A-78A.

77. Nie SM, Emery SR. Probing single molecules and single nanoparticles by surface-enhanced Raman scattering. *Science*. 1997;275(5303):1102-1106.

78. Krug JT, Wang GD, Emory SR, Nie SM. Efficient Raman enhancement and intermittent light emission observed in single gold nanocrystals. *Journal of the American Chemical Society*. 1999;121(39):9208-9214.

79. Emory SR. Direct Observation of Size-Dependent Optical Enhancement in Single Metal Nanoparticles. *Journal of the American Chemical Society.* 1998;120(31):8009-8010.

80. Talley C, Jackson J, Oubre C, et al. Surface-Enhanced Raman Scattering from Individual Au Nanoparticles and Nanoparticle Dimer Substrates. *Nano Lett.* 2005;5(8):1569-1574.

81. Schierhorn M, Lee S, Boettcher S, Stucky G, Moskovits M. Metal-Silica Hybrid Nanostructures for Surface-Enhanced Raman Spectroscopy. *Advanced Materials*. 2006;18(21):2829-2832.

82. Jackson J, Halas N. Surface-enhanced Raman scattering on tunable plasmonic nanoparticle substrates. *Proceedings of the National Academy of Sciences of the United States Of*. 2004;101(52):17930-17935.

83. Orendorff C, Gearheart L, Jana N, Murphy C. Aspect ratio dependence on surface enhanced Raman scattering using silver and gold nanorod substrates. *Physical Chemistry Chemical Physics*. 2006;8(1):165-170.

84. Hao E, Schatz GC. Electromagnetic fields around silver nanoparticles and dimers. *J. Chem. Phys.* 2004;120(1):357-366.

85. Banholzer M, Millstone J, Qin L, Mirkin C. Rationally designed nanostructures for surface-enhanced Raman spectroscopy. *Chemical Society Reviews*. 2008;37(5):885-897.

86. Kennedy B, Spaeth S, Dickey M, Carron K. Determination of the distance dependence and experimental effects for modified SERS substrates based on self-assembled monolayers formed using alkanethiols. *Journal of Physical Chemistry B*. 1999;103(18):3640-3646.

87. Ni J, Lipert RJ, Dawson GB, Porter MD. Immunoassay readout method using extrinsic Raman labels adsorbed on immunogold colloids. *Analytical Chemistry*. 1999;71(21):4903-4908.

88. Grubisha DS, Lipert RJ, Park HY, Driskell J, Porter MD. Femtomolar detection of prostate-specific antigen: An immunoassay based on surface-enhanced Raman scattering and immunogold labels. *Analytical Chemistry*. 2003;75(21):5936-5943.

89. Driskell J, Lipert R, Porter M. Labeled gold nanoparticles immobilized at smooth metallic substrates: Systematic investigation of surface plasmon resonance and surface-enhanced Raman scattering. *Journal of Physical Chemistry B*. 2006;110(35):17444-17451.

90. Cao YWC, Jin RC, Mirkin CA. Nanoparticles with Raman spectroscopic fingerprints for DNA and RNA detection. *Science*. 2002;297(5586):1536-1540.

91. Cao YC, Jin RC, Nam JM, Thaxton CS, Mirkin CA. Raman dye-labeled nanoparticle probes for proteins. *Journal Of The American Chemical Society*. 2003;125(48):14676-14677.

92. Ansari DO, Stuart DA, Nie SM. Enhanced Raman spectroscopic detection of protein biomarkers in intact cells and tissues. *Proc. SPIE- Int. Soc. Opt. Eng.* 2005;5699:82-90.

93. McCabe AF, Eliasson C, Prasath RA, et al. SERRS labelled beads for multiplex detection. *Faraday Discussions*. 2006;132:303-308.

94. Souza GR, Christianson DR, Staquicini FI, et al. Networks of gold nanoparticles and bacteriophage as biological sensors and cell-targeting agents. *Proceedings of the National Academy of Sciences of the United States of America*. 2006;103(5):1215-1220.

95. Mulvaney SP, Musick MD, Keating CD, Natan MJ. Glass-coated, analyte-tagged nanoparticles: A new tagging system based on detection with surface-enhanced Raman scattering. *Langmuir*. 2003;19(11):4784-4790.

96. Doering WE, Nie SM. Spectroscopic tags using dye-embedded nanoparticies and surface-enhanced Raman scattering. *Analytical Chemistry*. 2003;75(22):6171-6176.

97. Su X, Zhang J, Sun L, et al. Composite organic-inorganic nanoparticles (COINs) with chemically encoded optical signatures. *Nano Letters*. 2005;5(1):49-54.

98. Bosnick K, Jiang J, Brus L. Fluctuations and local symmetry in single-molecule rhodamine 6G Raman scattering on silver nanocrystal aggregates. *Journal of Physical Chemistry B*. 2002;106(33):8096-8099.

99. Schwartzberg AM, Grant CD, Wolcott A, et al. Unique gold nanoparticle aggregates as a highly active surface-enhanced Raman scattering substrate. *Journal of Physical Chemistry B*. 2004;108(50):19191-19197.

100. Sun L, Sung K, Dentinger C, et al. Composite organic-inorganic nanoparticles as Raman labels for tissue analysis. *Nano Letters*. 2007;7(2):351-356.

101. Lutz B, Dentinger C, Sun L, et al. Raman nanoparticle probes for antibody-based protein detection in tissues. *Journal of Histochemistry & Cytochemistry*. 2008;56(4):371-379.

CHAPTER 3

POLYMER-PROTECTED RAMAN-ENCODED NANOPARTICLE TAGS (PRENTS) FOR CANCER BIOMARKER DETECTION

3.1 Introduction

The development of sensitive optical tags to detect specific molecules in biological substrates is of considerable interest in clinical diagnostics and in many research disciplines. For many years, organic dye fluorophores have been the leading tagging technology in a variety of applications because of their brightness, mature chemistry, and widespread availability. However, the use of organic dyes has a number of drawbacks including photobleaching, narrow excitation profiles, uncontrolled spectral changes in certain environments, and difficult separation of tag signals from background signal.

Here we report a new class of optical tag based on polyethylene glycol protected nanoparticles and surface enhanced Raman scattering. This tag design is termed polymer-protected Raman-encoded nanoparticle tags (PRENTs) and is composed of Raman reporter molecules for fingerprint-like spectral signatures, gold nanoparticles (AuNPs) for signal enhancement, a layer of grafted polyethylene glycol (PEG) for protection and conjugation, and IgG antibodies for biological targeting.

The use of tags that produce Raman spectral readouts is a promising but relatively new approach for optical detection of biomolecules.[1,2] Based on the fundamental properties of

Raman scattering, Raman assays are expected to provide important advantages over fluorescence assays with respect to photostability, flexibility of excitation wavelength, generation of spectral diversity, and separation from background sample fluorescence. Although normal Raman scattering is inefficient, complexing Raman scattering labels with rationally designed metal nanostructures that exploit the surface enhanced Raman effect (SERS) yields intense Raman signals that can exceed those of fluorescence.[3-7]

Equally attractive is the use of PEG as a platform for nanoparticle protection and bioconjugation. Without a passivating surface coating, SERS active AuNP-Raman reporter complexes used in biological assays rapidly aggregate or become fouled with non-specific biomolecules. In addition, surface-bound Raman reporters are prone to desorption or subject to displacement by other molecules with affinity for AuNPs. The high sensitivity of surface enhancement makes SERS tags are a more challenging system than plasmon resonant particles (PRPs) as the surface coating itself may affect the reporter Raman spectrum or introduce spectral changes of its own. Consistent observation of biocompatibility and resistance to protein adsorption has led to the established use of PEG in drug delivery and biomaterials research.[8,9] More recently, Wuelfing, et al demonstrated that covalent grafting of thiolated PEG (PEG-SH) monolayer on AuNPs shuts off place-exchange reactions with other thiol ligands and slowed decomposition of the AuNP in the presence of cyanide relative to alkanethiols.[10] Otsuka, et al showed that PEG-SH grafted AuNPs were highly stable under physiologic conditions and that a heterobifunctional PEG provided an efficient means of covalently attaching targeting ligands to AuNPs. Since those initial reports, PEG-SH grafted AuNPs

have shown minimal non-specific absorption to proteins[11] and cell surfaces[12] and negligible cytotoxicity in intracellular delivery studies.[13] When injected into living animals for diagnostic or therapeutic applications, PEG-SH grafted AuNPs demonstrate excellent biodistribution and pharmacokinetic properties due to the lack of immunogenicity and decreased phagocytosis.[14-16]

Based on these reports, we *hypothesized* that a new SERS tag design that protects AuNP-Raman reporter complexes with a layer of grafted polyethylene glycol (PEG) would be simpler to synthesize, resistant to non-specific binding, aggregation, and uncontrolled spectral changes under a wide range of conditions, more amenable to bioconjugation, and practically useful in a broader range of biological detection assays than recently reported SERS tags based on silica or protein coatings.[17-19] Despite its potential advantages, the use of PEG in Raman tagging assays has not been previously reported.

In this chapter we describe the preparation and detailed characterization of polymer-protected Raman-encoded nanoparticle tags (PRENTs) with six distinct spectral signatures. We provide mechanistic insight into how the PEG-SH stabilizes surface bound reporters rather than displaces them. We compare PRENT optical properties to QDs. We also functionalize the PRENTs with antibodies (A-PRENTs) and use the A-PRENTs to detect cell surface biomarkers on living cancer cells.

3.2 Results and Discussion

Design and preparation of PRENTs

As shown in **Figure 3.1**, we first developed PRENTs composed of three elements: Gold particles with a mean diameter of ~60 nm (AuNPs), organic molecules that exhibit strong Raman scattering signals (Raman reporters), and thiol-derivatized polymers (α-methoxy-ω-mercapto-poly(ethylene glycol), PEG-SH). First, a solution of Raman reporter molecules was added dropwise to a rapidly mixing solution of AuNPs to evenly distribute the reporters on the nanoparticle surfaces and prevent aggregation (AuNP-reporter, **Figure 3.1B**). Then PEG-SH was reacted with the Au-reporter complex and the conjugate purified by repeated centrifugation and redispersion in water (PRENT, **Figure 3.1C**). This tag design generated intense Raman signals while minimizing AuNP aggregation. Adsorbing reporter molecules directly on the AuNP surface provides enormous Raman enhancements due to strongly distance-dependent electromagnetic field enhancement and possible charge transfer mechanisms between reporter and metal (chemical enhancement).[20-22]

Monodisperse AuNPs with a mean diameter of ~60 nm are efficient for Raman enhancement at 633 nm and 647 nm excitation wavelengths. About 10-15% of particles in such single NP preparations are SERS active,[23] substantially higher than in aggregated NP preparations.[24] This percentage is less than 100% because other poorly controlled factors such as surface active sites (e.g. adatoms and sharp edges) play a significant role

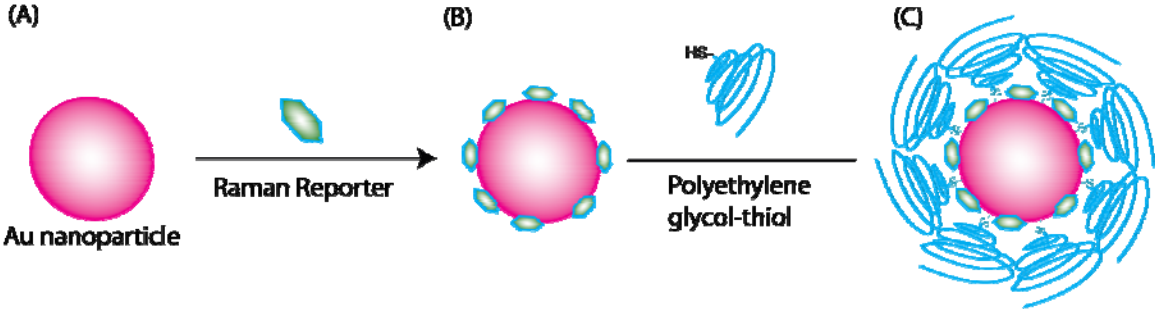

Figure 3.1: Schematic illustration of the procedure for preparing polymer-protected Raman encoded nanoparticle tags (PRENTs). (A) ~ 60 nm diameter colloidal gold nanoparticles (AuNPs). (B) Complex of gold nanoparticles and adsorbed Raman reporter (AuNP-reporter). (C) Complex of gold nanoparticles, Raman reporter, and polyethylene glycol-thiol (PEG-SH) composes a PRENT.

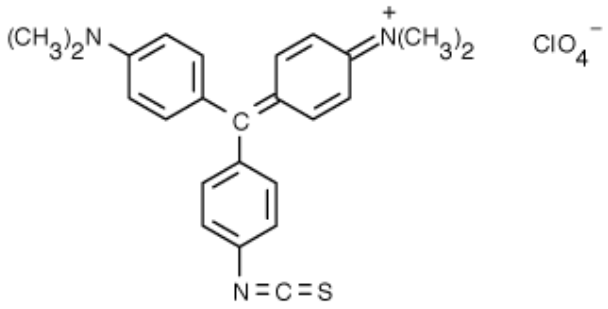

Figure 3.2: Chemical structure of malachite green isothiocyanate

in Raman enhancement.[25,26] Although silver NPs provide the greatest enhancement factors, monodisperse AuNPs are easier to synthesize, more stable, and are commercially available in a wider range of mean NP diameter. In addition, the interactions of AuNPs with proteins, polymers, and biological systems are better characterized[27-30] and AuNPs provide sufficient Raman enhancements at much smaller sizes[31].

The interaction of monochromatic light with the surface bound Raman reporter gives the PRENT its characteristic spectral signature. Malachite green isothiocyanate (MGITC, **Figure 3.2**) was initially chosen as a Raman reporter because its extended pi electron system can be easily polarized,[32] the spectroscopic properties of malachite green derivatives under a variety of conditions have been previously studied[33] and the sulfur atom in MGITC's isothiocyanate group was expected to form a stable bond with Au[34].

A key feature of PRENTs is the use of a self-assembled monolayer of grafted polyethylene glycol (PEG) derivatives. Covalent anchoring of polymers via a chemically-defined end-group is generally superior to traditional physisorption techniques for controlling grafting density and conferring long-term stability of AuNPs under physiologically relevant conditions.[35,36] A post-synthesis "grafting to" approach offers the best combination of monodispersity and reproducibility and presents mild conditions that are least likely to adversely affect reporter stability and Raman spectral signatures.[37,38] The strong chemisorption of thiols on AuNPs justifies the use of the thiol functional group as an anchoring moiety; the Au-thiolate linkage possesses a higher bond energy than complexes of Au with other common nucleophiles.[39] The distal end of the

PEG-SH used in this study contains a methoxy functional group. When self-assembled onto Au, both hydroxyl and methoxy capped PEG derivatives show extremely low levels of protein binding.[40] However, methoxy groups are more resistant to chemical modification *in vitro* and enzymatic oxidation i*n vivo* that can lead to non-specific binding.[41]

Characterization of PRENTs

Figure 3.3 addresses two early concerns about the PRENT design. The first concern is that the high affinity of PEG-SH for AuNPs may displace reporters away from the AuNP surface and reduce the Raman spectral signature; the replacement of AuNP bound organosulfur ligands by different organosulfur ligands free in solution is commonly observed.[42] Second, both polyethylene glycols and proteins possess intrinsic Raman scattering signals that may complicate PRENT spectral signatures.[43,44] To determine whether these factors would have any effect on the PRENT spectral signature, complexes of AuNPs and MGITC reporters were incubated with an excess of PEG-SH polymers or PEG-SH grafted antibodies (IgG-PEG-SH) and interrogated by Raman spectroscopy. **Figure 3.3** indicates that there were no differences in the Raman scattering spectra of unprotected Au-MGITC complex (**Figure 3.3A)**, the same complex incubated with a thirty-fold excess of PEG-SH relative to reporters (300,000 PEG-SH per nanoparticle, **Figure 3.3B)**, and the complex incubated with an excess of PEG-SH and IgG-PEG-SH (**Figure 3.3C). Figure 3.3 D** is a Raman scattering spectrum of AuNPs incubated with

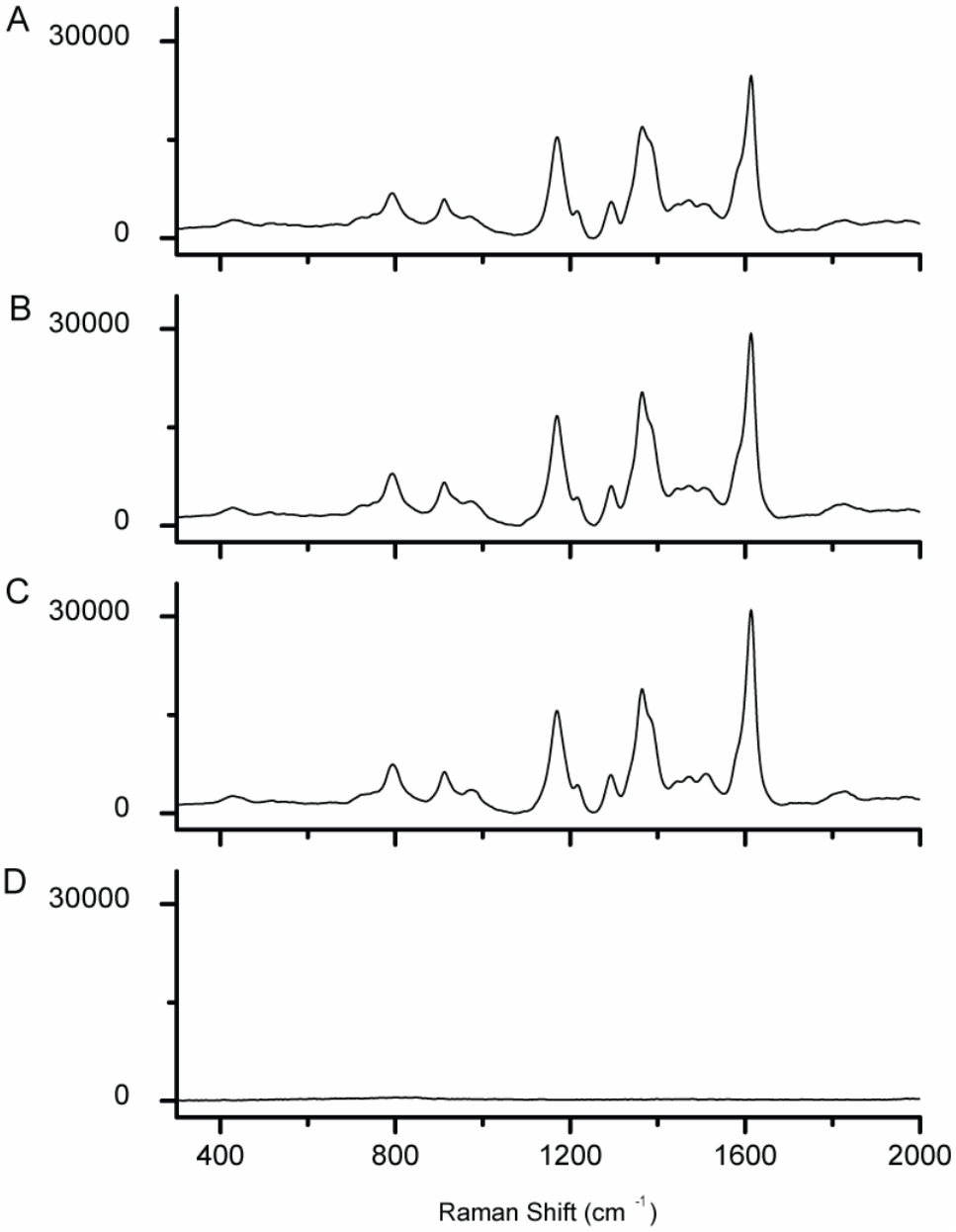

Figure 3.3: Effect of PEG-SH AND IgG-PEG-SH grafting on the spectral signature of gold nanoparticle –reporter molecule complexes. Raman spectra of AuNP-MGITC complex (**A**), AuNP incubated with MGITC and PEG-SH, with 30-fold excess of PEG-SH polymers to MGITC reporter molecules (**B**), AuNP incubated with MGITC, PEG-SH, and IgG-PEG-SH, 30-fold excess of PEG-SH to MGITC and equimolar amount of IgG-PEG-SH to MGITC (**C**), and AuNP incubated with PEG-SH and IgG-PEG-SH in the absence of MGITC.

PEG-SH and IgG-PEG-SH. No spectral contribution from either the PEG-SH or the IgG-PEG-SH was observed under conditions used for PRENT preparation. Only the MGITC reporter molecule contributed to the spectral signature of the resulting PRENT.

Adding a large amount of the reporter relative to the number of NPs in the solution caused immediate and extensive aggregation of the NPs. This finding is due to the fact that MGITC is cationic and that the AuNPs used in this study are stabilized in solution by negatively charged surface ligands. Thus, the reporter molecule to AuNP ratio used for MGITC-encoded PRENTs (~ 14000) was kept high enough to produce a strong Raman spectral signature but low enough to keep the colloidal preparation stable prior to the addition of the PEG derivatives. Reproducibility in preparing PRENTs required careful adherence to experimental protocols since the stock reporter concentration, volume ratio of stock reporter solution and AuNP solution, and rate of addition of reporter to AuNPs all affected the Raman scattering intensity and aggregation state of the resulting PRENT. When reporter solution was added to AuNP solution, we observed much higher Raman scattering signal than when adding NP solution to reporter solution.

Several experimental techniques (absorption spectroscopy, TEM, and DLS) verified the lack of aggregation of MG-encoded PRENTs (**Figure 3.4).** Addition of MGITC or PEG-SH caused neither a dramatic decrease in the plasmon resonance band at 535 nm nor a dramatic increase in the broadband adsorption at wavelengths greater than ~ 650 nm (**Figure 3.4B**) relative to the unmodified AuNPs (**Figure 3.4A)**. PEG-SH grafting did induce a slight (~1nm) bathochromic shift in absorbance. The spectral change occurred

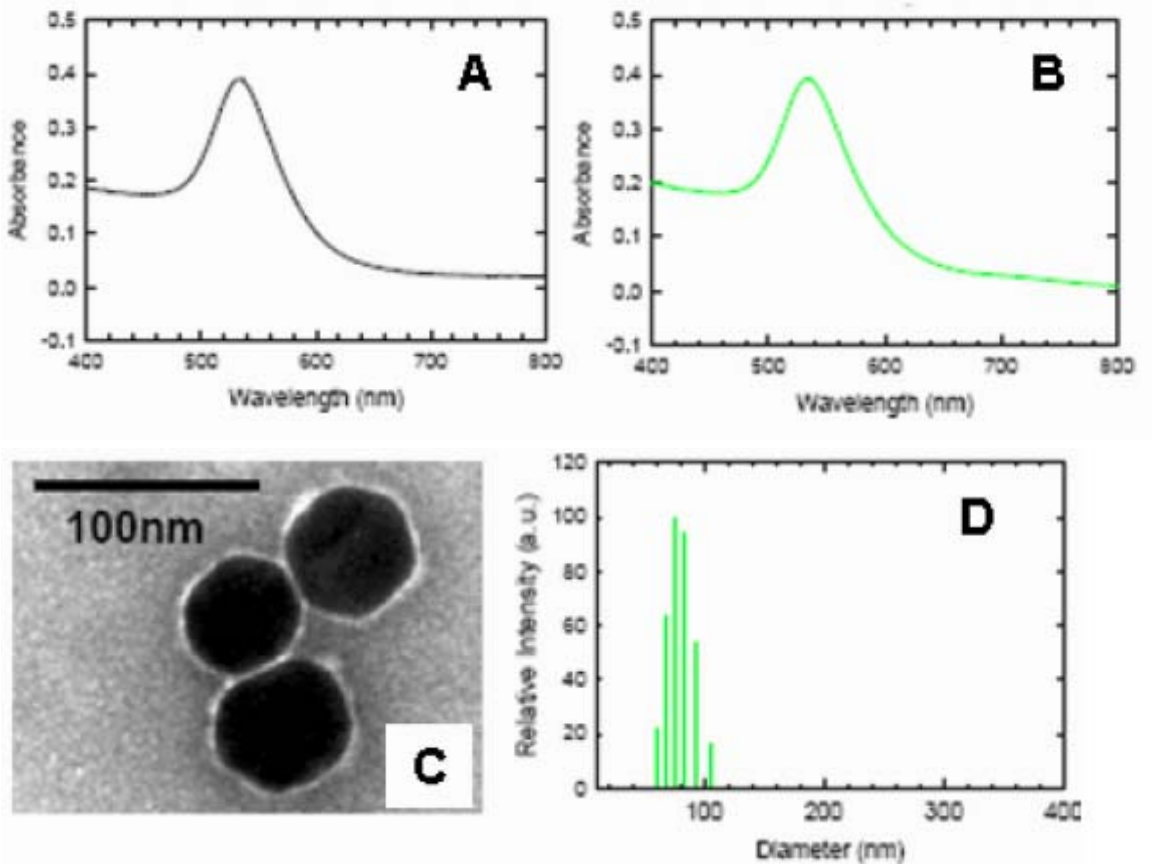

Figure 3.4: Characterization of PRENT aggregation state. UV-vis absorption spectra of 60 nm AuNPs **(A)** and MGITC encoded PRENTs **(B).** TEM image **(C)** and dynamic light scattering size distribution **(D)** of MGITC encoded PRENTs.

because PEG has a higher refractive index than water. Although MGITC possesses strong absorption in the 550-700 nm spectral region, the amount of adsorbed dye was low enough for the Au plasmon absorption band to mask the MGITC absorption band. Negatively stained transmission electron microscopy (TEM) images of PRENTs showed roughly spherical AuNP cores with a mean diameter of ~60 nm encapsulated with a ~ 5 nm thick PEG corona (**Figure 3.4C**). The proportion of dimers or higher order aggregates was approximately the same as those present in the unmodified AuNP solution. Dynamic light scattering data of PRENTs in water indicated a mean hydrodynamic size of ~75 nm with a unimodal size distribution (**Figure 3.4D**).

The efficacy of PEG's protective properties depends upon its density on the nanoparticle surface. In comparison to isolated "mushroom" chain configurations, dense polymeric "brushes" provide greater diffusional barriers to the nanoparticle core and increase the energy required for proteins to attach to the PEG-protected surfaces.[45] The minimum protective surface density of grafted PEG-SH was estimated by observing color changes before and after the resulting PRENTs were redispersed in 10-fold concentrated phosphate buffered saline (10X PBS). In the absence of PEG protection AuNP-reporter complexes rapidly aggregated and precipitated out of solution and the solution color changed from pink to blue (here the human eye serves as a visible absorbance spectrometer). A minimum ratio of 30,000 PEG-SH (5000 MW) per NP was required for long-term (> 3 days) protection in 10X PBS. Assuming that all of the added PEG-SH was able to bind to the AuNP, each PEG-SH polymer occupied an area (a "footprint") of 0.38 nm^2 on the NP surface. This finding is very close to a previously estimated footprint

of 0.35 nm^2 for 5000 MW PEG-SH adsorbed on unmodified AuNPs in a "brush" (high surface density, extended coil) conformation.[10] These results suggest that the presence of surface bound MGITC does not have a major effect on the binding of PEG-SH and that the surface coverage of MGITC is much less than a monolayer. Addition of PEG-SH at ratios up to 300,000 PEG-SH per NP did not cause any change in the aggregation state or the spectral signatures of PRENTs (**Figure 3.3**).

Protection from extreme conditions

We investigated the effect of a variety of harsh chemical conditions on the spectral signatures and aggregation states of PRENTs. The susceptibility of fluorescent dye emission spectra to pH and ionic environment is well known. Recently developed polymer-protected quantum dots aggregate at basic pH and in alcohols and there are spectral changes at acidic pH or at high salt concentrations.[46] MGITC encoded PRENTs were pelleted by centrifugation, redispersed in new solvents, and examined by Raman spectroscopy (**Figure 3.5 left column**) and absorbance spectroscopy (**Figure 3.5 right column**). There was no dramatic spectral signature change or change in aggregation state when the PRENTs were redispersed in 10-fold concentrated PBS (1.37 M NaCl, **Figure 3.5B**), acidic water (pH 2, **Figure 3.5C**), basic water (pH 14, **Figure 3.5D**), methanol (**Figure 3.5E**), and ethanol (**Figure 3.5F**) compared with the reference spectrum of Au-MGITC in water (**Figure 3.5A**). At pH 2, we did notice a slight change in relative peak intensities of the Raman bands at 1615

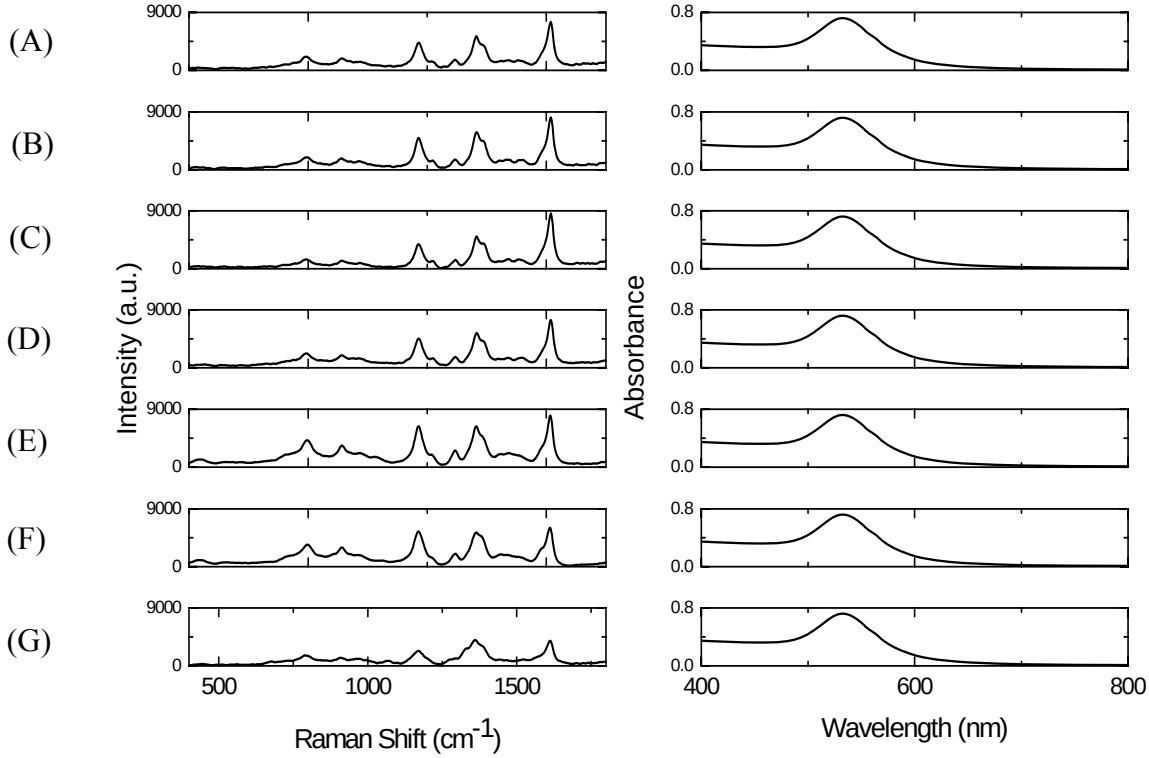

Figure 3.5: Stability of PRENTs under harsh chemical conditions. Raman scattering spectra (left) and absorption spectra (right) of MGITC-encoded PRENTs pelleted and redispersed in pure water (A), 10-fold concentrated phosphate buffered saline (1.37 M NaCl) (**B**), 0.01 M hydrochloric acid (pH 2) (**C**) 1 M sodium hydroxide (pH 14), (**D**), methanol (**E**), ethanol (**F**), dimethyl sulfoxide: tetrahydrofuran (50:50), then transferred back to water (G)

cm^{-1}, 1365 cm^{-1}, and 1172 cm^{-1} possibly due to a relative orientation change of MGITC on the Au surface[47], but no shift in vibrational frequencies was observed at any of the tested conditions. Redispersion of PRENTs in a mixture of dimethylsulfoxide (DMSO) and tetrahydrofuran (THF) masked the spectral features of the reporter due to the strong Raman cross section of DMSO. Interestingly, the original MGITC spectral signature was recovered after the DMSO/THF solvated PRENT was stored under ambient conditions for 60 days and then redispersed in water. (**Figure 3.5G**) Although unprotected Au-MGITC readily aggregated upon centrifugation, the aggregation state of the PRENTs did not change under any of the tested conditions (**Figure 3.5 right column**). In contrast to protein coated SERS tags,[48] these results clearly demonstrate the suitability of the PRENTs for a variety of bioconjugation, cell labeling, and storage procedures.

Photophysical properties

To further assess the potential of PRENTs as optical tags for in vitro diagnostics, and cellular and *in vivo* imaging, the photophysical properties of MGITC –encoded PRENTs and semiconductor quantum dots (QDs) that emit fluorescence in the same spectral region were compared. QDs are generally regarded as a gold standard for brightness and photostability in a variety of biological assays.[49] When illuminated continuously with laser light (633 nm excitation, 3 mW), MGITC-encoded PRENTs were remarkably photostable in comparison to commercially available far red QDs (peak fluorescence

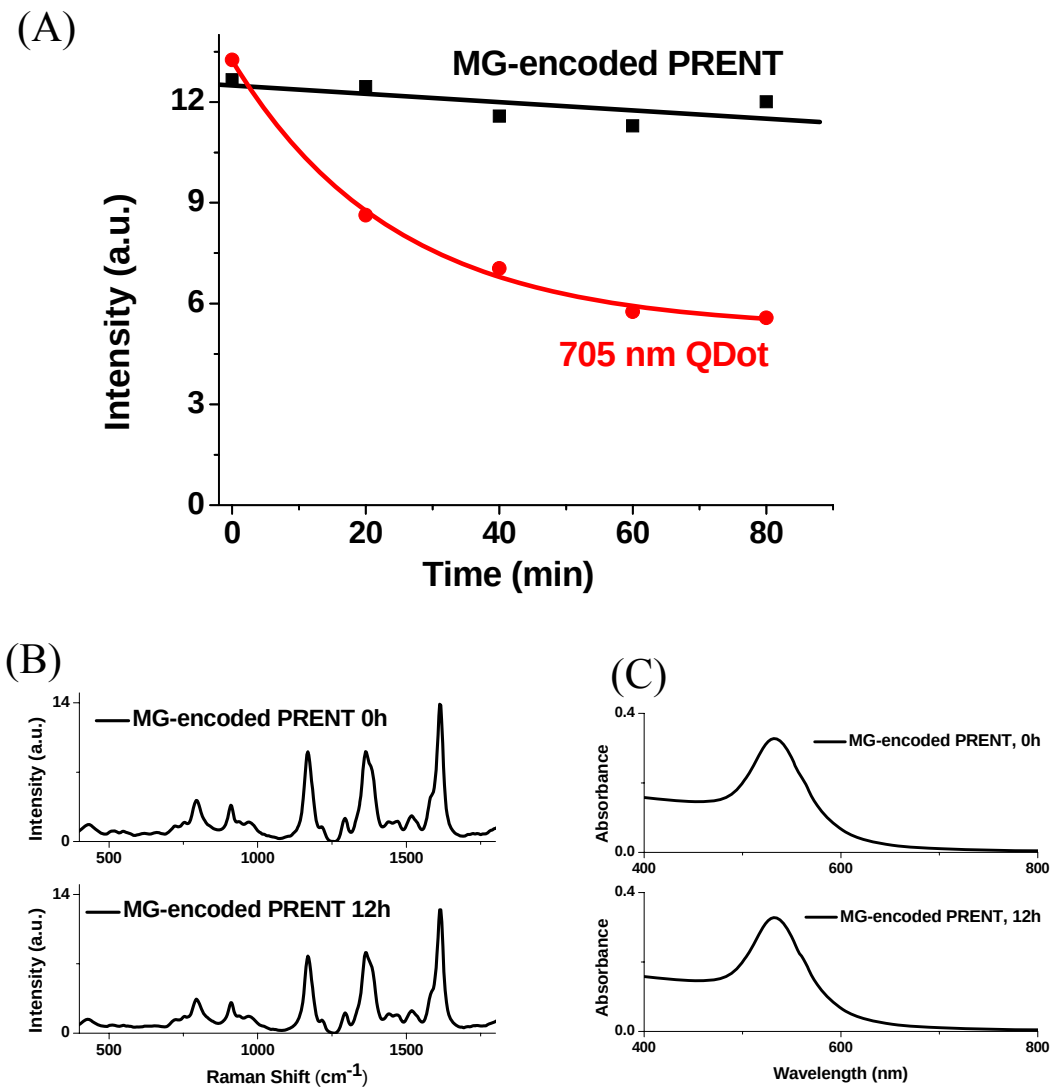

Figure 3.6: Stability of PRENTs and far-red quantum dots to prolonged illumination. Photobleaching kinetics of MG-encoded PRENTs (black squares) and 705 nm QDs (red circles). The curves are drawn only to guide the eye. (**A**) Raman scattering (**B**) and absorption spectra (**C**) of MG-encoded PRENTs after 0 hours (**top**) and 12 hours (**bottom**) of continuous laser illumination.

emission 705 nm, Invitrogen). At the end of an 80-minute illumination period under identical conditions, the intensities of PRENTs and quantum dots had decreased to ~95% and ~42% of their initial values, respectively (**Figure 3.6A**) These values remained the same after solutions were vortexed. Continuous illumination for 12 hours did not change the vibrational frequencies of the PRENT spectral signature and the signal intensity had decreased by only ~10% (**Figure 3.6B**). QD photostability is usually related to maintenance of a relatively large bandgap shell protecting the nanocrystal core,[50] although the mechanism underlying the rapid quantum dot photodegradation in this study has not been determined. The absence of spectral changes and the negligible photobleaching of PRENTs may be attributed to the extremely short lifetime of Raman scattering[51,52] and AuNP-induced quenching[53,54] that limits degradative reactions of the reporter's excited state.

Under identical experimental conditions, a solution of MGITC-encoded PRENTs was 92.3 times brighter than an equimolar solution of far-red QDs (**Figure 3.7A)** over a spectral region spanning 2800 cm^{-1} (from 641 nm to 781 nm) (**Figure 3.7B**). These findings were corroborated by single nanoparticle microscopic measurements of PRENTs and QDs (**Figure 3.7C** and **D**, respectively) immobilized on a glass coverslip. The MGITC-PRENTs were only about 3.5 times as large as the 705 nm QDs; the TEM diameters (mean +/- standard deviation) of the PRENTs and QDs were 77.3+/-8.4 nm and 22.3 +/- 1.4 nm, respectively (Figures **3.7E** and **F**). These results suggest that PRENTs would confer greater detection sensitivity than QDs under conditions affected by steric

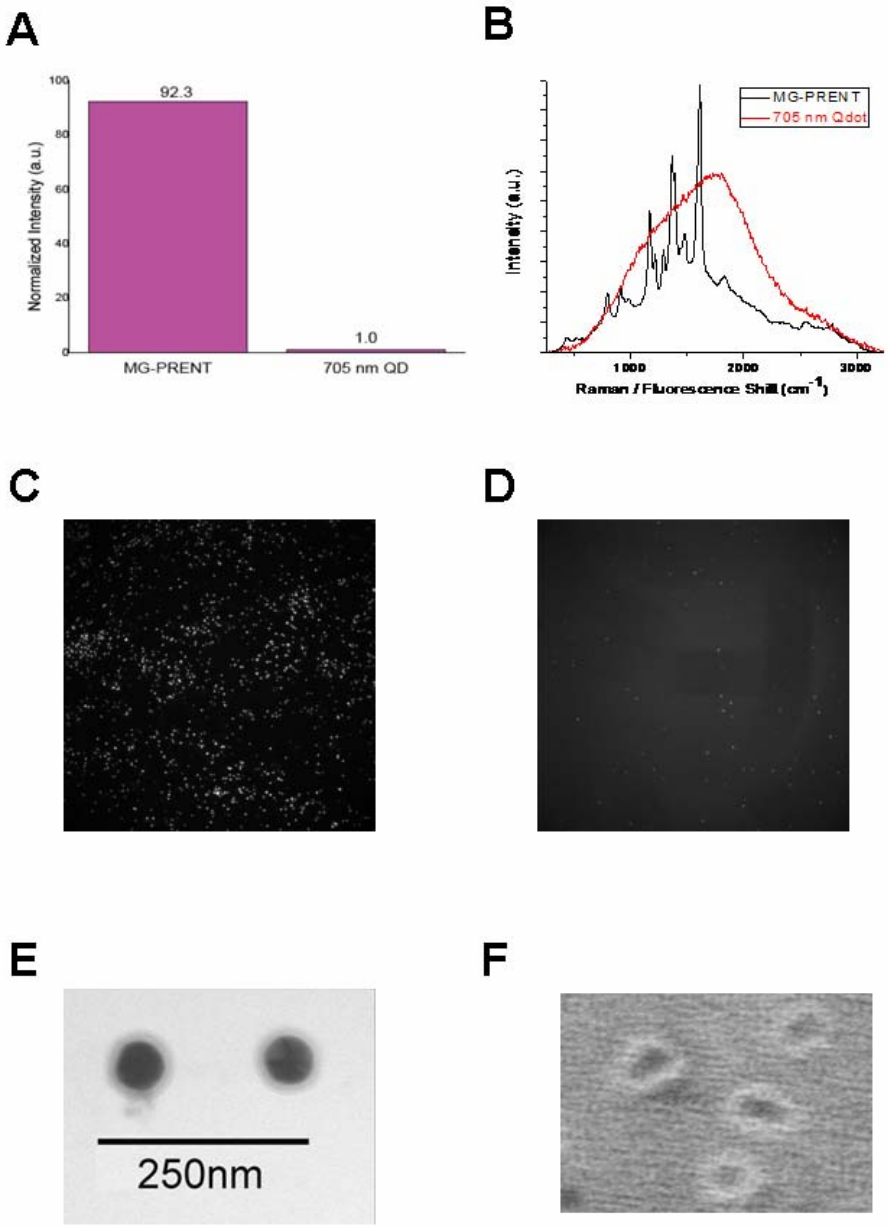

Figure 3.7: Brightness comparison of PRENTs and far-red quantum dots. Integrated spectral areas of MG-PRENTs and QDs excited by 633 nm laser light (**A**). Raw spectra of MG-PRENTs (black) and QDs (red) (**B**). TEM micrographs of MG-PRENTs (**C**) and 705 nm quantum dots (**D**) Raman scattering image of single PRENTs (**E**) and fluorescence emission image of single QDs (**F**) under identical experimental conditions.

hindrance such as those encountered in immunocytochemistry and immunosorbent assays.

Additional Raman reporters for diverse spectral signatures

PRENTs can be encoded with a broader range of reporter molecules than previously reported Raman tags. Following the experimental approach described for MGITC, we tested a variety of candidate reporters that possessed at least two of the following functional groups that have been shown to form stable associations with metal nanoparticles: organosulfur, alkylamine, positive charge, and delocalized pi electrons.[33,39,54,55] Of these potential interactions, the latter ones are generally regarded as quite weak in comparison to the covalent binding of sulfur with gold. **Figure 3.8** shows Raman spectral signatures of eight distinct PRENTs and the corresponding chemical structures of encapsulated reporters. In addition to the isothiocyanates MGITC and rhodamine B isothiocyanate (RBITC), PRENTs were successfully encoded with the non-sulfur containing molecules malachite green oxalate (MG), basic fuchsin (BF), crystal violet (CV), cresyl violet 670 perchlorate (CV670), and nile blue 690 perchlorate (NB690). In contrast, the use of reporter molecules lacking organosulfur functional groups in the preparation of silica coated Raman tags results in intensities too low for any practical use.[17,18] The Raman bands depicted in **Figure 3.8** are characteristic of the particular reporter and allow reproducible and unambiguous identification of each

PRENT. For example, the three triphenylmethane chromophores MG, CV, and BF are nearly identical in structure yet their respective encoded PRENTs have unique spectral features that can be distinguished by either a trained eye or computer algorithm. PRENTs encoded with malachite green lacking sulfur (MG) produced the same Raman spectral signature as PRENTs encoded with the isothiocyanate derivative (MGITC). MG-encoded PRENTs were as stable as MGITC-encoded PRENTs in high salt buffer and the presence of 10-fold excess PEG-SH for several weeks did not cause displacement of MG from the NP surface. The major interaction of MG/MGITC with AuNPs most likely occurs through its delocalized pi electrons. It is also possible that the reporters bind electrostatically to a negatively charged ligand already present on the AuNP surface. Each PRENT was reasonably bright when excited with 633 nm light. Successful encoding with non-organosulfur reporters allows a larger pool of potential Raman reporters and drives down the cost and complexity of PRENT preparation. For example, MG is over 17,000 times less costly than MGITC by weight and can be stored long term under ambient conditions. The fact that multiple PRENTs can be efficiently excited at a single wavelength increases the probability of success for developing molecular diagnostic assays and underscores the potential of this class of optical tags for combinatorial coding and multiplexed analyses.

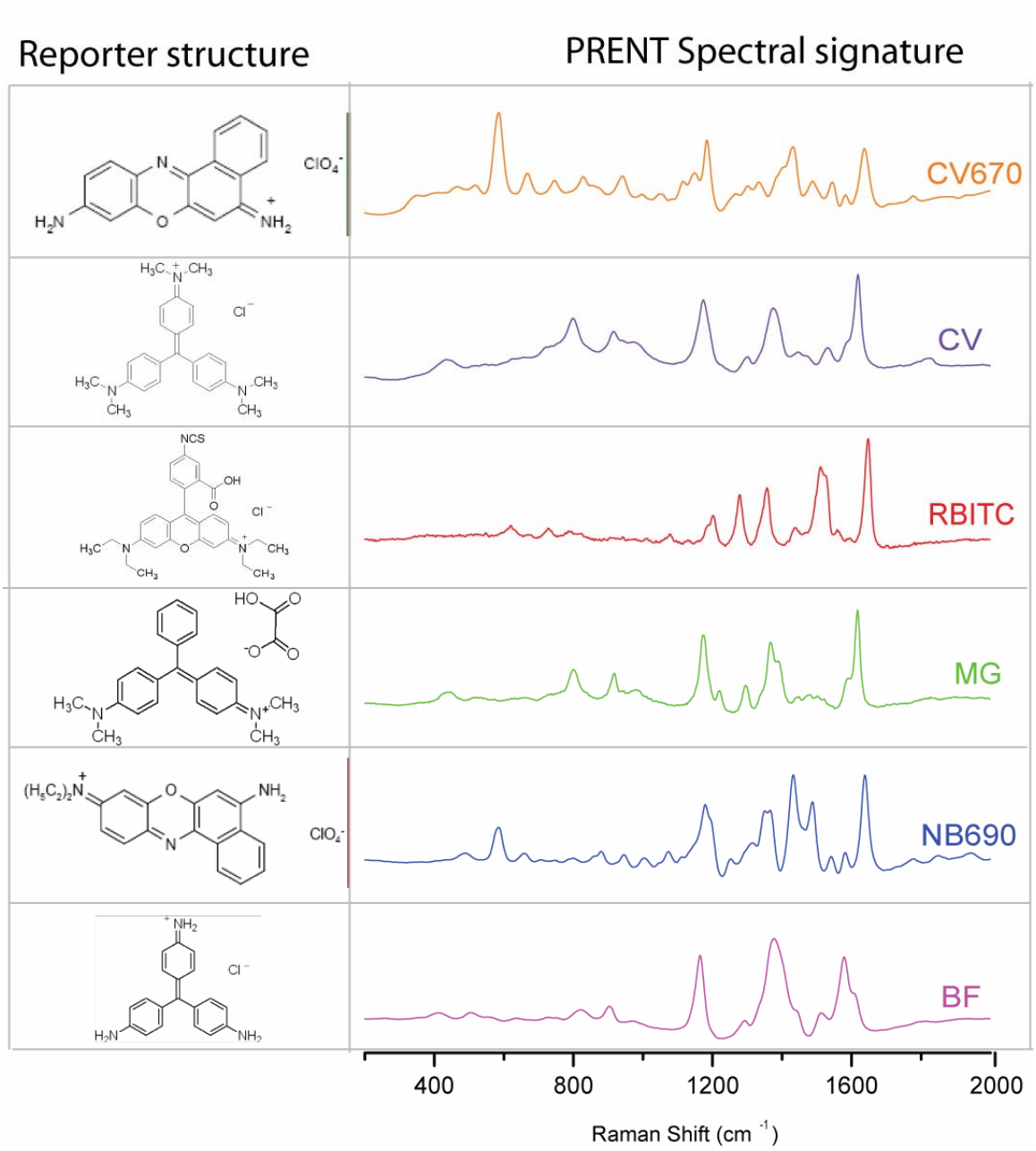

Figure 3.8: Effect of reporter chemical structure on PRENT spectral signature. Chemical structures of embedded reporters (left) and Raman spectra of PRENTS (right) encoded with cresyl violet 670 perchlorate (**CV670**), crystal violet (**CV**), rhodamine B isothiocyanate (**RBITC**), malachite green oxalate (**MG**), nile blue 690 perchlorate (**NB690**), and basic fuchsin (**BF**).

PEG-SH stabilization of reporter-Au interaction

Since PEG-SH is capable of displacing alkanethiols and thiolated oligonucleotides[56] that are generally assumed to possess stronger affinity to AuNPs than some of the reporters used in this study, the mechanism underlying the stabilization of the reporters by PEG-SH (**Figures 3.3** and **3.8**) was initially unclear. The two most plausible explanations were:

1) The reporter binds to surface sites on the AuNP that are distinct from the PEG-SH binding sites.
2) The reporter and PEG-SH compete for the same surface binding sites but the PEG-SH sterically traps desorbed reporters in close proximity to the Au surface.

To distinguish these possible mechanisms, we incubated Au-MG and Au-MGITC complexes (10,000 reporters per NP) with 2-mercaptoethanol (ME), a low molecular weight (~78) thiol compound that does not possess the large steric bulk of PEG-SH, and asked whether ME could displace the reporters from AuNPs. **Figure 3.9 A and B** show that ME treatment (30,000 ME molecules per NP) caused a dramatic reduction in SERS from both MGITC and MG capped AuNPs, respectively. (Note that the presence of a thiol group is necessary for PEG-SH protection of Au-reporter complexes. Treatment with non-thiol-derivatized PEG-SH did not protect the complexes from aggregation by the harsh chemical conditions described in **Figure 3.5)**. ME treatment did not aggregate the Au reporter complexes as evidenced by a lack of solution color change. To rule out the possibility that the observed spectral changes resulted not from desorption but from

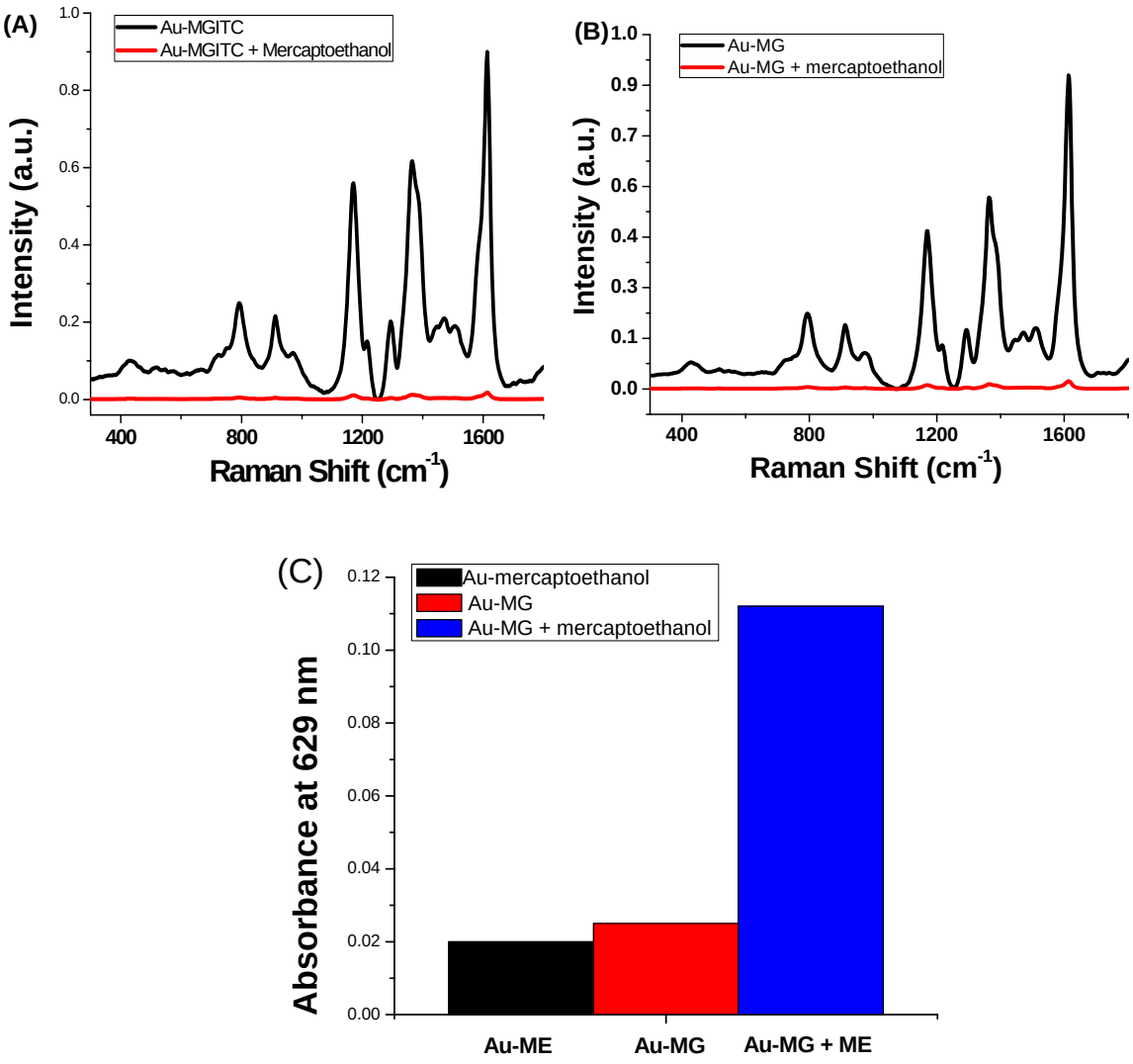

Figure 3.9: Effect of mercaptoethanol on AuNP-reporter complexes. Raman scattering spectra of AuNP-MGITC in the absence (black) and the presence (red) of mercaptoethanol (A), and AuNP-MG in the absence (black) and the presence (red) of mercaptoethanol (B). Absorbance at 629 nm of supernatants obtained from pelleting preparations of AuNP incubated with mercaptoethanol (black), AuNP-MG (red) and AuNP-MG incubated with mercaptoethanol (blue) (C).

reporter chemical modification by ME, mixtures of AuNPs and ME, AuNPs and MGITC, and AuNPs, MGITC, and ME were centrifuged and the absorbance of the supernatants was measured at the absorbance maximum of MGITC (629 nm). AuNPs and any stably adsorbates were visibly pelleted and the solution color changed from pink to clear. The supernatant of the Au-MGITC-ME mixture showed greater than ~5-fold absorbance than the supernatants of the Au-ME and Au-MGITC mixtures (**Figure 3.9C**), indicating the displacement of MGITC from the AuNP surface by ME. Taken together, the results in **Figure 3.9** suggest that PEG-SH protects complexes of AuNPs and reporters by its tight binding and steric bulk rather than by binding to distinct surface sites. Both MGITC and MG lacking an organosulfur group can be displaced from the AuNP by ME, suggesting that the same NP surface sites can bind to both sulfur and reporter. In addition, the results suggest that the poor encoding of non-organosulfur reporters in silica coated Raman tags is most likely due to displacement of the NP-bound Raman reporters by the low molecular weight (~179) thiol and amine-terminated silica coupling agents.[17,18]

Protection from surface contamination

Because of the high sensitivity of SERS and the potential of PRENTs for multiplexed assays, we also asked whether external molecules could penetrate the PEG layer of PRENTs and compete for adsorption to the gold surface, thereby decreasing intensity of the spectral signature or causing uncontrolled spectral changes. We added competing reporter molecules to both basic fuchsin (BF) encoded PRENTs and unprotected

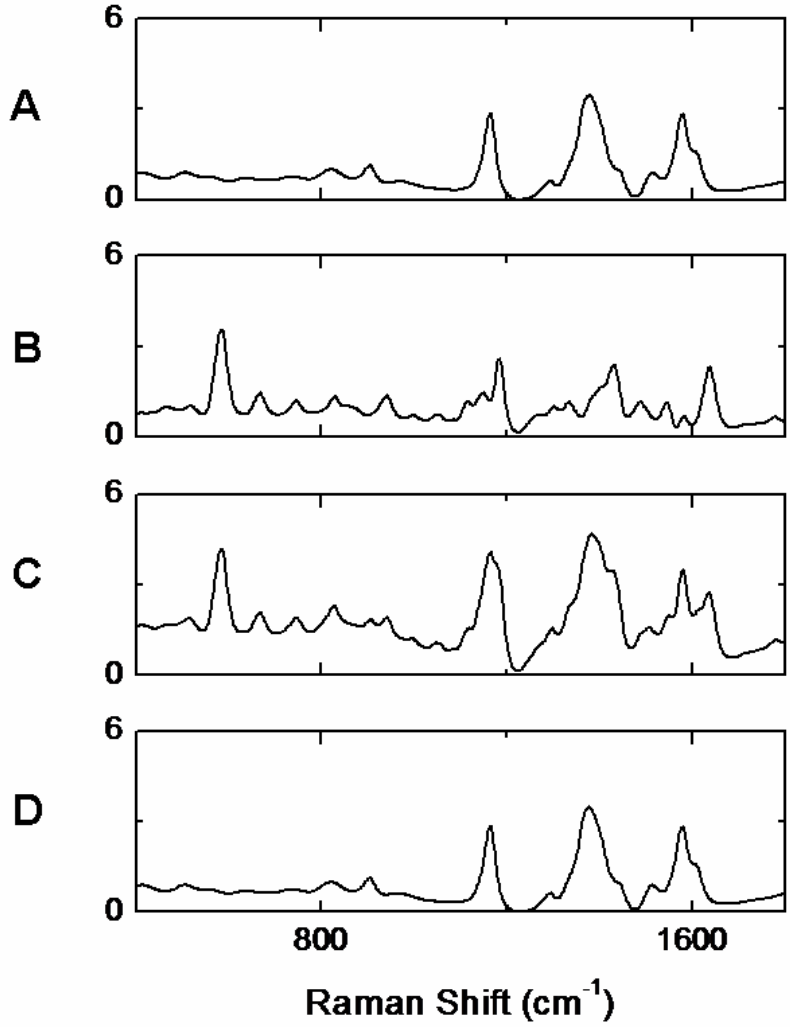

Figure 3.10. Effect of grafted PEG-SH on spectral interference by competing Raman-active species. Raman scattering spectra **of** Au nanoparticles mixed with BF reporter solution (A), Au nanoparticles mixed with CV670 reporter solution (B), Au nanoparticles mixed with BF reporter and CV670 reporter solutions (C), BF-encoded PRENTs mixed with CV670 reporter solution (D).

AuNP-BF complexes and obtained Raman spectra of the resulting mixtures. When cresyl violet 670 (CV670) was added to a solution of BF encoded PRENTs, the BF spectral signature was preserved and no CV670 spectral features were observed (**Figure 3.10D**). This finding suggests that the grafted PEG-SH monolayer blocks the access of free reporter molecules to the gold surface, and is consistent with the results of Wuelfing, et al, who reported that a grafted layer of PEG-SH could did not undergo place-exchange reactions with alkanethiols[10] However, addition of CV670 to a solution of uncoated AuNP-BF resulted in spectral contributions from CV670 that perturbed the spectral signature of BF (**Figure 3.10C**), suggesting that a biological assay employing improperly protected SERS tags is subject to spectral contamination by undesired Raman active species and underscoring the importance of a robust surface coating. Taken together, the findings in **Figures 3.5** and **3.10** suggest that the PEG monolayer of the PRENTs is permeable to solvent molecules and small ions but not large molecules such as organic chromophores, proteins, and oligonucleotides.

Cell surface biomarker detection using antibody-conjugated PRENTs

To demonstrate the potential of PRENTs as optical tags in cytometry applications, we prepared an antibody conjugated PRENT (A-PRENT) and used it to distinguish carcinoma from non-carcinoma cells in a suspension immunoassay. (**Figure 3.11**) We chose the cell surface glycoprotein EpCAM as a discriminatory biomarker because it is present in most human carcinomas, its overexpression in breast tumor cells is associated

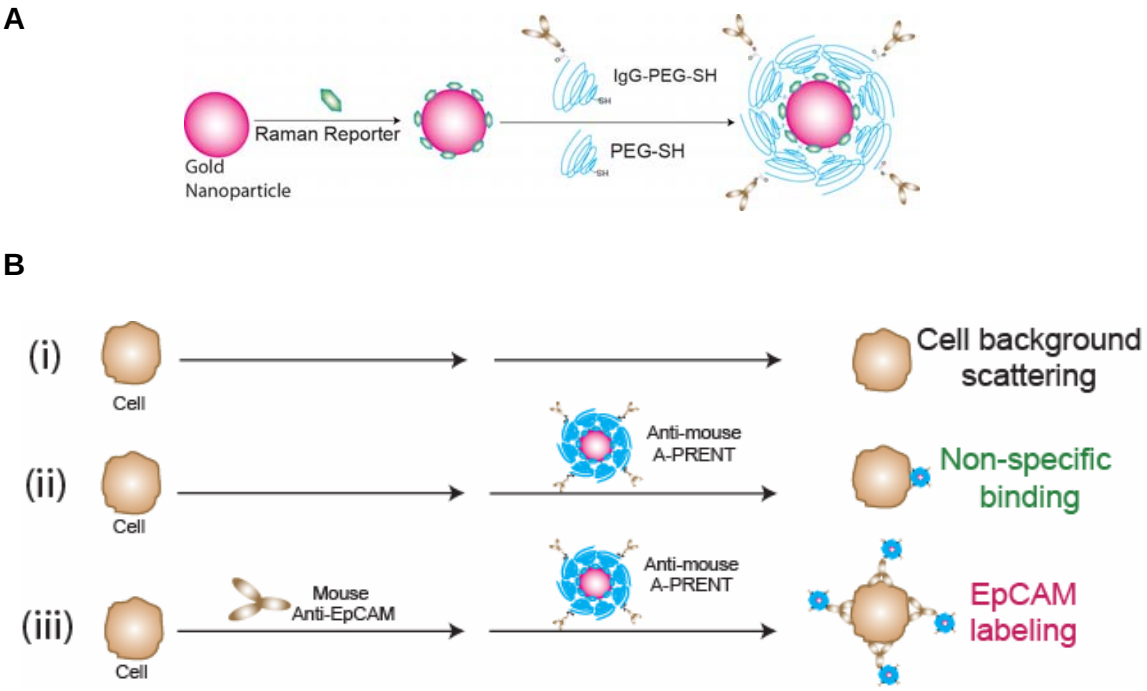

Figure 3.11. Schematic illustration of PRENT immunocytochemistry assay. (A) Schematic illustration of A-PRENT preparation. **(B)** Schematic illustration of cell tagging assay.

with poor prognosis and metastatic disease, and it is pursued as a therapeutic target for a variety of cancers.[57] Au-MGITC complexes were functionalized with PEG-SH-conjugated anti-mouse IgG (IgG-PEG-SH), then further protected with excess PEG-SH. We carefully controlled the reaction times of each step to avoid the possibility of place-exchange between PEG-SH and the surface bound IgG-PEG-SH. The use of heterobifunctional PEG containing an amine-reactive NHS ester on one end and a protected thiol on the other end enabled stable preparation of IgG-PEG-SH and one-step conjugation of antibody to the gold surface via the PEG linker.

Suspensions of living breast ductal carcinoma (BT474, EpCAM-positive[58]) and non-carcinoma (NIH/3T3, EpCAM-negative[59]) cells were blocked with bovine serum albumin, then incubated with a mouse monoclonal EpCAM antibody and anti-mouse IgG functionalized PRENT (A-PRENT, ~9000 PRENTs per cell) sequentially. The cells were washed exhaustively by centrifugation and resuspension in blocking buffer after each step. The immunoassay was performed at low temperature (4 ^{o}C) to guard against the possibility of internalization of either primary antibody or A-PRENT. EpCAM expression was measured by Raman spectroscopy using 633 nm excitation. The distinct MGITC spectral signature of labeled BT474 cells (**Figure 3.12A dark red spectrum**) and the absence of signature in the negative control reaction omitting the EpCAM primary antibody (**Figure 3.12A green spectrum**) demonstrates the negligible non-specific binding of the A-PRENT. The lack of MGITC spectral signature in EpCAM-negative NIH/3T3 cells (**Figure 3.12B**) further confirms specific EpCAM targeting.

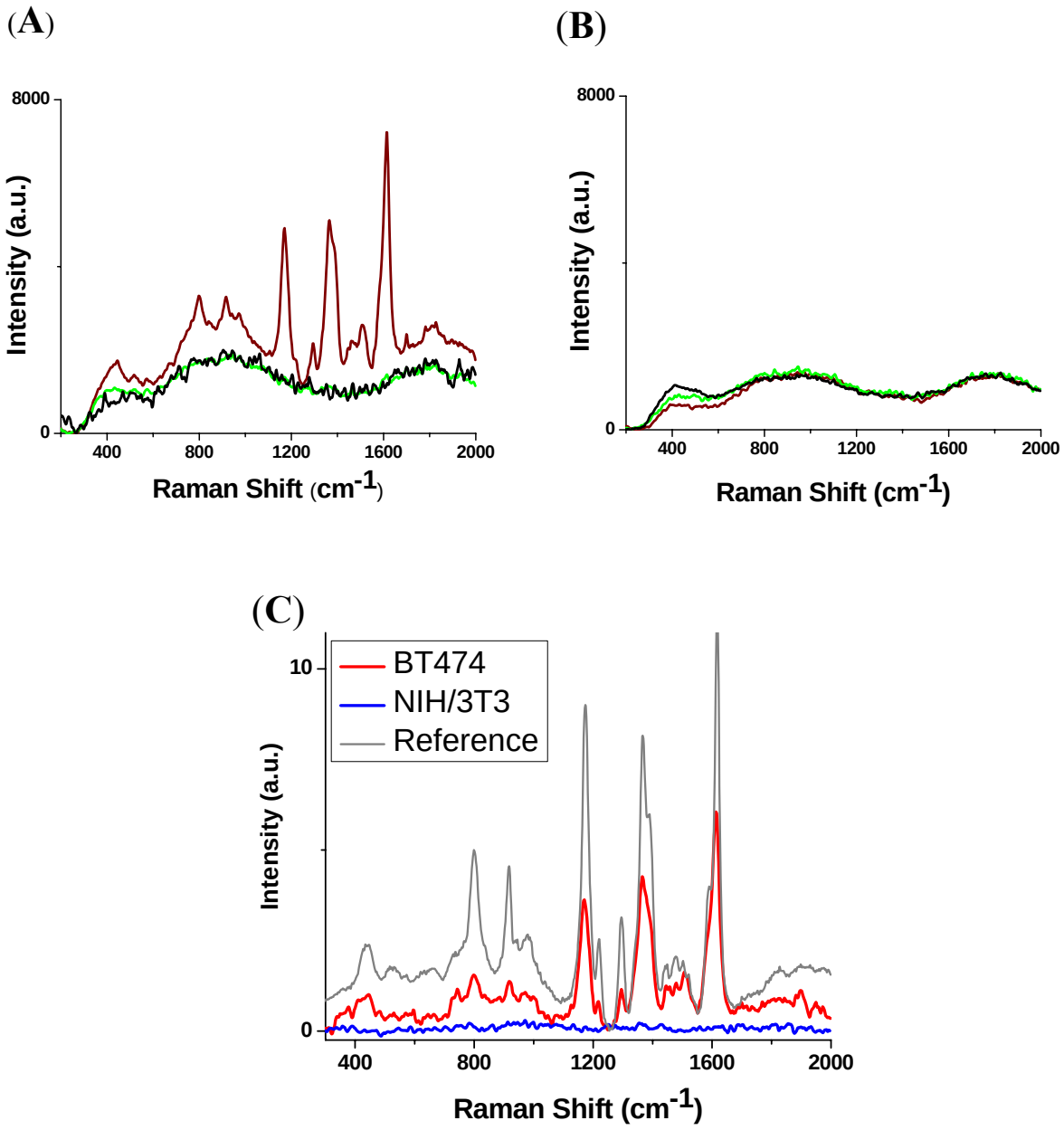

Figure 3.12: PRENT tagging of cell surface cancer biomarkers on living cells in suspension. Raman scattering spectra of BT474 breast carcinoma cells (**A**) and NIH/3T3 non-carcinoma cells (**B**) labeled with mouse monoclonal antibody against human EpCAM and secondary antibody functionalized, MGITC-encoded PRENT (MGITC-anti-mouse) (**dark red**), MGITC-anti-mouse alone (**green**), buffer lacking antibody containing reagents (**black**). (**C**) Background-subtracted Raman scattering spectra of PRENT-labeled BT474 cells (**red**), PRENT-labeled NIH/3T3 cells (**blue**), and an aqueous solution of MGITC-anti-mouse PRENTs (**grey**).

After background subtraction of the spectra of EpCAM-stained cells by the spectra of unprocessed cells (not stained with either primary antibody or A-PRENT), the spectral signature of background subtracted BT474 cells (red) matched exactly with the spectrum of pure MGITC-encoded PRENTs (black) and the background subtracted NIH/3T3 cells (blue) did not exhibit a spectral signature above the determination limit of the assay. Based on a cell density of 2×10^6 cells per cm^3, we estimated that the collection volume recorded by the spectrometer contained ~40 labeled cells. We did not observe changes in either spectral signature or intensity upon repeated examination of each unfixed sample (at least 3 times) over a period of 3 days and upon fixation in buffered formaldehyde solution. These reproducible measurements demonstrate the stability of Raman signals from cell membrane bound PRENTs and indicate the potential of this technology for practical cytometry applications such as the molecular profiling of low-abundance biomarkers in circulating tumor cells.

Biocompatibility of PRENTs

In contrast to gold compounds[60] and QDs,[61,62] the gold (Au^0) NPs that are the major component of PRENTSs are generally non-toxic to mammalian cells[13,63,64] and living animals.[65,66,15] Polyethylene glycols are famously biocompatible.[67] At the concentrations we have used for molecular detection, the unlikely event of complete breakdown of MG-encoded PRENTs by living cells would result in an MG solution concentration of ~ 300 nM, a concentration that has a negligible effect on cell viability after 24 h incubation.[68]

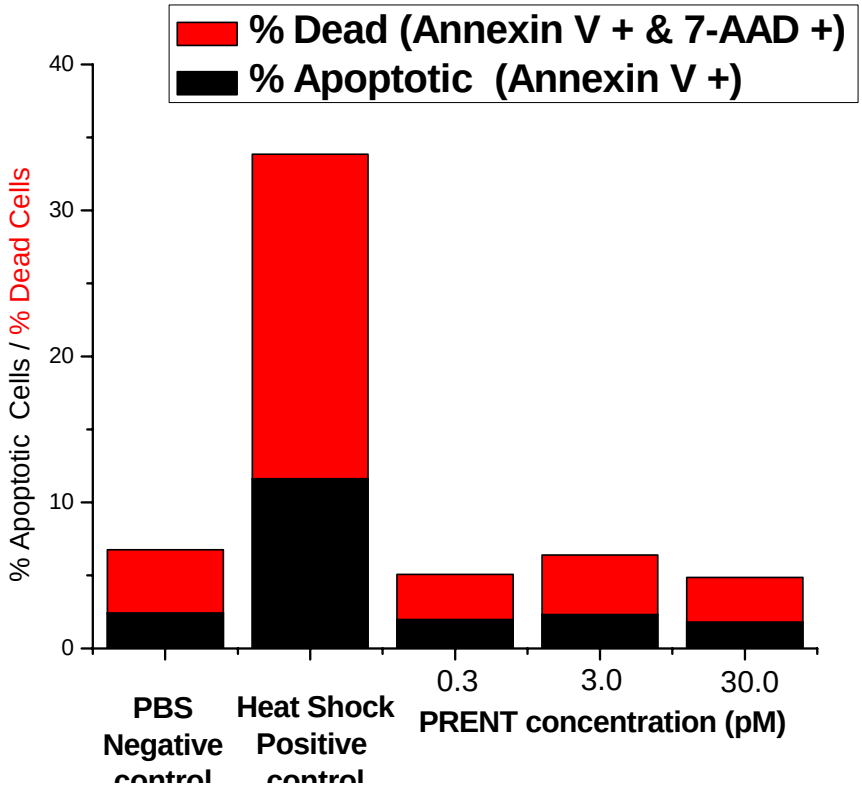

Figure 3.13: Effect of MG-encoded PRENTs on apoptosis induction and viability of cultured cells. Percentage of NIH/3T3 cells (n = 10^4) stained by Annexin V but not by 7-amino actinomysin (**black**) and percentage of cells stained by both Annexin V and 7-amino actinomysin (**red**).

Nevertheless, toxicity depends on both physicochemical and environmental factors and it is important to test the material in question in its exact form and under conditions that match as closely as possible to the setting of its intended application

We assessed the cytotoxicity of PRENTs under conditions exceeding those required for sensitive molecular detection by treating a monolayer of NIH/3T3 cells with 0.3-30 pM filter-sterilized MG-encoded PRENTs (~900 to ~90,000 PRENTs per cell) for 24 h under standard cell culturing conditions (37 ^{o}C, pH 7.4, 5% CO_2). The degree of apoptosis and cell death was determined according to established procedures.[69] .After incubation, the cells were harvested into suspension, washed, and stained with Annexin V conjugated to phycoerythrin fluorochrome (AV-PE) and the vital exclusion dye 7-amino-actinomysin D (7-AAD). Analysis by flow cytometry indicated that the PRENTs did not induce a greater level of early apoptosis (AV-PE positive, 7-AAD-negative) or cell death (AV-PE positive, 7-AAD positive) than the PBS vehicle (**Figure 3.13**). The morphology of cells treated with PRENTs did not appear different than those treated with PBS vehicle. These data demonstrate that PRENTs do not adversely affect cell behavior or viability and have important implications for live cell optical detection and imaging with PRENTs.

3.3 Conclusions

We have developed a new class of SERS based optical tags termed polymer-protected Raman-encoded nanoparticle tags (PRENTs). Compared to other classes of fluorescent

tags such as organic fluorophores and QDs, the design and preparation of PRENTs with diverse spectral signatures is simple and modular. PRENTs are better protected than protein-protected SERS tags and do not show changes in spectral signature or aggregation state when exposed to harsh chemical conditions or prolonged illumination. PRENTs incorporate a broader class of reporters than silica-encapsulated SERS tags. They are nearly two orders of magnitude brighter than quantum dots while their size is only about 3.5 times as large. Antibody-functionalized PRENTs enable specific targeting and Raman detection of biomolecules on the surface of living cancer cells at reasonable integration times. PRENTs are non-toxic to cells under conditions exceeding those required for molecular detection. Taken together, these findings suggest that PRENTs have the potential to become a new class of optical tags for applications in analytical chemistry, molecular biology, and medical diagnostics.

3.4 Materials and Methods

Materials

Ultrapure water (18 MΩ cm^{-1}) was used to prepare all aqueous solutions. The following materials were used without further purification: 60 nm gold particles (2.6×10^{10} particles/mL) (British Biocell International); malachite green isothiocyanate (MGITC), 4',6-diamidino-2-phenylindole (DAPI) dilactate, and 705 nm quantum dot conjugate (Invitrogen Corporation), cresyl violet 670 perchlorate and nile blue 690 perchlorate (Exciton), mPEG-SH and mPEG-OMe (MW ~ 5,000 Da) (Nektar

Therapeutics), S-acety1-poly(ethylene glycol)-NHS ester (PEG-SATA, Quanta Biodesign), NAP-5 columns (containing Sephadex G-25, GE Healthcare). BT474 and NIH/3T3 cells were obtained from the American Type Culture Collection (ATCC). Cell culture media, fetal bovine serum, hemacytometer, and cell culture supplies were purchased from Fisher Scientific. Annexin V-phycoerythrin and 7-amino-actinomysin D were obtained from BD Biosciences. All other reagents were obtained from Sigma-Aldrich at the highest purity available.

All experiments were performed at room temperature unless otherwise specified.

Measurements

UV-Vis absorption spectra were recorded on a Shimadzu UV-2401 spectrometer. Disposable polyacryl cuvettes with 1cm optical path length were used in all UV-Vis measurements. Transmission electron micrographs were taken using a Hitachi H7500 high-magnification electron microscope. 5 μL of sample was dropped onto copper 200 mesh grids that were pre-treated with UV light to reduce the static electricity. After 30 min, the solvent was drained with filter paper and 1% phosphotungstic acid stain (adjusted to pH 6) was applied for 30s. Particle sizes were determined with Image J software. Dynamic light scattering data were obtained from particle size analyzer instrument (Brookhaven 90Plus). Each sample was measured three times consecutively. Raman scattering and fluorescence emission spectra were recorded with an Advantage 200A Raman spectrometer (DeltaNu) using 633nm (3mW) excitation. The laser beam diameter was 35 μm at the focal point. We estimated the spectrometer collection volume

to be ~1.9×10^{-5} cm^3. Raman intensities of samples were normalized to the Raman spectrum of cyclohexane to control for any variations in instrument response. The instrument resolution was 5 cm^{-1}. Spectra were processed and analyzed in Origin software (Origin Lab Corp.). Note that the spectra consist of sharp Raman spectral bands (1-2 nm FWHM) and a concomitant broad underlying continuum noted by other SERS workers.[69] In most cases the continuum was removed mathematically (Fourier transforms or derivative methods) and did not affect the results or conclusions in this work. Fluorescence emission data from cells were recorded with a FACScan flow cytometer (Becton Dickinson) using 488 nm excitation and the instrument's built-in optical filter sets. Data were analyzed in FloJo software (Tree Star, Inc)

Polymer-protected Raman encoded nanoparticle tags (PRENTs)

Freshly prepared reporter solution was slowly added under rapid mixing with AuNPs to cover the NP surface and allow even distribution. The Au-reporter complexes were equilibrated in low-light conditions from 15 minutes to 24 hours, depending on reporter affinity for Au. The ratio of reporter molecules to Au particle was adjusted for each reporter to minimize aggregation. (example ratios: 14,000 MGITC per Au nanoparticle, 15,300 CV per Au particle) The volume ratio of stock reporter solution and gold nanoparticle solution was controlled to be 1:6. PEG-SH (10 μM) was added dropwise to the Au-reporter complex solution to achieve a final ratio of 300,000 PEG-SH per Au particle. Storage of PEG-SH under ambient conditions did not affect the results.

To test stability under harsh chemical conditions, the PRENTs were centrifuged at 1000g in a fixed angle-rotor and resuspended in various solvents.

Nanoparticle Imaging

Solutions of either MGITC-encoded PRENTs or PEG-coated quantum dots (705 nm peak fluorescence emission, Invitrogen) were spread onto a freshly cleaned coverglass and allowed to dry. Wide-field optical images were obtained with an inverted microscope (Olympus IX71). A halogen lamp and a band-pass filter (620nm DF60, Chroma) were used for excitation. Backscattered fluorescence and Stokes Raman signals were collected through a microscope objective (Plan 100×, oil immersion, NA= 1.4, Olympus) and passed through a 655 nm long pass filter (Chroma). Wide-field images were collected with an electron multiplier CCD camera (C900-12, Hamamatsu Photonics) and integrated for 500 ms. The majority of particles in both QD and SERS tags images were blinking. Image J software (U.S. National Institutes of Health) was used to analyze the images. Mean pixel gray value and area were measured for 18 randomly selected particles in each image. The mean integrated density (MID) for each particle was calculated as the product of mean pixel gray value and particle area. Each Particle MID was normalized to the MID of an equal-sized area of the coverglass that did not contain any particles. The plot shows the average normalized MID for SERS tags and QDs with standard deviation shown as error bars.

Antibody-conjugated PRENTs (A-PRENTs)

PEG-SATA was covalently conjugated to antibodies using standard conjugation chemistry.[70] To preserve the reactivity of the NHS ester in PEG-SATA, stock solutions were prepared in anhydrous DMSO under nitrogen. 25 μL PEG-SATA (125 μM in DMSO) was added to 387 μL goat anti-mouse IgG (~8.1 μM in sterile PBS) and thoroughly mixed over one hour period. Then, NH_2OH was mixed with IgG-PEG-SATA for 2 hours to deprotect the acetylated thiol groups. PEG-SATA, DMSO, and NH_2OH were immediately removed from IgG-PEG-SH by gel filtration on a Sephadex G-25 column using 1.8 mM K_2CO_3 as the chromatography buffer. After purification, the antibody concentration was estimated by absorbance at 280 nm and conjugation success was verified by centrifugation in 10% PEG (8000 MW) and treatment with (DTNB, Ellman's reagent). A yellow color indicated the attachment of PEG-SH to the antibody. The ratio of thiol groups to IgG molecules was ~ 0.7. Unconjugated IgG was used as a baseline in the absorbance assay. Conjugation of IgG-PEG-SH to Au-reporter complexes was carried out in 1.8 mM K_2CO_3. 250 μL IgG-PEG-SH (498 nM) was added dropwise to 6.1 mL Au-MGITC solution (3×10^{11} total Au particles) in a polypropylene tube under rapid mixing. The Au-MGITC was thoroughly mixed with IgG-PEG-SH for 2 hours, then with 250 μL PEG-SH (34.2 μM) for 10 min to protect any exposed regions of the Au surface. (Final ratio: 576 IgG-PEG-SH and 40,000 PEG-SH per Au particle). The resulting A-PRENT was purified by 4 rounds of centrifugation at 1000g and resuspension in 0.1% BSA in PBS. The A-PRENT was sterilized by filtering through a 0.2 micron filter and stored at 4 ^{o}C. Serial dilutions of the A-PRENT prior to purification were used to construct a linear calibration curve of absorbance at 530 nm as a function of the AuNP concentration. The stock AuNP concentration was provided by the manufacturer. A-

PRENT concentrations were estimated by assuming that each A-PRENT conjugate contained one AuNP.

Immunocytochemistry

BT474 and NIH/3T3 cells were cultured in RPMI-1640 + 10% fetal bovine serum and DMEM + 10% calf bovine serum, respectively, in a 5% CO_2 atmosphere at 37 ^oC. The cells were grown to confluence and harvested by gentle scraping. Cell staining procedures were performed under sterile conditions at 4 ^oC. The following solutions were used: Washing Buffer (1% BSA, 15mM sodium azide in PBS), Blocking Buffer (2.5% goat serum, 1% BSA, 15 mM sodium azide in PBS). Cell suspensions were pelleted by centrifugation at 200g and washed in Washing Buffer. Cells were mixed with Blocking Buffer for 30 min, then mouse anti-EpCAM (6.25 μg/mL, diluted in Blocking Buffer) for one hour. After 4 rounds of centrifugation and resuspension in Washing Buffer, cells were mixed with MGITC encoded, anti-mouse PRENTs (20 pM, diluted in Blocking Buffer) for one hour. The cells were subjected to another 4 rounds of washing, resuspended in 500 μL Washing Buffer and examined by Raman spectroscopy. A portion of cells that did not receive the EpCAM primary antibody were used as controls to assess non-specific binding of A-PRENTs. An additional portion of cells received neither primary antibody nor A-PRENTs and were used as controls to assess background cell scattering. Raman spectra were normalized to cell concentrations. The integration time was 3 sec. Cell concentrations were determined by DAPI staining and counting fluorescent nuclei in a hemacytometer using Image J software.

Cytotoxicity assay

NIH/3T3 cells were seeded into 6-well plates (150,000 per well) and incubated for 2 days under the conditions described above to allow for adherence and growth to ~80% confluence. The conditioned medium was replaced with serum-free medium containing 0.3 – 30 pM MG-encoded PRENTs. After incubation for 24 h, PRENT-containing medium was removed and cells were rinsed thoroughly with PBS. Cells were gently harvested into suspension by treatment with a non-enzymatic cell dissociation solution (Sigma-Aldrich), then washed and diluted in 0.1% BSA in PBS. Annexin V-phycoerythrin conjugate and 7-aminoactinomysin were added to the cell suspension and incubated for 15 min. Cells were analyzed immediately by flow cytometry according to the manufacturer's instructions (BD Biosciences). Cells stained with both Annexin V-PE and 7-AAD were considered dead by either apoptosis or necrosis and cells stained only with Annexin V-PE were regarded as undergoing apoptosis but not yet dead.

3.5 References

1. Doering WE, Piotti ME, Natan MJ, Freeman RG. SERS as a foundation for nanoscale, optically detected biological labels. *Advanced Materials*. 2007;19(20):3100-3108.

2. Banholzer M, Millstone J, Qin L, Mirkin C. Rationally designed nanostructures for surface-enhanced Raman spectroscopy. *Chemical Society Reviews*. 2008;37(5):885-897.

3. Nie SM, Emery SR. Probing single molecules and single nanoparticles by surface-enhanced Raman scattering. *Science*. 1997;275(5303):1102-1106.

4. Kneipp K, Wang Y, Kneipp H, et al. Single molecule detection using surface-enhanced Raman scattering (SERS). *Physical Review Letters*. 1997;78(9):1667-1670.

5. Emory SR. Direct Observation of Size-Dependent Optical Enhancement in Single Metal Nanoparticles. *Journal of the American Chemical Society.* 1998;120(31):8009-8010.

6. Emory SR, Nie S. Screening and enrichment of metal nanoparticles with novel optical properties. *Journal of Physical Chemistry B*. 1998;102(3):493-497.

7. Michaels AM, Nirmal M, Brus LE. Surface enhanced Raman spectroscopy of individual rhodamine 6G molecules on large Ag nanocrystals. *Journal of the American Chemical Society*. 1999;121(43):9932-9939.

8. Storm G, Belliot SO, Daemen T, Lasic DD. Surface Modification of Nanoparticles to Oppose Uptake by the Mononuclear Phagocyte System. *Advanced Drug Delivery Reviews*. 1995;17(1):31-48.

9. Vonarbourg A, Passirani C, Saulnier P, Benoit J. Parameters influencing the stealthiness of colloidal drug delivery systems. *Biomaterials*. 2006;27(24):4356-4373.

10. Wuelfing WP, Gross SM, Miles DT, Murray RW. Nanometer gold clusters protected by surface-bound monolayers of thiolated poly(ethylene glycol) polymer electrolyte. *Journal of the American Chemical Society*. 1998;120(48):12696-12697.

11. Yu SF, Lee SB, Kang M, Martin CR. Size-based protein separations in poly(ethylene glycol)-derivatized gold nanotubule membranes. *Nano Letters*. 2001;1(9):495-498.

12. Loo C, Lowery A, Halas N, West J, Drezek R. Immunotargeted nanoshells for integrated cancer imaging and therapy. *Nano Letters*. 2005;5(4):709-711.

13. Surface functionalization of gold nanoparticles using hetero-bifunctional poly(ethylene glycol) spacer for intracellular tracking and delivery. Available at: http://www.pubmedcentral.nih.gov.proxy.library.emory.edu/articlerender.fcgi?artid=1351208 [Accessed August 22, 2008].

14. Paciotti GF, Kingston DGI, Tamarkin L. Colloidal gold nanoparticles: A novel nanoparticle platform for developing multifunctional tumor-targeted drug delivery vectors. *Drug Development Research*. 2006;67(1):47-54.

15. Paciotti GF, Myer L, Weinreich D, et al. Colloidal gold: A novel nanoparticle vector for tumor directed drug delivery. *Drug Delivery*. 2004;11(3):169-183.

16. Visaria RK, Griffin RJ, Williams BW, et al. Enhancement of tumor thermal therapy using gold nanoparticle-assisted tumor necrosis factor-alpha delivery. *Molecular Cancer Therapeutics*. 2006;5(4):1014-1020.

17. Mulvaney SP, Musick MD, Keating CD, Natan MJ. Glass-coated, analyte-tagged nanoparticles: A new tagging system based on detection with surface-enhanced Raman scattering. *Langmuir*. 2003;19(11):4784-4790.

18. Doering WE, Nie SM. Spectroscopic tags using dye-embedded nanoparticies and surface-enhanced Raman scattering. *Analytical Chemistry*. 2003;75(22):6171-6176.

19. Su X, Zhang J, Sun L, et al. Composite organic-inorganic nanoparticles (COINs) with chemically encoded optical signatures. *Nano Letters*. 2005;5(1):49-54.

20. Moskovits M. Surface-enhanced Raman spectroscopy: a brief retrospective. *Journal of Raman Spectroscopy*. 2005;36(6-7):485-496.

21. Kneipp K, Kneipp H, Itzkan I, Dasari RR, Feld MS. Surface-enhanced Raman scattering and biophysics. *Journal of Physics-Condensed Matter*. 2002;14(18):R597-R624.

22. Campion A, Kambhampati P. Surface-enhanced Raman scattering. *Chemical Society Reviews*. 1998;27(4):241-250.

23. Krug JT, Wang GD, Emory SR, Nie SM. Efficient Raman enhancement and intermittent light emission observed in single gold nanocrystals. *Journal of the American Chemical Society*. 1999;121(39):9208-9214.

24. Michaels AM, Jiang J, Brus L. Ag nanocrystal junctions as the site for surface-enhanced Raman scattering of single Rhodamine 6G molecules. *Journal of Physical Chemistry B*. 2000;104(50):11965-11971.

25. Doering WE, Nie SM. Single-molecule and single-nanoparticle SERS: Examining the roles of surface active sites and chemical enhancement. *Journal of Physical Chemistry B*. 2002;106(2):311-317.

26. Hildebrandt P, Stockburger M. Surface-Enhanced Resonance Raman-Spectroscopy of Rhodamine-6g Adsorbed on Colloidal Silver. *Journal of Physical Chemistry*. 1984;88(24):5935-5944.

27. Hayat MA. *Colloidal Gold: Principles, Methods, and Applications*. Academic Press; 1990.

28. Hayat MA. *Immunogold-Silver Staining*. CRC Press; 1995.

29. Nakata S, Kido N, Hayashi M, et al. Chemisorption of proteins and their thiol derivatives onto gold surfaces: characterization based on electrochemical nonlinearity. *Biophysical Chemistry*. 1996;62(1-3):63-72.

30. Brewer SH, Glomm WR, Johnson MC, Knag MK, Franzen S. Probing BSA binding to citrate-coated gold nanoparticles and surfaces. *Langmuir*. 2005;21(20):9303-9307.

31. Emory SR. Ph.D. Dissertation. Dept of Chemistry. 1999.

32. McCreery RL. *Raman Spectroscopy for Chemical Analysis*. New York: Wiley Interscience; 2000.

33. Nickel U, Halbig P, Gliemann H, Schneider S. Charge transfer like complexes of organic dyes adsorbed at colloidal silver studied by cyclic voltammetry, UV-vis and SERS spectroscopy. *Berichte Der Bunsen-Gesellschaft-Physical Chemistry Chemical Physics*. 1997;101(1):41-49.

34. Makarova OV, Ostafin AE, Miyoshi H, Norris JR, Meisel D. Adsorption and encapsulation of fluorescent probes in nanoparticles. *Journal of Physical Chemistry B*. 1999;103(43):9080-9084.

35. Mangeney C, Ferrage F, Aujard I, et al. Synthesis and properties of water-soluble gold colloids covalently derivatized with neutral polymer monolayers. *Journal of the American Chemical Society*. 2002;124(20):5811-5821.

36. Otsuka H, Akiyama Y, Nagasaki Y, Kataoka K. Quantitative and reversible lectin-induced association of gold nanoparticles modified with alpha-lactosyl-omega-mercapto-poly(ethylene glycol). *Journal of the American Chemical Society*. 2001;123(34):8226-8230.

37. Advincula RC/B. *Polymer Brushes: Synthesis, Characterization, Applications*. Weinheim: Wiley-VCH; 2004.

38. Shan J, Tenhu H. Recent advances in polymer protected gold nanoparticles: synthesis, properties and applications. *Chemical Communications*. 2007;(44):4580-4598.

39. Ulman A. Formation and Structure of Self-Assembled Monolayers. *Chem. Rev.* 1996;96(4):1533-1554.

40. Prime KL, Whitesides GM. Adsorption of Proteins Onto Surfaces Containing End-Attached Oligo(ethylene Oxide) - a Model System Using Self-Assembled Monolayers. *Journal of the American Chemical Society*. 1993;115(23):10714-10721.

41. Ostuni E, Chapman RG, Holmlin RE, Takayama S, Whitesides GM. A survey of structure-property relationships of surfaces that resist the adsorption of protein. *Langmuir*. 2001;17(18):5605-5620.

42. Hostetler MJ, Templeton AC, Murray RW. Dynamics of place-exchange reactions on monolayer-protected gold cluster molecules. *Langmuir*. 1999;15(11):3782-3789.

43. Tuma R. Raman spectroscopy of proteins: from peptides to large assemblies. *Journal of Raman Spectroscopy*. 2005;36(4):307-319.

44. Kozielski M, Muhle M, Blaszczak Z. The Raman scattering study of selected polyoxyethyleneglycols. *Journal of Molecular Liquids*. 2004;111(1-3):1-5.

45. Sheth SR, Leckband D. Measurements of attractive forces between proteins and end-grafted poly(ethylene glycol) chains. *Proceedings of the National Academy of Sciences of the United States of America*. 1997;94(16):8399-8404.

46. Invitrogen Corp. *http://www.invitrogen.com*.

47. Alderman DJ. Malachite Green - a Review. *Journal of Fish Diseases*. 1985;8(3):289-298.

48. Su X, Zhang J, Sun L, et al. Composite organic-inorganic nanoparticles (COINs) with chemically encoded optical signatures. *Nano Letters*. 2005;5(1):49-54.

49. Smith AM, Duan H, Mohs AM, Nie S. Bioconjugated quantum dots for in vivo molecular and cellular imaging. *Advanced Drug Delivery Reviews*. 2008;60:1226-1240.

50. Dabbousi BO, RodriguezViejo J, Mikulec FV, et al. (CdSe)ZnS core-shell quantum dots: Synthesis and characterization of a size series of highly luminescent nanocrystallites. *Journal of Physical Chemistry B*. 1997;101(46):9463-9475.

51. Harris JM, Chrisman RW, Lytle FE, Tobias RS. Sub-Nanosecond Time-Resolved Rejection of Fluorescence from Raman-Spectra. *Analytical Chemistry*. 1976;48(13):1937-1943.

52. Wirth MJ, Chou SH. Comparison of Time and Frequency-Domain Methods for Rejecting Fluorescence from Raman-Spectra. *Analytical Chemistry*. 1988;60(18):1882-1886.

53. Maxwell DJ, Taylor JR, Nie SM. Self-assembled nanoparticle probes for recognition and detection of biomolecules. *Journal of the American Chemical Society*. 2002;124(32):9606-9612.

54. Franzen S, Folmer JCW, Glomm WR, O'Neal R. Optical properties of dye molecules adsorbed on single gold and silver nanoparticles. *Journal of Physical Chemistry A*. 2002;106(28):6533-6540.

55. Jiang JD, Burstein E, Kobayashi H. Resonant Raman Scattering by Crystal-Violet Molecules Adsorbed on a Smooth Gold Surface: Evidence for a Charge-Transfer Excitation. *Physical Review Letters*. 1986;57(14):1793.

56. Becker CFW, Marsac Y, Hazarika P, et al. Functional immobilization of the small GTPase Rab6A on DNA-gold nanoparticles by using a site-specifically attached poly(ethylene glycol) linker and thiol place-exchange reaction. *Chembiochem*. 2007;8(1):32-36.

57. Baeuerle PA, Gires O. EpCAM (CD326) finding its role in cancer. *British Journal of Cancer*. 2007;96(3):417-423.

58. Prang N, Preithner S, Brischwein K, et al. Cellular and complement-dependent cytotoxicity of Ep-CAM-specific monoclonal antibody MT201 against breast cancer cell lines. *British Journal of Cancer*. 2005;92(2):342-349.

59. Munz M, Kieu C, Mack B, et al. The carcinoma-associated antigen EpCAM upregulates c-myc and induces cell proliferation. *Oncogene*. 2004;23(34):5748-5758.

60. Clark P, Tugwell P, Bennet K, et al. Injectable gold for rheumatoid arthritis. *Cochrane Database of Systematic Reviews*. 2000;(2):CD000520.

61. Hardman R. A toxicologic review of quantum dots: Toxicity depends on physicochemical and environmental factors. *Environmental Health Perspectives*. 2006;114(2):165-172.

62. Derfus AM, Chan WCW, Bhatia SN. Probing the cytotoxicity of semiconductor quantum dots. *Nano Letters*. 2004;4(1):11-18.

63. Ellen E. Connor JMAGCJMMDW. Gold Nanoparticles Are Taken Up by Human Cells but Do Not Cause Acute Cytotoxicity. *Small*. 2005;1(3):325-327.

64. Shukla R, Bansal V, Chaudhary M, et al. Biocompatibility of gold nanoparticles and their endocytotic fate inside the cellular compartment: A microscopic overview. *Langmuir*. 2005;21(23):10644-10654.

65. Hainfeld JF, Slatkin DN, Focella TM, Smilowitz HM. Gold nanoparticles: a new X-ray contrast agent. *British Journal of Radiology*. 2006;79(939):248-253.

66. Hainfeld JF, Slatkin DN, Smilowitz HM. The use of gold nanoparticles to enhance radiotherapy in mice. *Physics in Medicine and Biology*. 2004;49(18):N309-N315.

67. Pelham RW, Nix LC, Chavira RE, Cleveland MV, Stetson P. Clinical trial: single- and multiple-dose pharmacokinetics of polyethylene glycol (PEG-3350) in healthy young and elderly subjects. *Alimentary Pharmacology & Therapeutics*. 2008;28(2):256-265.

68. Culp SJ, Blankenship LR, Kusewitt DF, et al. Toxicity and metabolism of malachite green and leucomalachite green during short-term feeding to Fischer 344 rats and B6C3F1 mice. *Chemico-Biological Interactions*. 1999;122(3):153-170.

69. Koopman G, Reutelingsperger CPM, Kuijten GAM, et al. Annexin-V for Flow Cytometric Detection of Phosphatidylserine Expression on B-Cells Undergoing Apoptosis. *Blood*. 1994;84(5):1415-1420.

CHAPTER 4

OPTIMIZING PRENTS FOR NEAR-INFRARED EXCITATION AND DETECTION

4.1 Introduction

The development of optical tags that are efficiently excited with near-infrared (NIR, 750-950 nm wavelength) light is expected to motivate advances in a variety of biological applications. Two particularly important and challenging areas of interest are *in vivo* optical imaging and spectroscopic detection of disease markers in living organisms and *ex vivo* diagnostic assays on formalin-fixed paraffin-embedded tissue biopsies.

In vivo molecular imaging has attracted tremendous attention because it provides a dynamic view of biological processes under strictly physiologic conditions[1,2] and; in the future, the techniques developed may be used for endoscopic or intraoperative "optical biopsy" of human patients.[3-7] The signal-to-noise ratio (SNR) for optical imaging in living animals depends on the brightness of the optical tags bound to biomarker targets as well as endogenous light absorption, scattering, and autofluorescence within the animal tissue. Absorption and scattering control the degree of exciting photon penetration into the living tissue and whether the excitation light can interact with biomarker-bound optical tags. Autofluorescence in the same spectral region as the tag's spectral output often requires mathematical unmixing[8,9] and can completely overwhelm tag signal in severe cases. In living, non-pigmented animal tissues, the major photon absorbers are

water, oxyhemoglobin, and deoxyhemoglobin, and absorption of light reaches a minimum in the 750-950 nm region, commonly termed the NIR "spectral window".[10,11] Elastic scattering of many living tissues is lower in the NIR wavelength regime than at other wavelengths efficient for silicon-based CCD detection.[12] Moreover, excitation at longer wavelengths minimizes the risk of laser-induced sample damage of delicate biological substrates such as cells, tissues, and living organisms.[13]

When tissue is excised from the body and cut into thin sections for detailed histologic and molecular analysis, the penetration depth of light is no longer a major concern. However, endogenous absorption, fluorescence, and scattering remain and the background is worsened by the extensive formalin fixation necessary for long-term preservation of tissue morphology. Even with red excitation light (647 nm), a significant level of autofluorescence is present.[14] Fortunately, the signal-to-noise ratio of optical assays in FFPE tissues is markedly ameliorated by the use of near-infrared excitation.[15] In general the fraction of the biological substrate that can generate fluorescence decreases with increasing excitation wavelength.

Despite tremendous interest in the development of optical tags with NIR excitation and emission, few materials with these characteristics are available. It is extremely challenging to precisely tune the spectral properties of conventional organic dye fluorophores without adversely affecting stability, quantum yield, and water solubility.[16,17] Like their visible counterparts, NIR organic dyes are also highly susceptible to photobleaching and often have overlapping excitation and emission bands.

A growing number of reports are building the case that quantum dots (QDs), bright, photostable inorganic nanostructures with built-in spectral tuning mechanisms, have great potential as targeted NIR optical contrast agents.[18-20]

In Chapter 3 we developed polymer-protected Raman-encoded nanoparticle tags (PRENTs) and showed that this novel technology has bright spectral signatures with greater resistance to harsh chemical conditions and prolonged illumination than QDs. The PRENT design is simple and modular with a large capacity for spectral diversity. PRENTs are non-toxic to cells, readily amenable to bioconjugation, and selective agents in immunocytochemistry. The Raman spectra of PRENTs comprise multiple bands with bandwidths of 1 – 2 nm that are sharper than QD fluorescence peaks (~30 nm bandwidth) and easier to separate from background elastic scattering and fluorescence.[21] Although the mechanism of Raman scattering differs from fluorescence, both techniques involve excitation of a sample with light and the collection of lower energy light emitted from the sample. Thus, single tags can be imaged with the same instrumentation used for fluorescence imaging. Discrimination of multiple tags could be achieved through either optical or mathematical filtering.[22,23] If the optimal excitation profile and spectral output of PRENTs could be shifted to the NIR spectral region, PRENTs would be well-poised to address the challenges inherent to IHC of FFPE specimens and molecular imaging of living organisms.

Here, we report the development of PRENTs with improved excitation and Raman scattering in the near-infrared spectral region. The overall *hypothesis* guiding this study

is that the incorporation of NIR chromophores as Raman reporters and the size dependent Raman enhancement of single gold nanoparticles (AuNPs) could be used to efficiently develop and optimize a set of PRENTs for excitation at a particular NIR wavelength.

4.2 Results and Discussion

Effect of reporter electronic excitation

In contrast to fluorescent tags such as organic dyes and QDs, changing the absolute energy of the exciting light used for Raman tagged assays does not alter the energy difference between the exciting light and Raman scattered light. In other words, the magnitude of Raman shifts in PRENT spectral signatures is independent of the excitation wavelength used. For biological samples that possess a strong autofluorescence background, signal-to-noise ratios can be readily improved by choosing a Raman excitation wavelength that does not excite the autofluorescence or that only induces autofluorescence in regions outside the Raman spectral region. Excitation in the NIR spectral region minimizes autofluorescence as well as the risk of laser-induced sample damage of delicate biological substrates such as cells, tissues, and living organisms. However, the Raman scattering intensities of breast cancer cells tagged with MG-encoded A-PRENTs were 200-300 times lower at 785 nm excitation than at 633 nm

excitation. Measurements at each wavelength were normalized to a cyclohexane standard to control for the effects of different instrumentation and for the wavelength dependent efficiency of scattered light (λ^{-4}).[24]

Molecular resonance is one likely factor in the intensity differences. This notion is sensible because the excitation laser wavelength of 633 nm is near coincident with an electronic transition in the MGITC reporter molecule (~629 nm), whereas there is no electronic transition near 785 nm (**Figure 4.1**). The differences in relative peak intensities observed between the spectrum taken at 633 nm and the spectrum taken at 785 nm are attributed to the fact that only the vibrations involving atoms responsible for light absorption are enhanced and those in other parts of the reporter are left unenhanced. When excited with 633 nm light, the brightest PRENTs were those encoded with MG/MGITC, CV670, and NB690 reporters that had absorption maxima of 629 nm, 600 nm, and 628 nm, respectively.

Based on these observations, we reasoned that encoding PRENTs with reporters possessing electronic transitions close to 785 nm would be a straightforward means of

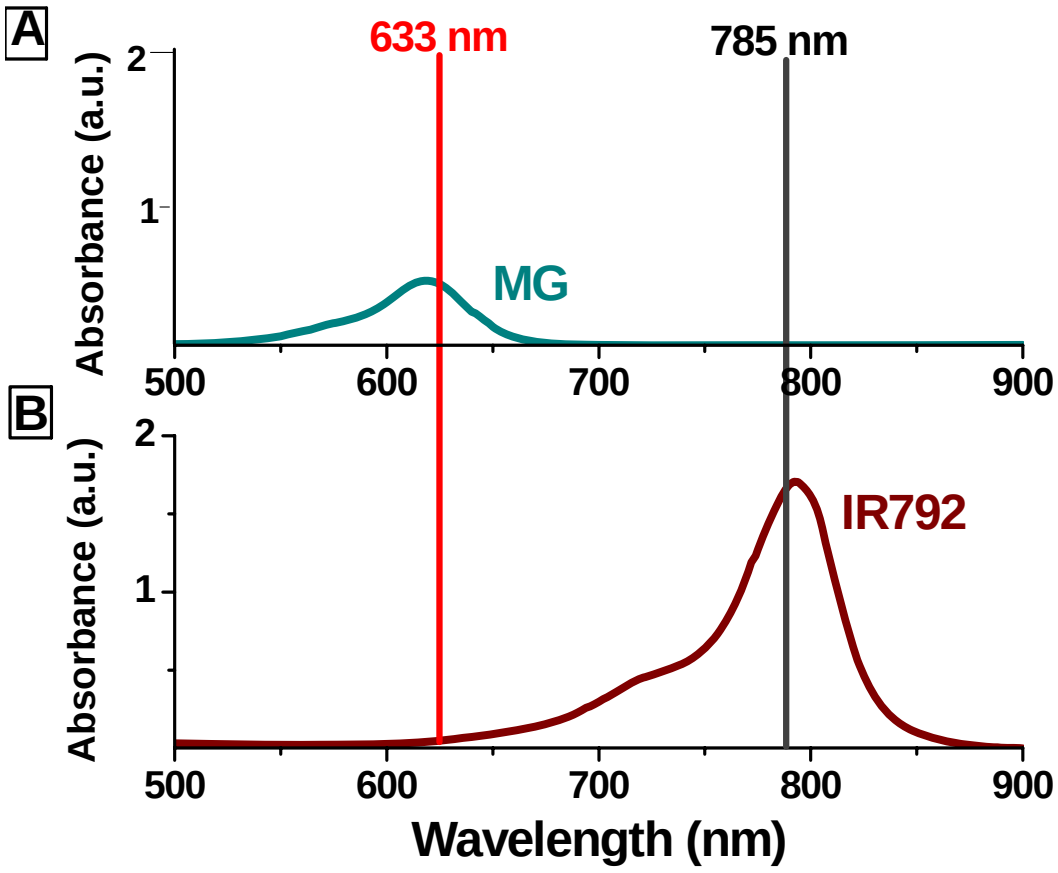

Figure 4.1: Optical absorption spectra of the Raman reporters malachite green (**A**) and IR792 (**B**) with positions of 633 nm HeNe laser line (**red**) and 785 nm diode laser line (**black**) indicated.

improving signal intensity in the near infrared spectral region. None of the reporters described above or in Chapter 3 possess this characteristic and reports of NIR SERS systems usually tailor surface plasmon resonance rather than molecular resonance for Raman enhancement.[25-28] Raman reporter selection is non-trivial because the reporter must bind stably enough to AuNPs for efficient electromagnetic field enhancement, charge transfer effects and PEG-SH stabilization. Conjugating Raman reporters to proteins prior to nanoparticle adsorption allows a greater number of molecules to be encoded in SERS tags but Raman signals require post-assay metal salt deposition to quench interfering fluorescence signals and clearly demonstrate specific Raman signals.[29] Systematic examination of commercially available near-infrared laser dyes suggested that IR792, an organic chromophore with an absorption band close to 785 nm and containing delocalized pi electrons, positive charge, thioether functional group, and ethylamino functional groups, would serve as a good candidate for a NIR Raman reporter. PRENTs were successfully encoded with IR792 by mixing AuNPs with IR792 and allowing the two species to equilibrate for 1 hour before PEGylation. Raman signal intensity did not change appreciably for solutions incubated at longer time points. Of the visible PRENT reporters, only MG/MGITC equilibrated as quickly as IR792, and some reporters required overnight incubation to prevent displacement by subsequent PEG-SH grafting.

To quantify the molecular resonance effect, the brightness and specific peak intensities of IR792-encoded PRENTs were compared to those of MG-encoded PRENTs. MG-encoded PRENTs contained 14,000 reporters per AuNP. Addition of 14,000 IR792

molecules per AuNP caused rapid aggregation of the colloidal system, but reducing the reporter-to-nanoparticle ratio (RNR) to 10,000 provided bright, stable signals without changing the aggregation state. Each PRENT was purified by several rounds of centrifugation to remove fluorescent or Raman scattering impurities, diluted to 4.2 pM concentration, and excited with 633 and 785 nm laser light. Signals were collected under identical sample geometry, laser power, and integration time. PRENT brightness was calculated as the integrated area under the spectrum spanning from 200 –to 2000 cm^{-1} and serves as a measure of overall optical contrast that would be detected by eye or charge coupled device (CCD) in a simple imaging experiment. When excited with 785 nm light, the IR-792-encoded PRENT was 54 times brighter than the MG-encoded PRENT (**Figure 4.2A**). To determine the effect of using a resonant reporter for quantitative spectroscopic detection experiments, the baseline-subtracted areas and heights of peaks with similar bandwidths and Raman shift were compared. At a given concentration, the IR792-PRENT centered at 1379 cm^{-1} was 57 times as intense as the MG-PRENT centered at 1398 cm^{-1} when measured by baseline-subtracted integrated peak area and 54 times as intense when measured by baseline-subtracted peak height (**Figure 4.2B**). The bandwidths of the IR792-PRENT peak and the MG-PRENT peak were 131.98 and 109.05 cm^{-1}, respectively. Interestingly, the brightness of IR792-PRENTs was only 20% lower than the brightness of MG-PRENTs when the tags were excited with 633 nm light (**Figure 4.2C**). This property stems from the fact that the electronic absorption profiles of both Raman reporters are skewed towards shorter wavelengths and there is still a pre-resonance effect at 633 nm for IR792 (**Figure 4.1**). Since most chromophores share this "blue skew" property in their absorption spectra,[30,31] these results suggest that PRENTs

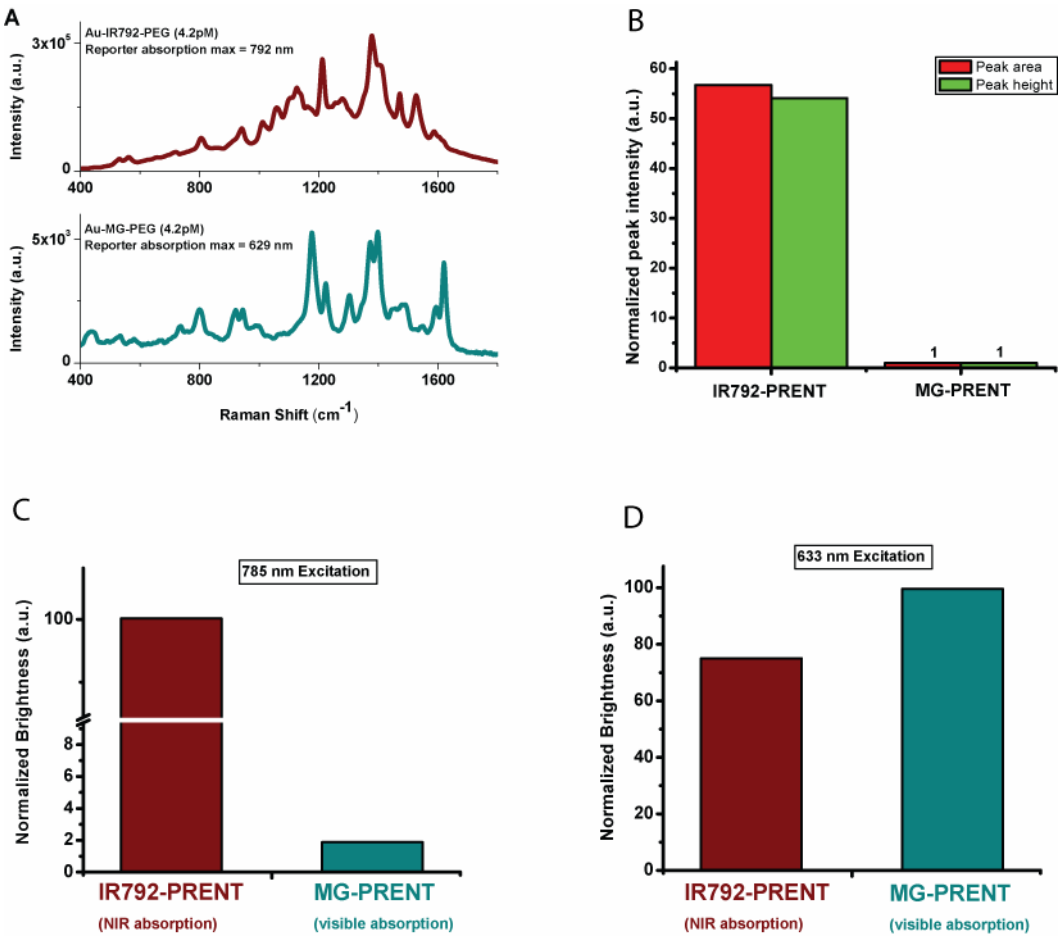

Figure 4.2: Effect of molecular resonance on brightness and peak intensity of PRENTs. (**A**) Raw spectra of 4.2 pM solutions of purified IR792-encoded PRENTs and malachite green (MG) encoded PRENTs. (**B**) Peak areas (red) and peak heights (green) of the 1379 cm^{-1} peak of IR792-encoded PRENTs and the 1398 cm^{-1} peak of MG-encoded PRENTs. Peak area was calculated by integrating the spectral region between the two minima to the left and the right of the peak. Peak height was calculated by subtracting the maximal value of a peak by the mean of its two neighboring minima. Data were normalized so that the MG values would equal one. (**C**) The total brightness (integrated spectral area) of IR792-encoded PRENTs (dark red) and MG-encoded PRENTs (cyan) at 785 nm excitation. (**D**) The total brightness (integrated spectral area) of IR792-encoded PRENTs (dark red) and MG-encoded PRENTs (cyan) at 633 nm excitation.

encoded with reporters possessing a strong electronic transition in the near-infrared spectral region could be efficiently detected and localized with widely available visible light instrumentation as well as more specialized near-infrared instruments.

Generation of diverse NIR spectral signatures

Additional organic chromophores with absorbance bands near 785 nm and functional groups capable of binding to AuNPs were tested as NIR Raman reporters. The primary aim of the reporter testing described in Chapter 3 was to ascertain the effects of subtle changes in reporter structure on the resulting PRENT spectral signature and to determine if non-organosulfur molecules could be incorporated as Raman reporters. Here, the emphasis has shifted to generating NIR spectral signatures that are as distinct as possible with a goal of broad applicability to multiplexed bioassays *in vitro*, *ex vivo*, and *in vivo*. Developing a panel of PRENTs efficiently excited at a single wavelength increases the probability of success in developing tagging assays as well as demonstrating the potential for multiplexing and combinatorial coding. **Figure 4.3** shows Raman reporter chemical structures and corresponding NIR PRENT spectral signatures for the Raman reporters HITC, IR140, IR143, IR786, IR792, and IR800. All six NIR-PRENTs produced strong Raman signals at 785 nm with no changes in spectral signature or aggregation state for several months when stored in phosphate buffered saline. Three of the six Raman

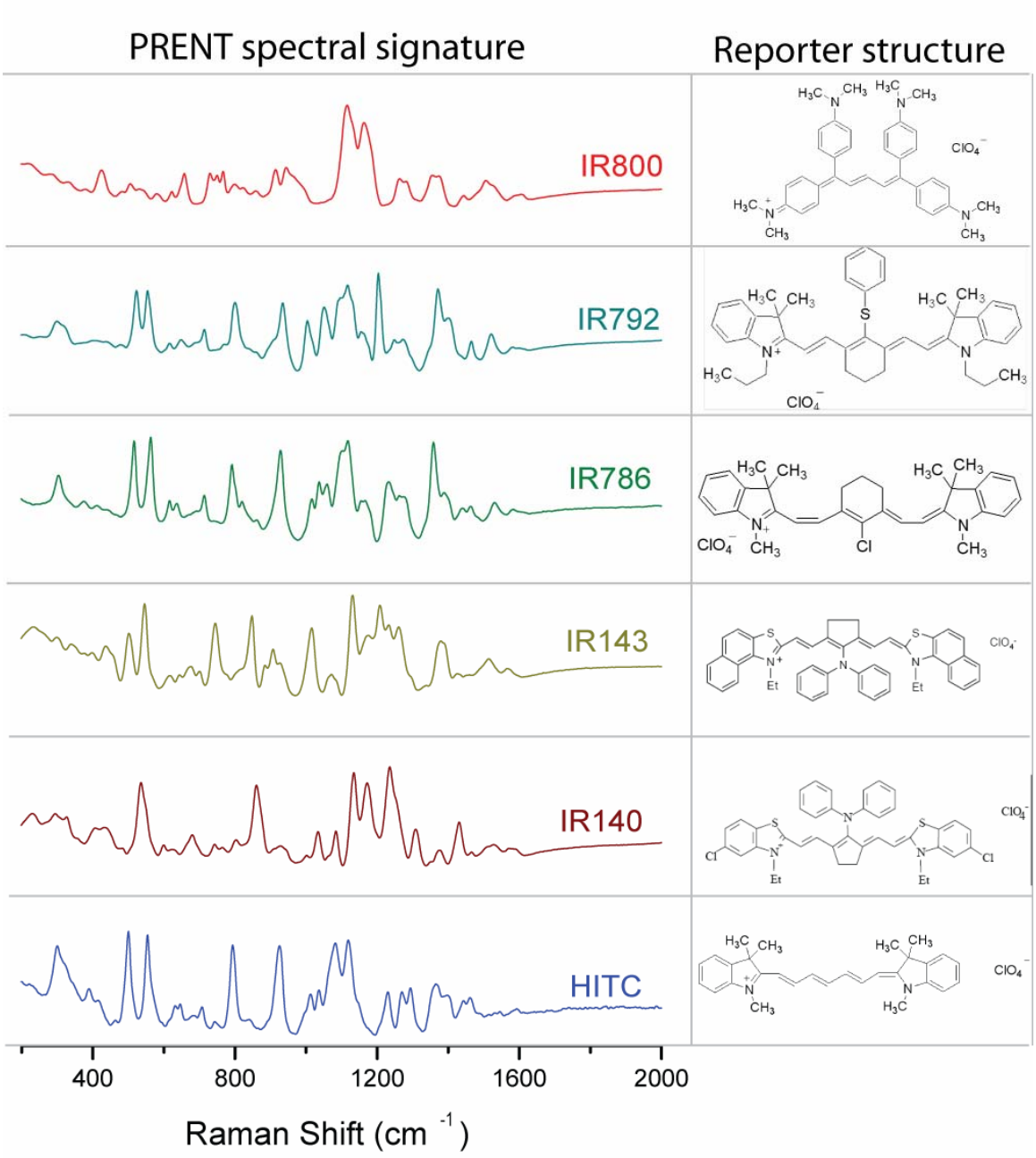

Figure 4.3: Near-infrared PRENTs. Raman spectra of NIR-PRENTs (**left**) and chemical structures of their embedded reporters (**right).**

reporters, IR792, IR143, and IR140, contain organosulfur groups. All six Raman reporters possess extensively delocalized pi electrons and positive charges. A summary of NIR-PRENT characteristics is provided in **Table 4.1**.

Effect of reporter-to-nanoparticle ratio

An interesting finding is the differential effect of the number of Raman reporter molecules added to each AuNP (reporter-to-nanoparticle ratio, RNR) on PRENT peak intensity and the extent of AuNP aggregation. The RNR provides a simple mechanism for attenuating PRENT intensity without causing excessive aggregation. PRENT intensity gradually increased with increasing ratio of reporter molecules to AuNPs (RNR) over much of the range of RNR tested. In the case of IR792 reporter titration on 60 nm AuNPs, the intensity of the Raman band centered at 1204 cm^{-1} increased monotonically for $0 \leq RNR \leq 12{,}000$ (**Figure 4.4A**). For RNR >12,000, the colloidal system became unstable within a few minutes and the Raman intensity values began to decrease.

Table 4.1: Characteristics of NIR reporters and corresponding encoded PRENTs

Reporter	Absorption maximum (nm)	Optimal RNR for 60 nm AuNPs	Spectral changes upon PEGylation	Spectral changes in 10X PBS	> 90% intensity after 48h
IR792	792	10,000	None	None	Yes
IR800	800	17,500	None	None	Yes
HITC	740	12,500	None	None	Yes
IR143	823	2,500	None	None	Yes
IR786	775	10,000	None	None	Yes
IR140	839	10,000	None	None	Yes

Vortexing the AuNP-reporter solution immediately before measurement slightly increased the intensity but results were not very reproducible. Reproducibility between experiments required that IR792 be either freshly dissolved or scrupulously stored under conditions minimizing exposure to light, temperature, and moisture. Otherwise the curve shifted to the right due to reporter degradation. However the same trends were always observed.

Au-IR792 complexes were also studied with absorption spectroscopy, a sensitive indicator of metal NP aggregation state well-suited for accurate and reproducible analysis of a large number of samples.[32] A strong plasmon resonance absorption band at 534 nm was observed in the absence of IR792. Increasing RNR decreased the 534 nm band and caused a broadband increase at wavelengths greater than 650 nm (**Figure 4.4B**). The spectral changes were not reversed by PEGylation or prolonged incubation. The plasmon resonance frequencies of AuNPs coated with an adsorbate are strongly dependent on size, shape, interparticle distance (aggregation state for a colloidal solution), adsorbate charge transfer, and adsorbate and solvent dielectric constant.[33-38] Since particle size, shape, adsorbate type, and solvent were held constant in this experiment, the spectral changes can be due only to changes in nanoparticle aggregation or the degree of electron transfer between gold and adsorbed IR792. Several observations suggest that the spectral changes are due to aggregation: (i) the longer wavelength absorption band does not have a well-defined absorption maximum, as was observed by Nickel, et al in a study of silver nanoparticle-triphenylmethane dye complexes,[39] (ii) the shape of the longer wavelength

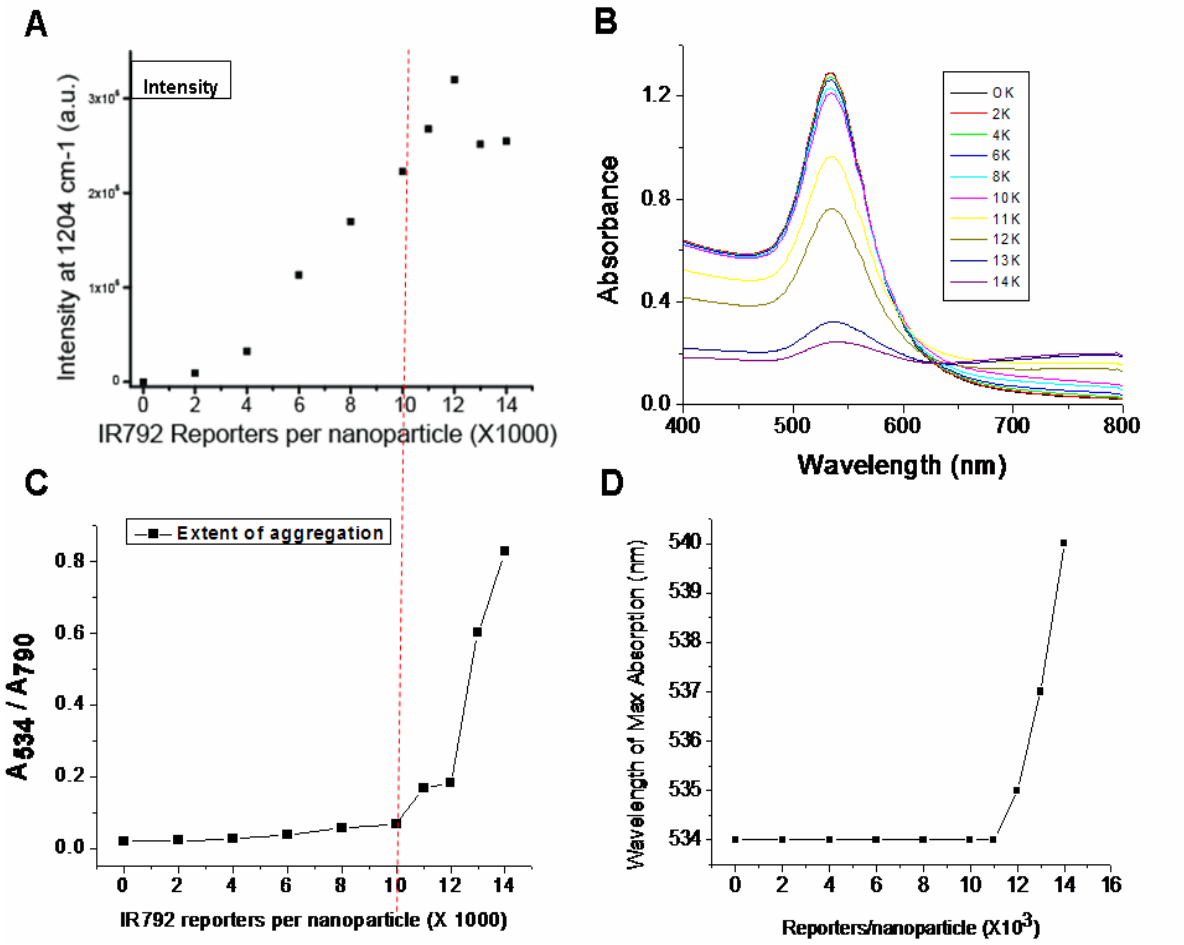

Figure 4.4. Titration of IR792 reporter dye on 60 nm AuNPs. (**A**) Integrated Raman peak intensity at 1204 cm^{-1} as a function of IR792 reporter to nanoparticle ratio (RNR). (**B**) Optical absorption spectra of the AuNP-IR792 solutions in A. OK – 14K is the reporter to nanoparticle ratio in thousands. (**C**) The ratio of absorbance at 790 nm to the absorbance at 534 nm as a function of reporter to nanoparticle ratio. (**D**) The wavelength of maximum absorption (lamba max) as a function of reporter to nanoparticle ratio. The red dashed line superimposed on **A** and **C** indicates the optimal RNR for IR792-PRENTs which maximized the ratio of Raman intensity and the aggregation extent.

band is nearly identical to the shape of the band that appears when AuNPs are intentionally aggregated with concentrated phosphate buffered saline, (iii) IR792 is cationic and can reduce the negative surface charge of AuNPs upon adsorption, (iv) large shifts in the ratio of the absorbance at 790 nm to the absorption at 534 nm (**Figure 4.4C**) coincided with dramatic solution color changes from pink to mauve to grey, and (v) an abrupt bathochromic shift in the position of the plasmon absorption band from 534 nm to 540 nm (**Figure 4.4D**) suggested cluster formation.[40]

Effect of nanoparticle diameter

Besides resonance enhancement in the reporter, additional factors in the wavelength dependent Raman intensity of PRENTs may include the geometry of the core AuNP. The PRENTs used in this study thus far have comprised single AuNPs with a mean diameter of ~60 nm, based on previous research delineating highly enhancing particles at 633-647 nm excitation wavelength.[41] Since unaggregated metal NPs show relatively narrow excitation profiles[42] and the optimal size for Raman enhancement from AuNPs at 785 nm has not been previously reported, we sought to determine the effect of AuNP diameter used for NIR-PRENT preparation at the new wavelength.

AuNPs with mean diameter of approximately 40, 50, 60, 80, 100, and 150 nm were tested as Raman enhancers for IR792 scattering. An IR792 footprint, the area on the AuNP surface occupied by each IR792 molecule, was estimated as 1.13 nm^2 based on the 60 nm results in **Figure 4.4** and used as a starting point for focused titration of IR792 RNR at other sizes. The optimal IR792 RNR was defined as the highest ratio of IR792 reporters to AuNPs that did not cause a solution color change after 1 h incubation. **Figure 4.5A** plots the peak intensity per nanoparticle for 1204 cm^{-1} band at each tested NP size at 785 nm excitation. The highest levels of enhancement were provided by 100 nm sized AuNPs, which yielded an intensity value ~3 times greater than the intensity provided by 60 nm AuNPs. Since tagging of proteins immobilized on two-dimensional surfaces (e.g. protein microarray, cell membrane, tissue section) will likely be the first practical applications of NIR PRENTs, steric considerations will play a role in the observed staining intensity. Intensity data was also normalized to the maximum cross-sectional area of the NP used. 80 nm AuNPs yielded a normalized intensity ~30% higher than 100 nm AuNPs and ~35% higher than 60 nm AuNPs (**Figure 4.5B**). To verify quantitatively that results were not biased by different levels of aggregation state, an aggregation index (AI) was constructed for each PRENT tested (**Figure 4.5C**). Unprotected AuNPs mixed with 10X concentrated PBS (Au + 10X PBS) served as a positive control for 100% extent of aggregation. AuNPs protected by PEG-SH but lacking reporters (Au-PEG) served as a negative control for the presence of aggregates. Based on the considerations described in the "Effect of reporter-to-nanoparticle ratio" section above, the AI was defined as:

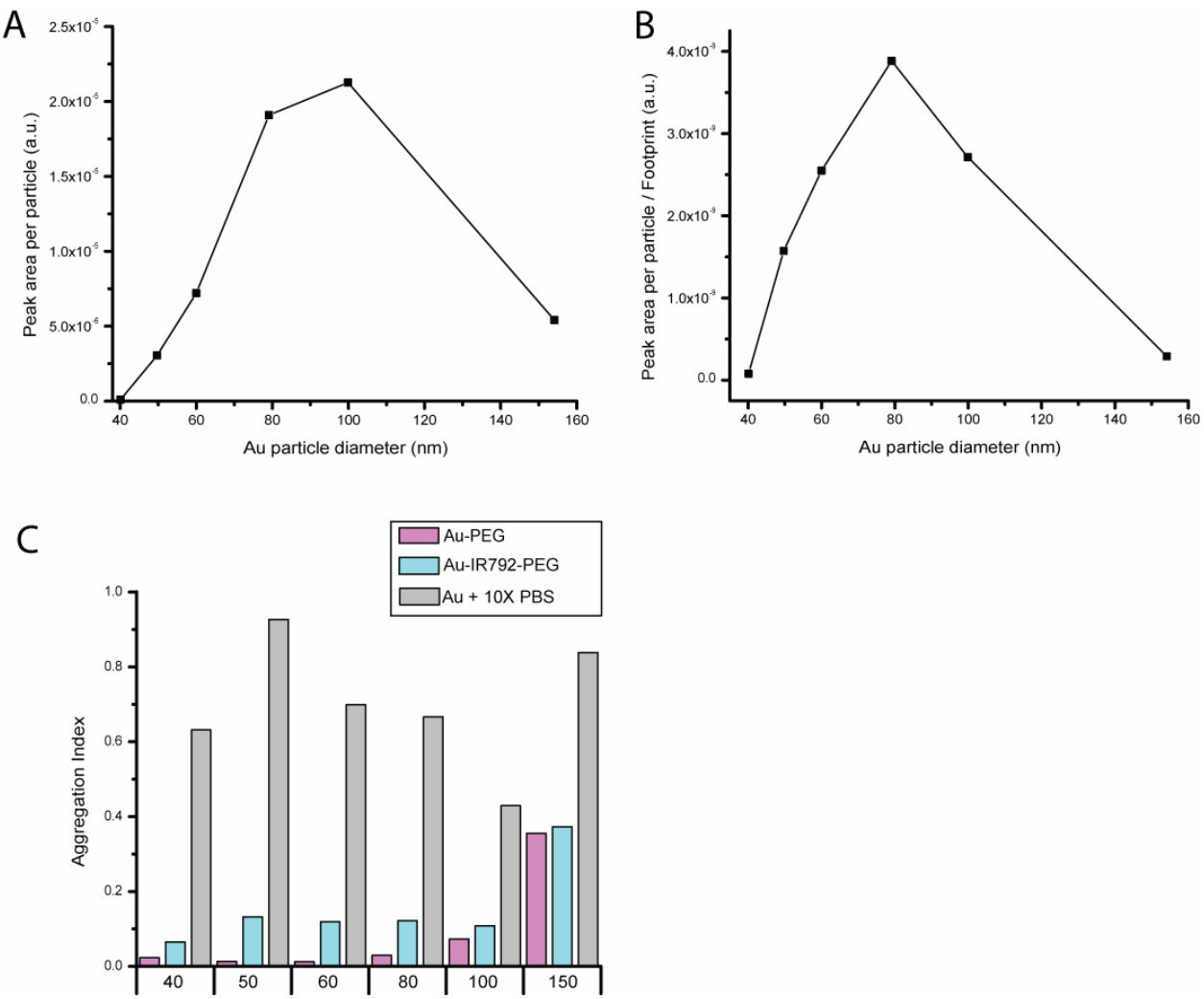

Figure 4.5. **Size-dependent Raman enhancement of gold nanoparticles at 785 nm excitation wavelength.** (**A**) Integrated Raman intensity of the 1204 cm^{-1} peak of IR792 encoded PRENTs as a function of core nanoparticle size. (**B**) Data in (A) normalized to the estimated footprint of the nanoparticle on a flat surface. (**C**) Aggregation index for the IR792 encoded PRENTs in comparision with PEGylated single Au particles and intentionally aggregated Au particles in phosphate buffered saline for each nanoparticle size tested (see text for details).

AI = Absorbance of the sample at the maximum absorbance of the long wavelength band in (Au + 10 X PBS) / Absorbance of the sample at the absorbance maximum of Au-PEG

The aggregation extent was not dramatically different among tested preparations and was relatively low. The IR792 reporter coverage on each of the differently sized nanoparticles did not vary considerably, as indicated by the IR792 footprints calculated in **Table 2**. This finding suggests a consistent surface chemistry among the different sized AuNPs. As expected, this IR792 footprint value is slightly larger than AuNP footprint values obtained for fluorescein isothiocyanate.[43]

Correlation of AuNP size with optical enhancement simplifies rational and reproducible design of PRENTs. Larger or smaller AuNPs can be chosen based on the unique requirements of a particular experiment. 80 nm AuNPs were used for immunosorbent assay experiments (Chapter 5) but 50 nm AuNPs were used for suspension immunoassays of cell and microsphere substrates. Suspension assays required removal of unbound PRENTs via centrifugation. A small proportion of PRENTs sedimented under the slowest speed capable of pelleting the substrate and had to be removed prior to immunolabeling procedures. Although the enhancement factor of 50 nm AuNPs was

Table 4.2: Characteristics of nanoparticles and reporter-nanoparticle relationships of PRENTS used in Fig. 4.5.

Particle diameter (nm)	Optimal IR792: Nanoparticle Ratio	IR792 footprint (nm^2)
40.1	4000	1.26
49.7	5600	1.39
59.9	10000	1.13
79.1	22000	0.89
99.9	37000	0.85
154.1	80000	0.93

lower than for 60-100 nm AuNPs, the intensity of 50 nm PRENT solution was slightly higher after the pre-immunolabeling spin due to its lower sedimentation velocity. Note that the size-dependent effects of these AuNPs are not as dramatic as those observed in microscopic studies of individual NPs because the present study uses bulk colloidal solutions, with each population containing a finite distribution of NP sizes. Nanoparticle population studies are most relevant for practical analytical applications. We may see a greater size-dependent Raman enhancement effect with more monodisperse particle preparations.

4.3 Conclusions

The results of this study clearly demonstrate that core nanoparticle geometry and molecular resonance can be used to improve the overall brightness and Raman peak intensities of PRENTs. In addition, the ratio of reporters to nanoparticles (RNR) in the PRENT preparation procedure provides a fine adjustment of intensity over a wide range without causing a large change in the nanoparticle aggregation state. This property should allow for reproducible and homogeneous PRENT preparation in comparison to optical tags that deliberately aggregate nanoparticles to increase overall signal intensity but introduce significant tag heterogeneity. The insights generated from this study allow one to customize PRENT properties for a given tagging applications. A set of NIR-

PRENTs with distinct Raman spectral signatures was developed using NIR chromophores and 80 nm AuNPs for further work in slide-based immunoassays. A similar set of NIR-PRENTs was prepared using 50 nm AuNPs for bead-based immunoassays.

4.4 Materials and Methods

Materials

Ultrapure water (18 MΩ cm^{-1}) was used to prepare all aqueous solutions. The following materials were used without further purification: 40.1, 49.7, 59.9, 79.1, 99.9, and 154.1 nm diameter gold particles (British Biocell International); IR140 and IR143 (Exciton), mPEG-SH (MW ~ 5,000 Da, Nektar Therapeutics). All other reagents were obtained from Sigma-Aldrich at the highest purity available.

All experiments were performed at room temperature unless otherwise specified.

Measurements and data analysis

Optical absorption spectra were recorded on a Shimadzu UV-2401 spectrometer. Disposable polyacryl cuvettes with 1cm optical path length were used in all UV-Vis measurements. Raman scattering spectra were recorded with an ExamineR Raman microscope (DeltaNu) equipped with a 785 nm diode laser. Spectra were processed and analyzed in Origin software (Origin Lab Corp.). Note that the spectra consist of sharp

Raman spectral bands (1-2 nm FWHM) and a concomitant broad underlying continuum noted by other SERS workers.[44] In most cases the continuum was removed mathematically and did not affect the results or conclusions in this work. Raman bands were separated from SERS continuum and sample background fluorescence using a Fourier transform method (Examine R software, Delta Nu) or by manual construction of baselines in Grams A/I software (Thermo Scientific). Peak area was calculated by integrating the spectral region between the closest local minimum to the left and the closest local minimum to the right of the peak. Integration was performed by the trapezoidal method. Peak height was calculated by subtracting the maximal value of a peak by the mean of its two neighboring minima. Calibration curves were constructed and fit in Origin software (Origin Lab Corp)

Polymer-protected Raman encoded nanoparticle tags (PRENTs)

Freshly prepared reporter solution was slowly added under rapid mixing with AuNPs to cover the NP surface and allow even distribution. The AuNP-reporter complexes were equilibrated in low-light conditions from 15 minutes to 24 hours, depending on reporter affinity for AuNP. The ratio of reporter molecules to Au particle was adjusted for each reporter to minimize aggregation. The volume ratio of stock reporter solution and gold nanoparticle solution was controlled to be 1:6. PEG-SH (10 μM) was added dropwise to the Au-reporter complex solution to achieve a final ratio of 300,000 PEG-SH per Au particle. Storage of PEG-SH under ambient conditions did not affect the results.

4.5. References

1. Massoud T, Gambhir S. Molecular imaging in living subjects: seeing fundamental biological processes in a new light. *Genes & Development*. 2003;17(5):545-580.

2. Weissleder R. Scaling down imaging: Molecular mapping of cancer in mice. *Nature Reviews Cancer*. 2002;2(1):11-18.

3. Weissleder R. Molecular imaging in cancer. *Science*. 2006;312(5777):1168-1171.

4. Weissleder R, Pittet MJ. Imaging in the era of molecular oncology. *Nature*. 2008;452(7187):580-589.

5. Rao J, Dragulescu-Andrasi A, Yao H, Yao H. Fluorescence imaging in vivo: recent advances. *Current Opinion in Biotechnology*. 2007;18(1):17-25.

6. Kircher MF, Mahmood U, King RS, Weissleder R, Josephson L. A Multimodal Nanoparticle for Preoperative Magnetic Resonance Imaging and Intraoperative Optical Brain Tumor Delineation. *Cancer Res*. 2003;63(23):8122-8125.

7. Muguruma N, Ito S. Endoscopic molecular imaging: Beacon to the destination. *Digestive Endoscopy*. 2008;20(3):101-106.

8. Gao XH, Cui YY, Levenson RM, Chung LWK, Nie SM. In vivo cancer targeting and imaging with semiconductor quantum dots. *Nature Biotechnology*. 2004;22(8):969-976.

9. Hama Y, Urano Y, Koyama Y, et al. In Vivo Spectral Fluorescence Imaging of Submillimeter Peritoneal Cancer Implants Using a Lectin-Targeted Optical Agent . *Neoplasia.* . 2006;8(7):607–612.

10. Frangioni JV. In vivo near-infrared fluorescence imaging. *Current Opinion in Chemical Biology*. 2003;7(5):626-634.

11. Rolfe P. In vivo near-infrared spectroscopy. *Annual Review of Biomedical Engineering*. 2000;2:715-754.

12. Yong Taik Lim SK, and Frangioni JV. Selection of Quantum Dot Wavelengths for Biomedical Assays and Imaging. *Molecular Imaging*. 2003;2(1):50-64.

13. Puppels GJ, Olminkhof JH, Segers-Nolten GM, et al. Laser irradiation and Raman spectroscopy of single living cells and chromosomes: sample degradation occurs with 514.5 nm but not with 660 nm laser light. *Exp Cell Res*. 1991;195(2):361-7.

14. Doering W. Ph.D. Dissertation. Indiana University. Dept of Chemistry. 2003.

15. diVito KA, Camp RL. Tissue microarrays - automated analysis and future directions. *Breast Cancer Online*. 2005;8(7).

16. Patonay G, Antoine MD. Near-Infrared Fluorogenic Labels - New Approach to an Old Problem. *Analytical Chemistry*. 1991;63(6):A321-A326.

17. Amiot C, Xu S, Liang S, Pan L, Zhao J. Near-infrared fluorescent materials for sensing of biological targets. *Sensors*. 2008;8(5):3082-3105.

18. Cai W, Shin DW, Chen K, et al. Peptide-Labeled Near-Infrared Quantum Dots for Imaging Tumor Vasculature in Living Subjects. *Nano Lett.* 2006;6(4):669-676.

19. Jayagopal A, Russ P, Haselton F. Surface engineering of quantum dots for in vivo vascular Imaging. *Bioconjugate Chemistry*. 2007;18(5):1424-1433.

20. Tada H, Higuchi H, Wanatabe T, Ohuchi N. In vivo real-time tracking of single quantum dots conjugated with monoclonal anti-HER2 antibody in tumors of mice. *Cancer Research*. 2007;67(3):1138-1144.

21. Hanlon EB, Manoharan R, Koo TW, et al. Prospects for in vivo Raman spectroscopy. *Physics in Medicine and Biology*. 2000;45(2):R1-R59.

22. Wabuyele MB, Yan F, Griffin GD, Vo-Dinh T. Hyperspectral surface-enhanced Raman imaging of labeled silver nanoparticles in single cells. *Rev. Sci. Instrum.* 2005;76(6):063710-7.

23. Pelletier MJ. Quantitative analysis using Raman spectrometry. *Applied Spectroscopy*. 2003;57(1):20A-42A.

24. McCreery RL. *Raman Spectroscopy for Chemical Analysis*. New York: Wiley Interscience; 2000.

25. Souza GR, Christianson DR, Staquicini FI, et al. Networks of gold nanoparticles and bacteriophage as biological sensors and cell-targeting agents. *Proceedings of the National Academy of Sciences of the United States of America*. 2006;103(5):1215-1220.

26. Souza GR, Levin CS, Hajitou A, et al. In Vivo Detection of Gold-Imidazole Self-Assembly Complexes: NIR-SERS Signal Reporters. *Anal. Chem.* 2006.

27. Schwartzberg AM, Grant CD, Wolcott A, et al. Unique gold nanoparticle aggregates as a highly active surface-enhanced Raman scattering substrate. *Journal of Physical Chemistry B*. 2004;108(50):19191-19197.

28. Jackson J, Halas N. Surface-enhanced Raman scattering on tunable plasmonic nanoparticle substrates. *Proceedings of the National Academy of Sciences of the United States Of*. 2004;101(52):17930-17935.

29. Ansari DO, Stuart DA, Nie SM. Enhanced Raman spectroscopic detection of protein biomarkers in intact cells and tissues. *Proc. SPIE- Int. Soc. Opt. Eng.* 2005;5699:82-90.

30. Prahl S. http://omlc.ogi.edu/spectra/PhotochemCAD/html/index.html. *Oregon Medical Laser Center*.

31. Shapiro HM. Excitation and Emission Spectra of Common Organic Dyes. In: *Current Protocols in Cytometry*. John Wiley and Sons, Inc; 2003.

32. Freeman RG, Grabar KC, Allison KJ, et al. Self-Assembled Metal Colloid Monolayers - an Approach to Sers Substrates. *Science*. 1995;267(5204):1629-1632.

33. Mulvaney P. Surface Plasmon Spectroscopy of Nanosized Metal Particles. *Langmuir*. 1996;12(3):788-800.

34. Mock J, Barbic M, Smith D, Schultz D, Schultz S. Shape effects in plasmon resonance of individual colloidal silver nanoparticles. *Journal of Chemical Physics*. 2002;116(15):6755-6759.

35. Lazarides AA, Lance Kelly K, Jensen TR, Schatz GC. Optical properties of metal nanoparticles and nanoparticle aggregates important in biosensors. *Journal of Molecular Structure: Theochem*. 2000;529(1-3):59-63.

36. Oldenburg SJ, Averitt RD, Westcott SL, Halas NJ. Nanoengineering of optical resonances. *Chemical Physics Letters*. 1998;288(2-4):243-247.

37. Lee K, El-Sayed M. Gold and Silver Nanoparticles in Sensing and Imaging: Sensitivity of Plasmon Response to Size, Shape, and Metal Composition. *J. Phys. Chem. B*. 2006;110(39):19220-19225.

38. Kelly KL, Coronado E, Zhao LL, Schatz GC. The optical properties of metal nanoparticles: the influence of size, shape, and dielectric environment. *J. Phys. Chem. B*. 2003;107(3):668–677.

39. Nickel U, Halbig P, Gliemann H, Schneider S. Charge transfer like complexes of organic dyes adsorbed at colloidal silver studied by cyclic voltammetry, UV-vis and SERS spectroscopy. *Berichte Der Bunsen-Gesellschaft-Physical Chemistry Chemical Physics*. 1997;101(1):41-49.

40. Sonnichsen C, Reinhard BM, Liphardt J, Alivisatos AP. A molecular ruler based on plasmon coupling of single gold and silver nanoparticles. *Nature Biotechnology*. 2005;23(6):741-745.

41. Krug JT, Wang GD, Emory SR, Nie SM. Efficient Raman enhancement and intermittent light emission observed in single gold nanocrystals. *Journal of the American Chemical Society*. 1999;121(39):9208-9214.

42. Emory SR. Direct Observation of Size-Dependent Optical Enhancement in Single Metal Nanoparticles. *Journal of the American Chemical Society.* 1998;120(31):8009-8010.

43. Makarova OV, Ostafin AE, Miyoshi H, Norris JR, Meisel D. Adsorption and encapsulation of fluorescent probes in nanoparticles. *Journal of Physical Chemistry B.* 1999;103(43):9080-9084.

44. Michaels AM, Nirmal M, Brus LE. Surface enhanced Raman spectroscopy of individual rhodamine 6G molecules on large Ag nanocrystals. *Journal of the American Chemical Society*. 1999;121(43):9932-9939.

CHAPTER 5

QUANTITATIVE ASSAYS WITH BIOCONJUGATED PRENTS

5.1 Introduction

The development of immunoassays capable of ultrasensitive and simultaneous quantification of multiple protein biomarkers is of tremendous interest in molecular diagnostics. Precise determination of biomarker expression allows better prediction of disease states, prognostic outcomes, and therapy selection than qualitative detection. Reducing assay detection limits allows earlier detection of subclinical disease. Many biomarkers with potential predictive value for the onset of cancer and neurodegenerative disorders are present at picomolar levels or lower in the early course of disease, before aberrant processes produce recognizable clinical findings.[1-4] The importance of early detection cannot be overstated. Favorable prognosis is nearly always inversely correlated with disease progression.[5] Recent progress in systems biology research and experience in clinical diagnostic applications have demonstrated the complex nature of protein interactions and the difficulty of gaining insights into biological processes and disease etiology from measurements of a single protein or nucleic acid.[6-10] Thus, there is an increasing demand for technologies that effectively analyze panels of multiple biomarkers. Immunoassay systems that provide multivariate readouts of colocalized

biomolecules reduce the number of repeated measurements and the amount of sample required, important considerations for limited clinical samples.

Immunosorbent assays (ISAs) combine the selectivity of antibody-antigen coupling with the robustness and simplicity of solid-liquid separation of bound and unbound tags. ISAs are typified by the selective or non-selective capture of an unknown quantity of a disease relevant antigen on a surface, followed by labeling of the immobilized antigen with a cognate antibody conjugated to a radioactive, enzymatic, or optical tag. Quantification of the target antigen is provided by readouts from the bound tags, with increasing signal intensity corresponding to increased amounts of antigen in the sample.

The use of surface-enhanced Raman scattering (SERS) for quantitative detection of specific disease-relevant biomolecules is still in its infancy. The current resurgence of interest in analytical applications of SERS arose from recent breakthroughs in the ability to precisely and reproducibly control the geometry and surface chemistry of metal nanostructures and a microscopic understanding of the effects of those manipulations on optical properties.[11-14] Quantitative ISAs using soluble SERS tags have been reported but require a specialized assay support or post-assay signal development, limiting the number of potential biological applications.[15-19] However, Berlin and coworkers recently described the preparation of SERS tags called composite organic inorganic nanoparticles (COINS) and their use in sandwich and direct immunoassays without additional signal development.[20]

Here, we report the development of a Raman-linked immunosorbent assay (RLISA) using polymer-protected Raman encoded nanoparticle tags (PRENTs), comparison of antibody conjugation methods, and demonstration of signal processing methods for PRENT quantification. Our *hypothesis* is that the unique properties of PRENTs such as a robust surface coating and tolerance to prolonged laser excitation will allow quantification of proteins in a miniaturized ISA format. PRENTs tuned for optimal excitation in the near-infrared (NIR) spectral region are advantageous for *in vitro* immunoassays as well as for *ex vivo* detection in biopsied tissue and *in vivo* imaging of living animals. In comparison with visible detection, NIR optical readouts are compatible with a greater variety of immunosorbent assay solid supports.[21,22] In addition, crude lysates or serum samples often used as sources of target antigen in immunoassays contain many endogenous fluorophores. Few of these fluorophores can be excited efficiently with light wavelengths below 200 nm or above 700 nm.[23,24] Ultraviolet (UV) excitation is usually unacceptable because many solid supports can absorb short wavelength photons.[25]

5.2 Results and Discussion

Effect of antibody conjugation method

The successful development of a new ISA requires strongly binding tags and exhaustive systematic testing that can consume large amounts of reagents. Thus, optimization of tag avidity and preparation procedures is prudent. We compared several antibody

conjugation methods to maximize the number of antigen reactive antibodies on the PRENT surface. Multivalency greatly increases nanoparticle avidity for the target antigen because all of the antibody: antigen interactions must be broken simultaneously before the bioconjugated nanoparticle can dissociate. The original procedure we used for functionalizing PRENTs with immunoglobulin G (IgG) class antibodies involved derivatizing amine groups on the antibody molecule with a heterobifunctional PEG containing an N-hydroxysuccinimide ester and a protected thiol prior to incubation with AuNP-reporter complexes (**Figure 5.1 Scheme I**). Although antibodies can be adsorbed directly to AuNPs, we were concerned about low reactivity due to excess PEG-SH displacing surface-bound antibody during the conjugation procedure or bulky PEG chains masking the antigen-binding sites of the coadsorbed antibody.[26] In addition, there is a possibility of denaturation of IgG structure by the AuNP through oxidative addition of disulfide bridges or interaction with hydrophobic residues.[27,28] On the other hand, coupling of unmodified antibodies directly with AuNP-reporter complexes (**Figure 5.1 Scheme II**) is simpler and less time-consuming than coupling via a polymeric intermediate. The PEG derivative used in **Scheme I** is reactive to moisture and requires careful storage and handling under inert gas prior to bioconjugation. Although we kept the degree of derivatization low (~0.7 thiol groups per IgG molecule), amine functional groups are distributed throughout the IgG molecule and the random PEG procedure also carries a risk of inactivating antigen binding capability. In principle,

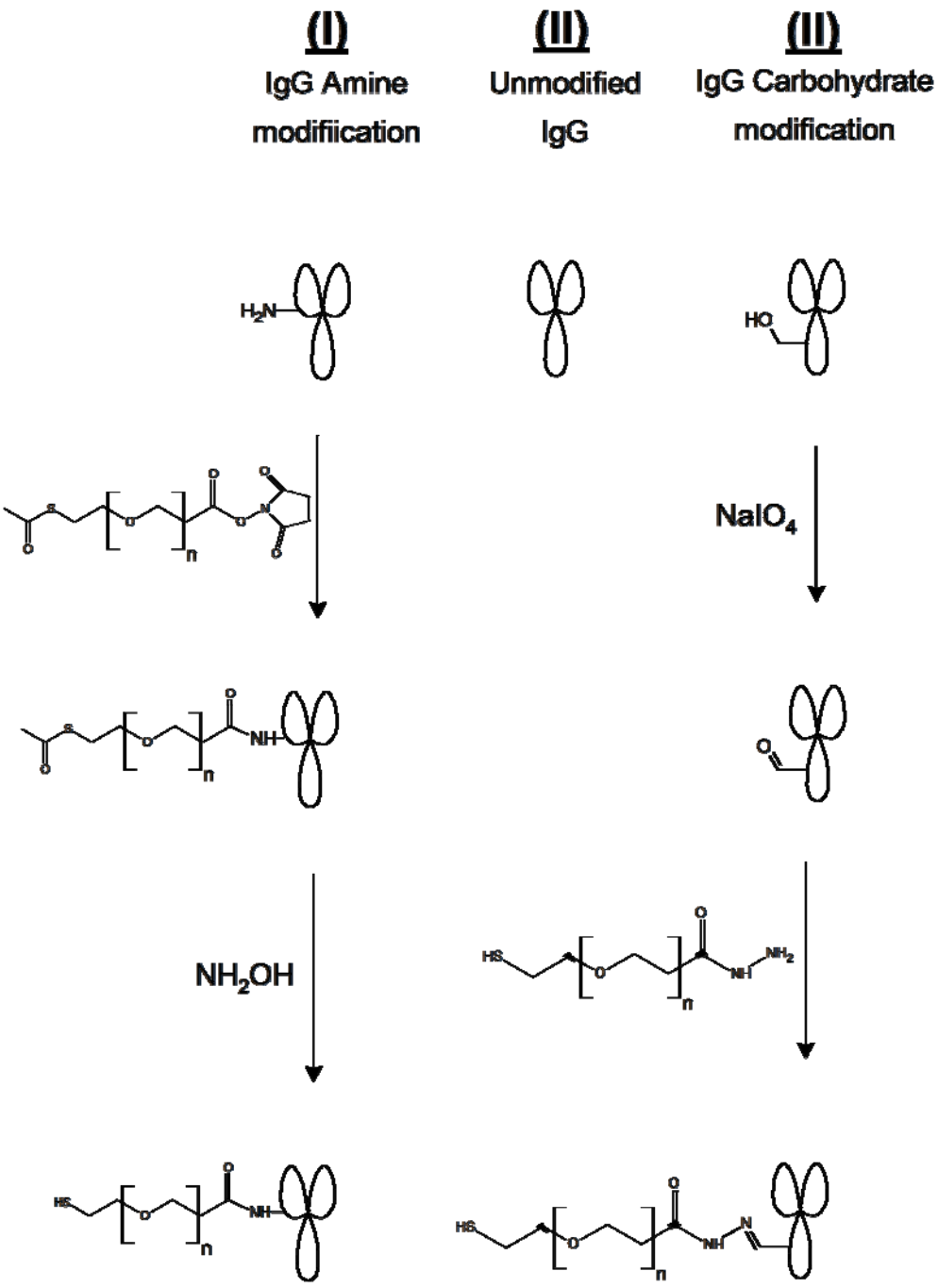

Figure 5.1: Schematic illustration of the modification reactions of antibodies by PEG derivatives through amine groups (I) or oxidized carbohydrate residues (III). Scheme II is the use of antibodies without PEG modification.

the most ideal antibody conjugation procedure is to attach the PEG-SH only to a portion of the IgG molecule that excludes the antigen binding site. A common methodology takes advantage of the restricted localization of glycosylation sites on antibodies. (**Figure 5.1 Scheme III)** Mild oxidation of antibodies with periodate generates aldehyde functional groups in the polysaccharide chains distal to the antigen binding site.[29] These aldehydes are highly reactive toward hydrazide groups, which can be readily introduced into PEG derivatives and are not reactive toward thiols or amines under physiologic conditions.[30] In addition, hydrazides do not disrupt the bond between AuNPs and sulfur atoms.[31] Scheme III is more laborious and complex than Schemes I and II but is designed to ensure correct orientation of antibody on the AuNP surface as well as the presence of a flexible polymeric spacer, while minimizing the risk of antibody inactivation.

Since all three bioconjugation procedures involve some trade-offs, we sought a definitive answer on whether any one of these procedures is superior in practice. We prepared IR792-encoded A-PRENTs using antibodies modified by Schemes I, II, or III (**Figure 5.2)** and compared their antigen-binding performance under identical experimental conditions. (The details of preparation and characterization are provided in the Materials and Methods section). A-PRENTs were functionalized with equivalent amounts of antibody and incubated in suspension with silica microspheres coated with a cognate antigen. After separating unbound A-PRENT from PRENT tagged microspheres, the PRENT tagged microspheres were qualitatively examined by reflected light microsopy and quantitatively evaluated with Raman spectroscopy. Under light microscopy, the

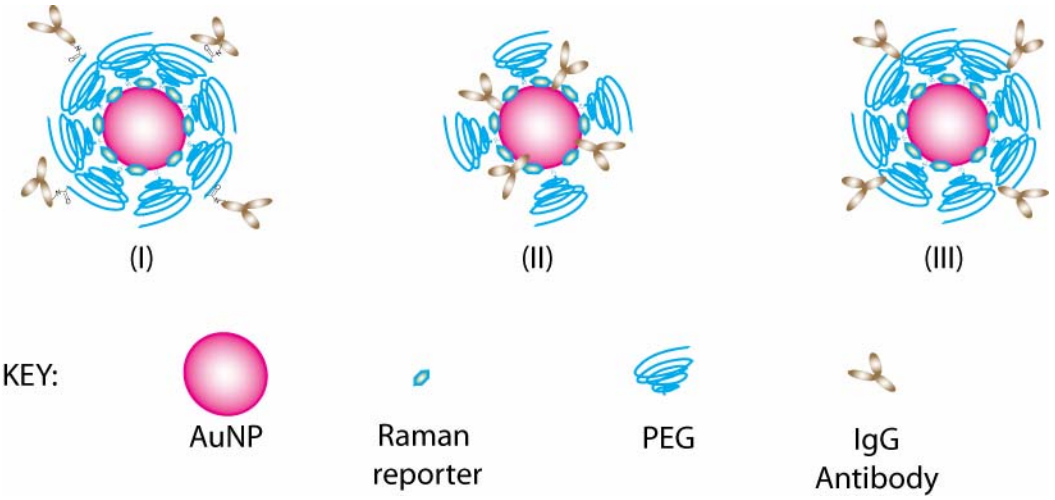

Figure 5.2: Schematic illustration of antibody functionalized PRENTS prepared with antibodies modified by Schemes I, II, or III.

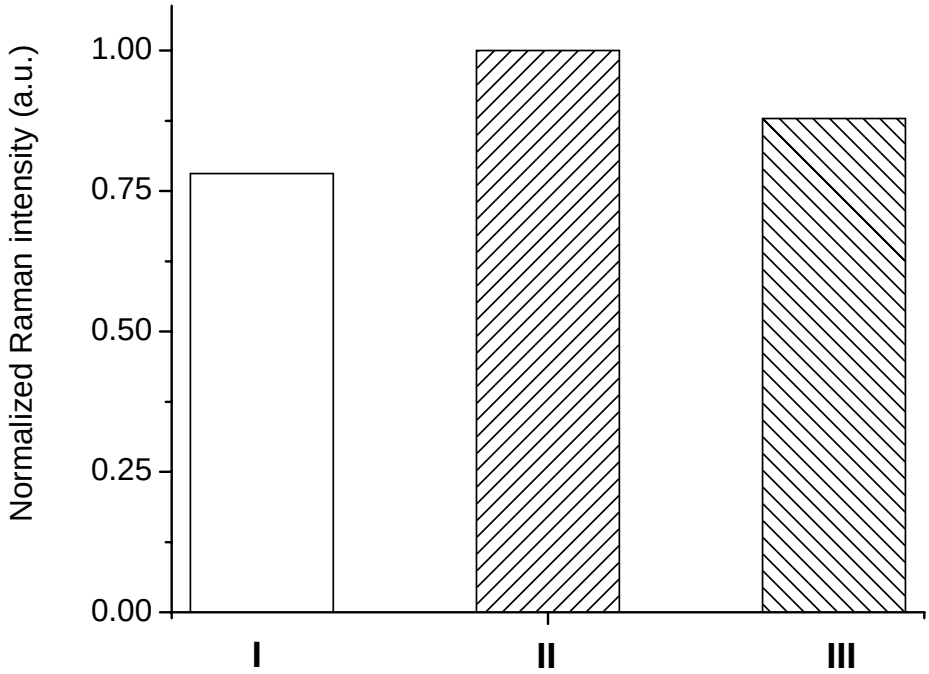

Figure 5.3: Effect of antibody modification method on A-PRENT immunoreactivity. Raman peak intensities of 10^5 antigen coated microspheres incubated with IR792 encoded A-PRENTs (20 pM) functionalized with equal amounts of antibodies modified through Schemes **I**, **II**, or **III**. The IR792 band at 1204 cm^{-1} was used for relative quantification.

three preparations showed a strong yellowish contrast while no contrast was observed from negative control reactions from microspheres that were not coated with antigen. Raman intensity measurements of equal numbers of tagged beads showed that the intensity of the IR792 band at1204 cm^{-1} in the direct preparation immunoreaction (Scheme II) was ~12% greater than the site-specific PEG immunoreaction and ~22% greater than the random PEG immunoreaction (**Figure 5.3)**. The spectral signatures of A-PRENTs prepared with antibodies modified by Schemes I, II, and III were identical (**Figure 5.4)**. These results suggest that mild pre-treatment of antibodies plays a more important role than the presence of a PEG spacer. It is also apparent that the unmodified antibodies in the direct conjugation procedure (scheme II) were not excessively masked or desorbed by PEG-SH nor extensively denatured by the AuNP. Scheme III may prove advantageous in functionalizing PRENTs with carbohydrates and other carbonyl containing targeting ligands that do not form a stable association with AuNPs. For antibody conjugation, the direct method was selected as the preferred procedure for scaled up preparations of A-PRENTs.

Raman-linked immunosorbent assay

To demonstrate that PRENTs are practical optical tags for biomarker quantification we developed a direct Raman-linked immunosorbent assay (RLISA). Rabbit IgG antigens were captured onto a standard glass microscope slide and probed with PRENTs functionalized with anti-rabbit IgG antibodies. From Raman spectral data, dynamic

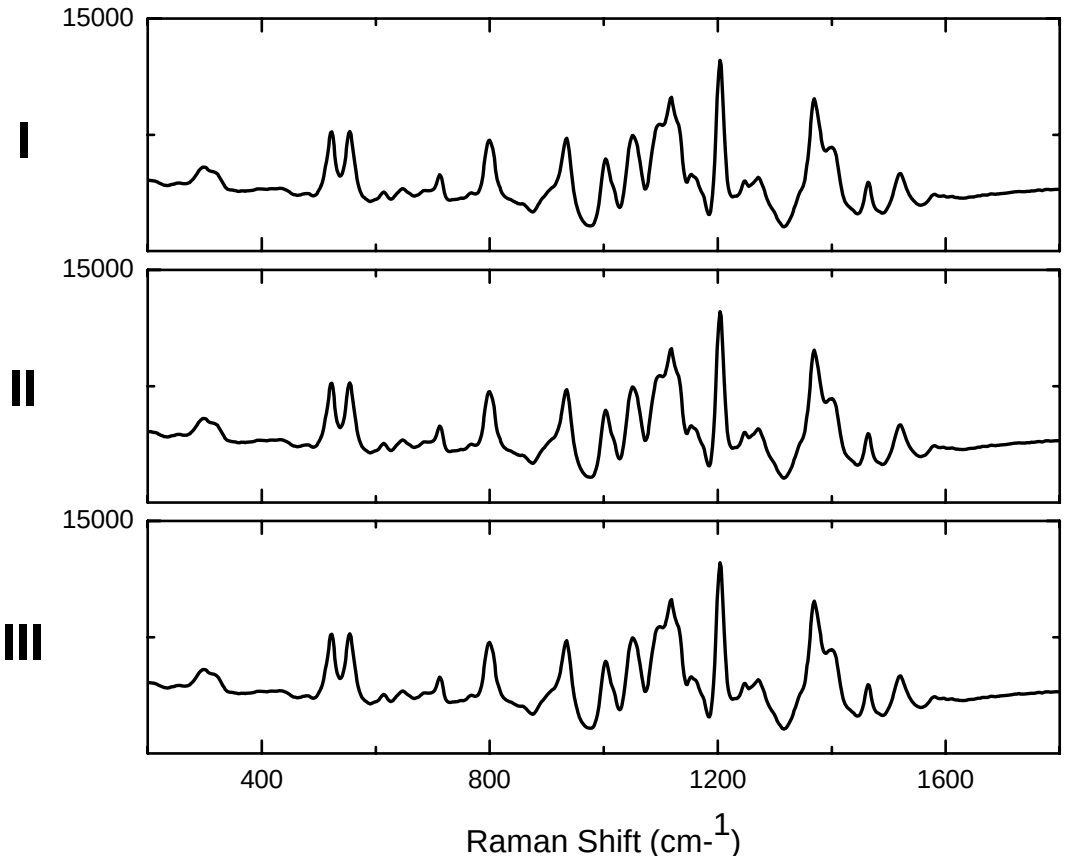

Figure 5.4: Effect of antibody modification method on A-PRENT spectral signature. Raman spectra of equimolar solutions of IR792-encoded A-PRENTs conjugated to antibodies modified by Schemes **I**, **II**, or **III**.

range and determination and detection limits were evaluated and the data were examined for regions of linearity.

In comparison to suspension immunoassay of microspheres, immunoassay on planar solid supports such as chambered glass slides simplifies the binding, washing, and measurement readout steps of multiple immunoreactions performed in parallel. This format takes advantage of the slightly larger PRENTs that are optimized for NIR excitation and detection (**Chapter 4)**. The use of NIR-PRENTs in a suspension assay is more difficult due to their high sedimentation velocity and lower margin of separation between the target support (e.g. microspheres or cells) and unbound PRENTs. In addition, target supports must be must accurately counted to ensure a fair comparison between suspension assays. For some beaded supports this step can be quite onerous. The use of paramagnetic microspheres and magnetic separators streamlined assay steps but were not superior to more traditional glass slide supports. Planar supports are also a better model system for both fixed tissue sections and cell surface tumor antigens in living animals because their antigen targets are anchored within a two-dimensional system. Microsphere/suspension cell assays allow both target and tag to move freely in three dimensions. Both quantitative immunohistochemistry assays and in vivo molecular imaging procedures benefit from tag multivalency. In contrast, multivalency does not confer an advantage for tagging microspheres and suspension cells due to the possibility of aggregating the micron sized targets and confounding the results.[32]

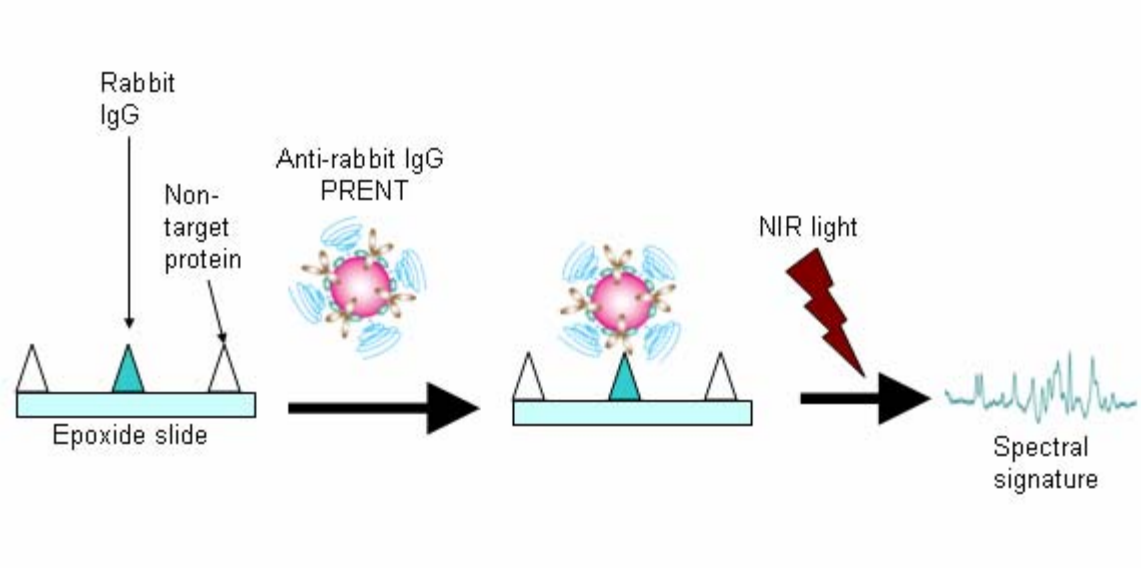

Figure 5.5: Schematic illustration of the Raman-linked immunosorbent assay procedure.

Rabbit IgG was used as a model antigen for the RLISA and was attached to a glass solid support (16-well chamber Lab-Tek chamber slides) covalently via a heterobifunctional cross-linker containing a silane functional group on one end and an epoxide functional group on the other. The binding of rabbit IgG to epoxide-derivatized, aldehyde-derivatized, nitrocellulose-coated, and plain glass slides was compared qualitatively with standard ELISA reagents; epoxide slides produced the strongest and most uniform coating (results not shown). Silanes form a covalent bond with glass and epoxides form covalent bonds with protein thiols and amines at the elevated pH of the incubation buffer (9.6).[30,33] Serial dilutions of rabbit IgG were spotted in individual wells followed by incubation in 1% bovine serum albumin (BSA) to quench unreacted epoxides and block non-specific binding of proteins to the glass surface. After thorough washing, anti-rabbit IgG functionalized IR792-encoded PRENTs were diluted in 1% BSA and added to wells

for incubation. Exhaustive washing and air drying preceded Raman spectral analysis. A schematic of the assay procedure is shown in **Figure 5.5**.

We adhered to proper immunoassay development practices to provide optimized results. Temperature, agitation, incubation time, and immunoreagent concentration have strong effects on assay sensitivity and dynamic range.[34-36] An incubation temperature of 37 ^{o}C was selected for the A-PRENT binding reaction. No loss of Raman signal from IR792-PRENTs was observed when subjected to 37 ^{o}C for 3 h, but 45 ^{o}C exposure caused a slight signal intensity reduction, and 55 ^{o}C exposure caused 100-fold reduction in signal intensity. (The loss of signal is presumably due to IR792 degradation rather than simple dissociation of IR792 and PEG-SH because the intensity decrease was not reversed by lowering temperature to the ambient and the optical absorption spectra of the PRENTs did not change.). The RLISA experiment was kept under vigorous shaking to aid both diffusive and advective transport (convection). Assay wells were kept in high humidity conditions and Parafilm sealed to reduce required volumes. A-PRENT concentration was carefully titrated on supports containing 0 or 10,000 ng/mL rabbit IgG to maximize the difference between total signal and signal due to non-specific binding of A-PRENTs to the protein coated support (**Figure 5.6)**. An A-PRENT concentration of 500 pM provided the optimal signal-to-background ratio under the tested conditions. Results of the rabbit IgG RLISA are shown in **Figure 5.7**. Raman spectra were recorded with a commercial near-infrared Raman microscope (Delta Nu ExamineR). Each data point in the quantitative assay is the mean of ten randomly selected spots in a given well. The

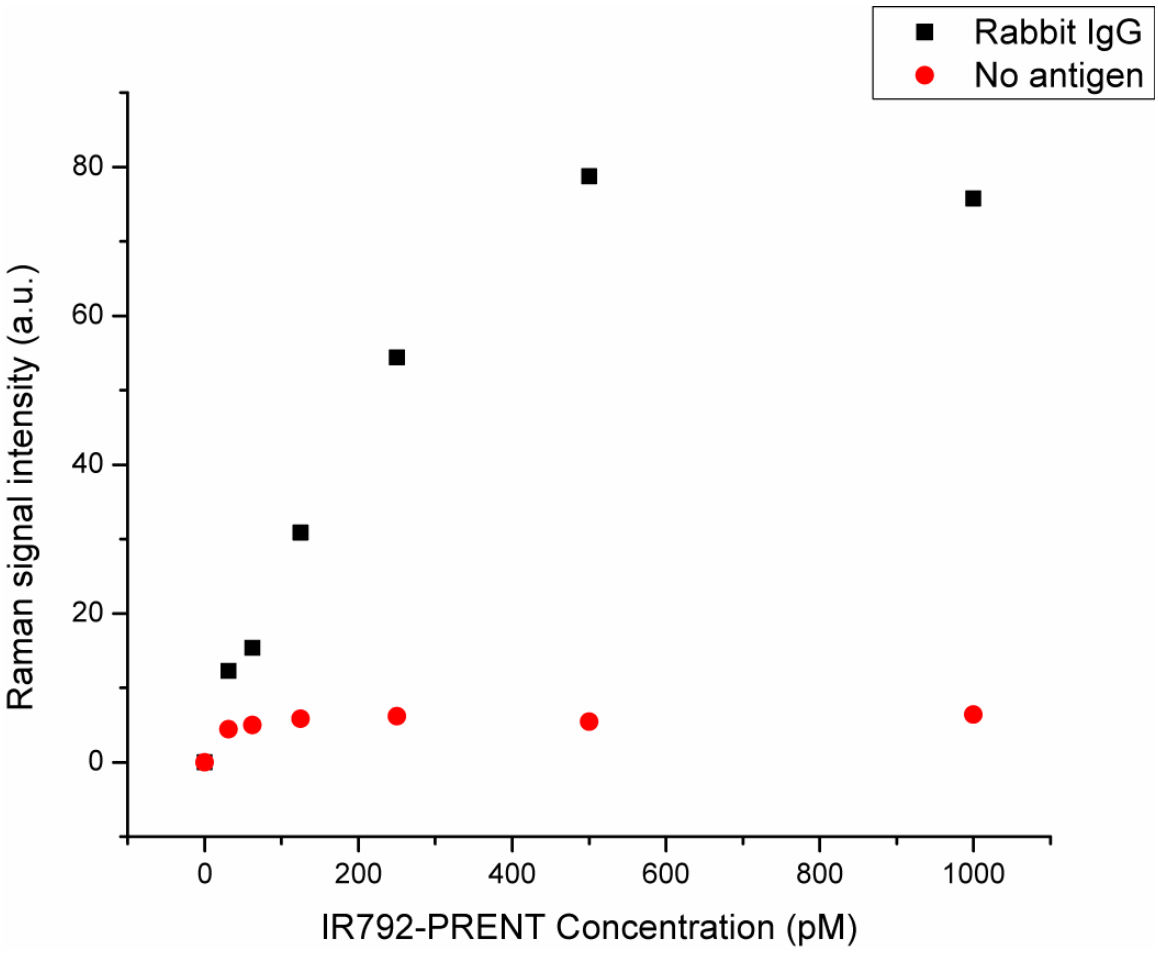

Figure 5.6: Optimization of anti-rabbit IgG PRENT concentration for RLISA. Titration of IR792-encoded Anti-rabbit IgG PRENTs on supports containing rabbit IgG antigen (10,000 ng/mL, black squares) and no antigen (red circles).

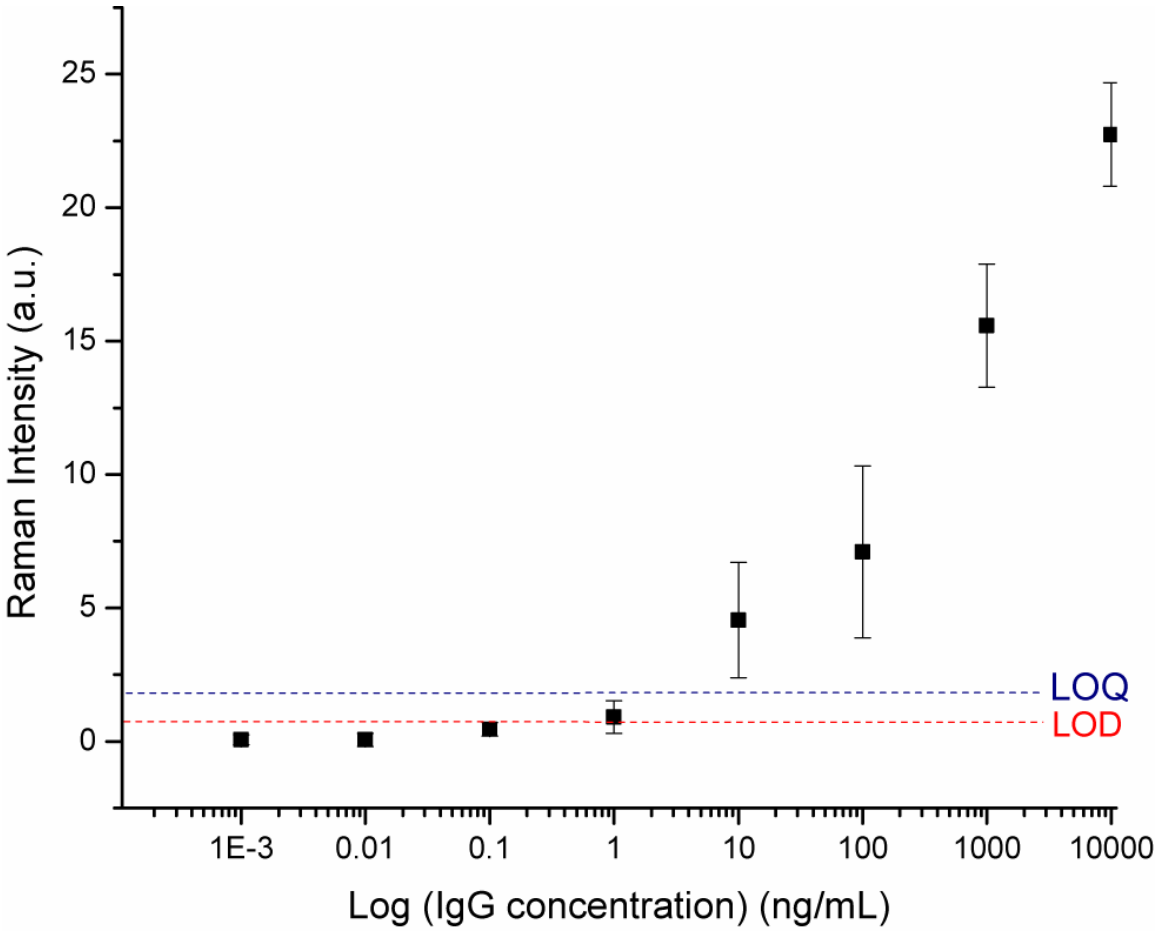

Figure 5.7: Dose response curve for IR792-PRENT detection of rabbit IgG. The baseline-subtracted area under the IR792-PRENT band centered at 1204 cm^{-1} was plotted as a function of added rabbit IgG concentration. The data points are the mean value of ten randomly selected spots in the assay well. The error bars are the standard deviations of signals. The signal values for the limit of detection (LOD) and the limit of quantification (LOQ) are indicated as red and blue lines, respectively. The integration time was 5 seconds for each data point.

error bar is the standard deviation. Based on standard definitions,[37-39] the limit of detection (LOD) was between 0.1 and 1.0 ng/mL and the limit of quantification (LOQ) was between 1.0 and 10.0 ng/ml. The Raman signal increased with tested rabbit IgG concentrations above these values.

Multivariate calibration of PRENTs

Before proceeding with further immunoassay development to determine regions of linearity and assess the assay dynamic range, it is important to determine whether an assumption of linearity is actually valid. To this end, serial dilutions of IR792-encoded PRENTs were examined by Raman microscopy and the data fit to a least squares regression model (**Figure 5.8A**). The dose-response curve was linear over a dynamic range of 1388 above the limit of quantification (LOQ). The Raman signal intensity of the NIR-PRENTs was also a linear function of integration time and laser power (**Figure 5.8B** and **C**), demonstrating that these parameters could be used to further expand the linear dynamic range of detection. Linear unmixing algorithms are commonly used to simultaneously measure the relative abundance of fluorescence probes in mixtures but in practice the analysis is complicated by undesired and uncontrolled spectral changes due to chemical degradation, photobleaching, or fluorescence resonance energy transfer.[40-43] In contrast to most fluorescent optical tags, PRENTs are well-protected from interactions between each other and are chemically and optically-stable under conditions commonly

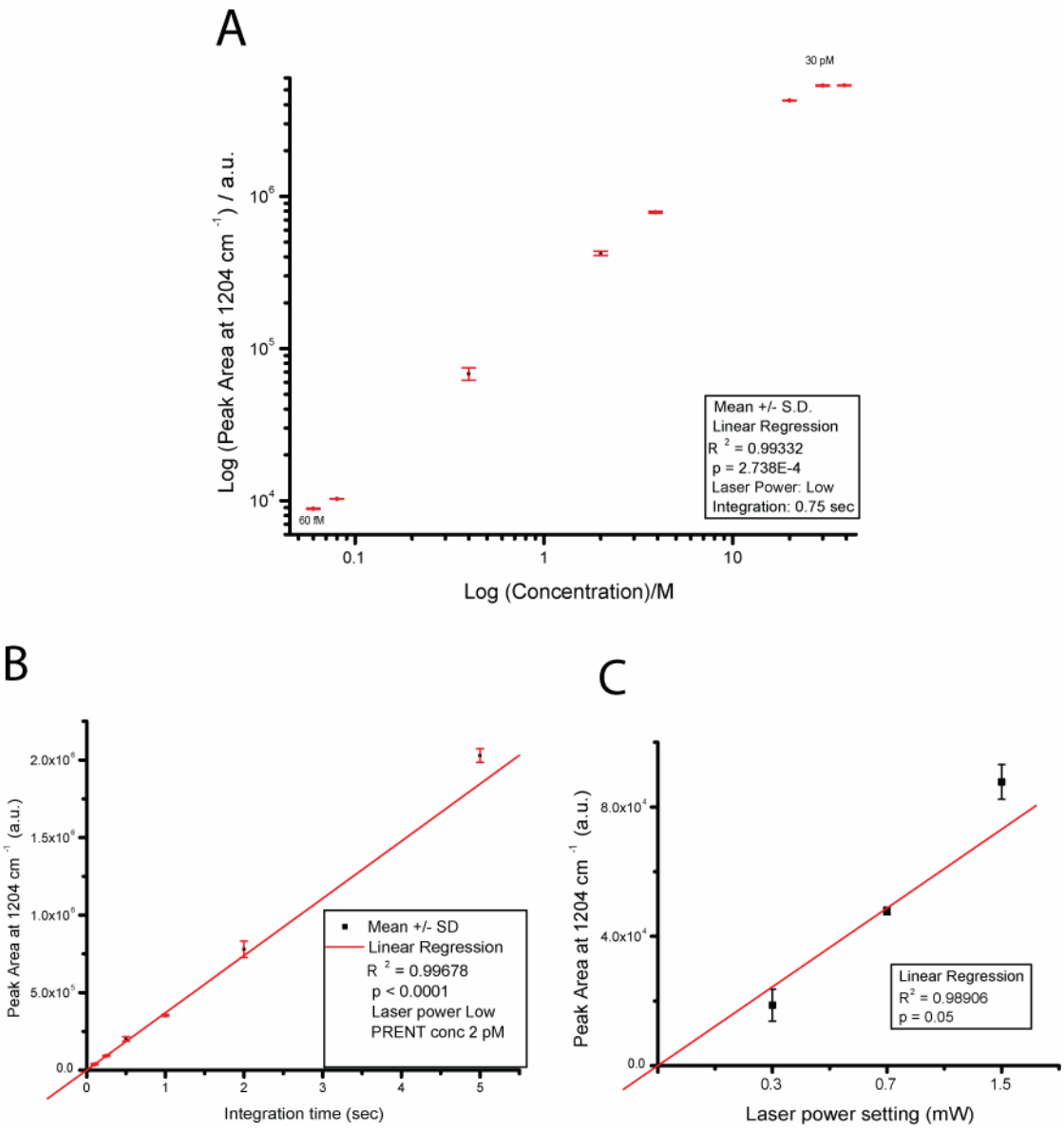

Figure 5.8: Assessment of linearity assumption in PRENT dose-response. Peak intensity of IR792-encoded PRENTs as a function of concentration (**A**), integration time (**B**), and laser power (**C**). Error bars shown are the standard deviations of three replicate measurements taken 10 seconds apart.

encountered in protein detection and cell labeling assays. Error-free linear unmixing would require that a Raman spectrum of a mixture of PRENTs be a simple linear superposition of the spectrum of each PRENT weighted by its relative concentration in the mixture. This is given by

$$M(\nu) = \sum c_i * R_i(\nu) \quad (1)$$

where $M(\nu)$ is the observed Raman spectrum of a sample containing a mixture of PRENTs, $R_i(\nu)$ is the Raman spectrum of a pure solution of PRENT i, and c_i is the relative concentration of PRENT i in the mixture, and ν is energy in wavenumbers (cm^{-1}).

Tests of this linear superposition property were simplified by normalizing the spectral output of each of the six NIR-PRENTs developed in Chapter 4 so that the intensities of their most prominent peaks were approximately equal. This was accomplished through a unique intensity attenuation mechanism that fine-tunes signal intensity via the ratio of Raman reporters to gold nanoparticles (reporter-to-nanoparticle ratio, RNR). For example the maximal intensity of an IR786-PRENT is over ten times as high as the maximal intensity of an IR792-PRENT at 785 nm excitation, but an IR786-PRENT with 4,000 reporters per nanoparticle has approximately the same intensity as an IR792-PRENT with 10,000 reporters per nanoparticle (**Figure 5.9**). In contrast, multiplexed analysis of other types of optical tags such as fluorescent dyes, QDs, and PRPs requires that the end-user take into account the variation of spectral response among tags with different colors or emission spectra.[44,45] In principle, RNR intensity modulation should also be available to other classes of SERS tags such as COINs[20] and GANs[46,47], but it is

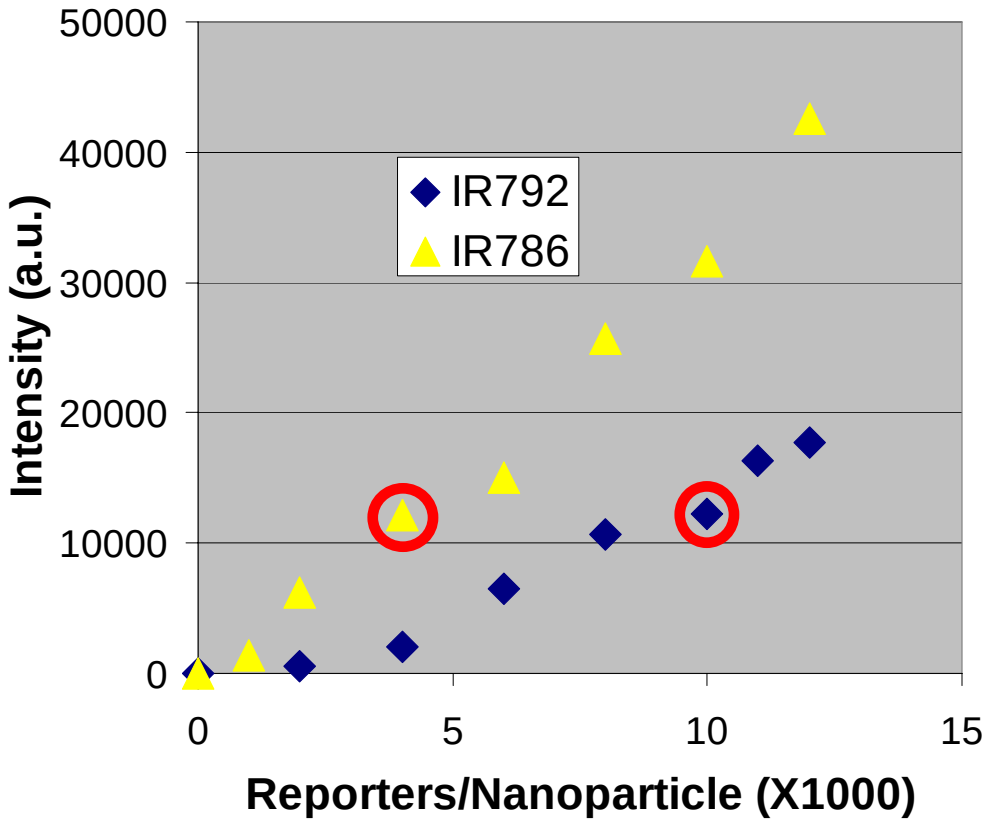

Figure 5.9. Intensity tuning of PRENTs using the reporter to nanoparticle ratio (RNR). Raman peak intensity as a function of RNR for IR792-encoded PRENTs (blue diamonds) and IR786-encoded PRENTs (yellow triangles). Normalized PRENTs used for multivariate calibration are indicated by red circles. The 1204 cm^{-1} peak of IR792 and the 928 cm^{-1} peak of IR786 were used in quantification.

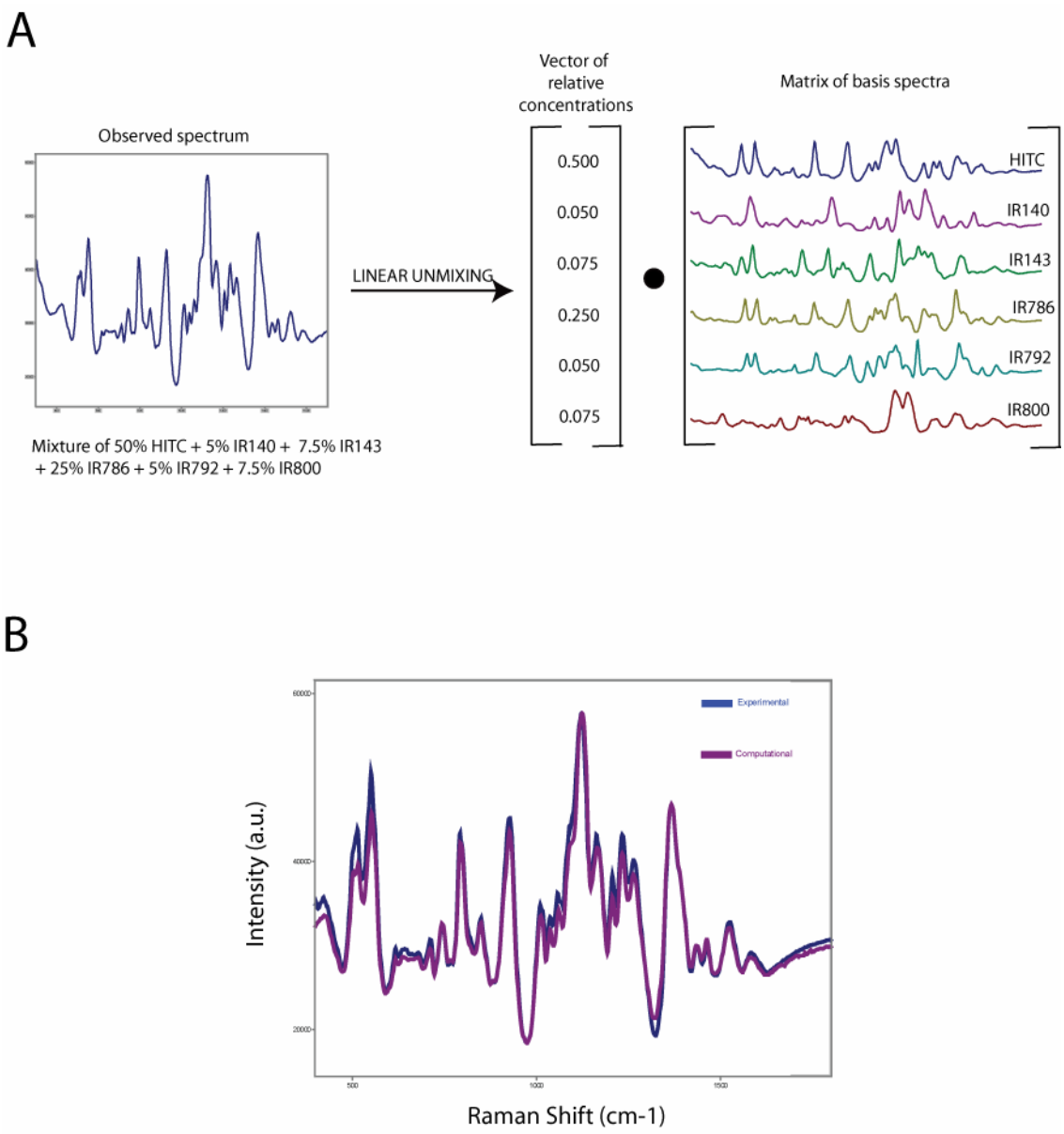

Figure 5.10. Tests of linearity in multivariate Raman signal processing of PRENT mixtures. Results from a linear decomposition of a 6-PRENT computational mixture (**A**) and comparison of a real 6-PRENT mixture (**blue** spectrum) with a computational mixture (**violet** spectrum) of the same six PRENTS at the same relative concentrations (**B**).

unlikely that they can achieve the highly precise attenuation afforded by the relatively straightforward PRENT synthetic protocol. The normalized NIR-PRENTs were verified for univariate linearity with respect to concentration using the procedure described for IR792-encoded PRENTs in **Figure 5.8A**. To determine the validity of the linear superposition assumption for multiplexed PRENT analysis, Raman spectra of samples containing a single population of PRENTs were recorded and a multivariate ordinary least squares model with non-negativity constraint[48-50] was constructed in MATlab software. The soundness of this model was verified by input of various computational mixtures containing all six individual PRENT spectra. Despite substantial spectral overlap, the algorithm unmixed the signal 100% correctly in every case tested. An example is shown in **Figure 5.10A**. A Raman spectrum for a real sample containing an equimolar concentration of all six NIR-PRENTs matched nearly exactly with the computational sum of the spectra of solutions containing a single PRENT of equivalent concentration (**Figure 5.10B**), verifying linear superposition and demonstrating the absence of interactions between different PRENTs. The discrepancy between the mixed PRENT spectrum and the sum of the individual PRENT spectra is most likely due to a combination of pipetting errors, slide surface variation, laser power fluctuations, and the absence of an internal standard. The error of the six-PRENT mixture was small in comparison to most fluorescent tags but large enough to make linear unmixing by ordinary least squares methods inaccurate. However, in real samples containing combinations of two different PRENTs, this approach was very accurate. A sample containing 50.0% IR792-PRENTs and 50.0% IR786-PRENTs was unmixed as 51.4% and 48.6%, respectively (**Figure 5.11**).

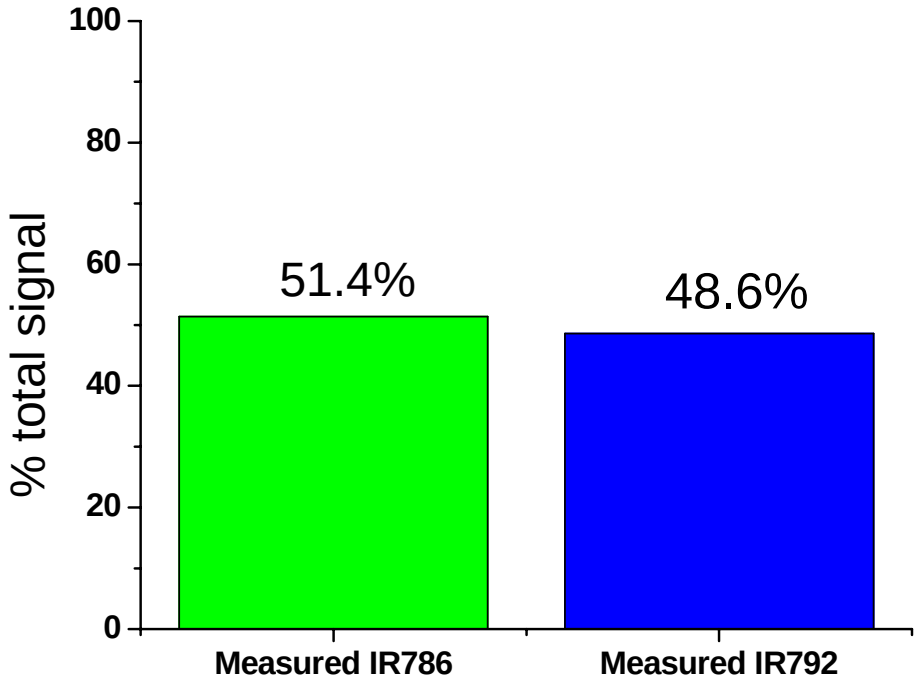

Figure 5.11. Linear unmixing of a sample containing 50% IR786-encoded PRENTs and 50% IR792-encoded PRENTs.

5.3 Conclusions

We have demonstrated that antibody-conjugated PRENTs can quantify proteins in a proof-of-principle slide-based Raman-linked immunosorbent assay (RLISA). The LOD is in the low ng/mL range with the current experimental approach. Further LOD reduction could be achieved with automated measurements and more comprehensive optimization of assay parameters. Experiments have been planned to construct a sandwich RLISA and evaluate assay performance with disease-relevant proteins such as prostate specific antigen in human serum. We showed that ordinary least squares unmixing algorithms can be used to determine the concentrations of two-PRENT mixtures. Accurate discrimination of assays containing more than two PRENTs could be achieved with more sophisticated statistical methods that can better handle the multiple sources of noise that introduce calibration errors (e.g. partial least squares, principle components analysis).

5.4 Materials and Methods

Materials

Ultrapure water (18 MΩ cm^{-1}) was used to prepare all aqueous solutions. The following materials were used without further purification: succinimidyl 4-hydrazidoterephthalate hydrochloride (SHTH) (Pierce Biotechnology); HS-PEG-NH_2 and HS-PEG-OCH_3 (MW ~ 5,000 Da, Rapp Polymere), rabbit anti-horseradish peroxidase (HRP) antibody, bovine serum albumin, purified rabbit IgG, purified mouse IgG, goat anti-mouse IgG antibody, goat anti-rabbit IgG antibody (Jackson Immuno); Sephadex G-25 columns (GE Healthcare), Vivaspin 50K centrifugal concentrator (Sartorius Stedim Biotech); streptavidin coated silica microspheres (Bangs Labs); biotinylated horseradish peroxidase (HRP-biotin) (Biomeda); 16-well Lab-Tek chamber slide (Nunc). All other reagents were obtained from Sigma-Aldrich at the highest purity available.

All experiments were performed at room temperature unless otherwise specified.

Measurements

Optical absorption spectra were recorded on a Shimadzu UV-2401 spectrometer. Disposable polyacryl cuvettes with 1cm optical path length were used in all UV-Vis measurements. Raman scattering spectra were recorded with an ExamineR Raman microscope (DeltaNu LLC) equipped with a 785 nm diode laser. The laser power was attenuated with neutral density filters. Size exclusion chromatography was performed on an AKTAPrime Plus fast protein liquid chromatography (FPLC) device equipped with a Superose 6 column (GE Healthcare). Samples were filtered through a 0.2 micron PVDF filter and the flow rate was 0.5 mL/min.

Analysis of spectral data

Raman bands were separated from SERS continuum and sample background fluorescence using a Fourier transform method (Examine R software, Delta Nu) or by manual construction of baselines in Grams A/I software (Thermo Scientific). Peak area was calculated by integrating the spectral region between the closest local minimum to the left and the closest local minimum to the right of the peak. Integration was performed by the trapezoidal method. Peak height was calculated by subtracting the maximal value of a peak by the mean of its two neighboring minima. Univariate calibration curves were constructed and fit in Origin software (Origin Lab Corp). Multivariate analysis was performed in Matlab software (The Mathworks, Inc) using a previously described algorithm.[49,50] Briefly, the Raman spectra of single PRENT solutions were stored in 1024-element basis vectors of intensity values corresponding to each wavenumber measured. Each PRENT basis vector was incorporated as a row of a design matrix **B**. The spectrum of the sample containing a mixture of different PRENTs was stored in a 1024-element vector **m**. Since $\mathbf{m} = \mathbf{c} \bullet \mathbf{B} + \boldsymbol{\varepsilon}$, where **c** is a vector containing the relative concentrations of each PRENT in the mixture and $\boldsymbol{\varepsilon} = \mathbf{B} \bullet \mathbf{c}$ is the vector containing the model error terms , the concentration vector **c** is the pseudoinverse of **B** given by

$$\mathbf{c} = (\mathbf{B}^{\mathbf{T}} \bullet \mathbf{B})^{-1} \bullet \mathbf{B}^{\mathbf{T}} \bullet \mathbf{m} \qquad \textbf{(2)}$$

PEGylation of IgG amine groups

Rabbit anti-HRP polyclonal antibody was modified by PEG-SATA as described in **Chapter 3**.

PEGylation of IgG carbohydrate residues.

PEG-SH was grafted to the polysaccharide chains of antibodies by minor modifications of literature procedures.[51] HS-PEG-NH2 was reacted with 10-fold molar excess of SHTH in 100 mM carbonate-bicarbonate buffer (pH 9.6) for 2h in a polypropylene tube to form HS-PEG-$NHNH_2$. Reaction completion was determined with fluorescamine. HS-PEG-NH_2 fluoresced under UV excitation before but not after reaction with SHTH. Reaction selectivity for amines and not thiols was verified with positive DTNB reaction. IgG was mixed with sodium meta-periodate (1000-fold molar excess) and protected from light. After 30 min incubation, the oxidation reaction was quenched with glycerol. A portion of the reaction mixture that did not receive glycerol was added to Purpald solution (15 mg/mL in 1 N NaOH) to verify aldehyde formation. The oxidized IgG sample and oxidized glycerol (positive control) exhibited a purple color in the presence of Purpald whereas unoxidized IgG did not. Oxidized IgG and HS-PEG-$NHNH_2$ were purified by size exclusion chromatography (Sephadex G-25). Both antibody and polymer were eluted with citrate buffered saline (pH 6.0, 150 mM NaCl). IgG fractions were identified by UV-vis absorption spectroscopy and concentration with a Vivaspin 50K centrifugal concentrator the IgG concentration was estimated by absorbance at 280 nm (extinction coefficient $\sim 210{,}000\ M^{-1}\ cm^{-1}$).[21] HS-PEG-$NHNH_2$ concentration was estimated with DNTB. Purified HS-PEG-$NHNH_2$ and oxidized IgG and were reacted overnight at 5:1 molar ratio with shaking in a polypropylene tube, followed by reduction with an excess of sodium cyanoborohydride ($NaBH_3CN$) for 1h. IgG-PEG-SH was purified from $NaBH_3CN$ by size exclusion. Increased retention time

of the reaction product on FPLC compared to HS-PEG-NNH_2 and oxidized IgG verified the success of the conjugation.

Preparation of A-PRENTs

AuNPs were synthesized and complexed with IR792 and IR786 reporters as described in Chapter 4. AuNP-reporter complexes were thoroughly mixed with IgG or IgG-PEG-SH (prepared by Schemes I or III) for 2 hours at a molar ratio of 1,000 IgG : 1 AuNP, then with 50,00 PEG-SH per AuNP for 10 min. Tween-20 was added to the solution to 0.05% and the A-PRENT was purified by 5 rounds of centrifugation at 1000g and resuspension in 0.05% Tween-20 in PBS. Serial dilutions of the A-PRENT prior to purification were used to construct a linear calibration curve of absorbance at 550 nm as a function of the AuNP concentration. The stock AuNP concentration was provided by the manufacturer. A-PRENT concentrations were estimated by assuming that each A-PRENT conjugate contained one AuNP.

Bead binding assay

HRP functionalized beads were prepared by mixing HRP-biotin with streptavidin coated silica microspheres (4.82 micron mean diameter) at a ratio of 10^7 HRP per microsphere for 30 min. The HRP-beads were washed by five rounds of centrifugation in 1% BSA / 0.05% Tween-20 in PBS. The HRP beads were concentrated and mixed with A-PRENTs (20 pM, diluted in 1% BSA). The tagging reaction was incubated for 1.5 h with vigorous shaking, and then beads were washed by five rounds of centrifugation in

0.05% Tween-20. Beads were concentrated and counted in a hemacytometer before analysis by reflected light microscopy and Raman spectroscopy.

Raman-linked immunosorbent assay

A 16-well chamber slide was washed with HPLC grade methanol. 3-Glycidyloxypropyltrimethoxysilane (2% v/v in methanol, prepared fresh) was added to each well and incubated at 30 min with shaking. The wells were washed exhaustively with methanol, then water and air dried under a stream of argon. The epoxide-coated slides were used immediately or stored under inert gas. Rabbit IgG diluted in bicarbonate buffered saline (BBS, pH 9.6, 150 mM NaCl) was added to the wells and incubated for 1h at 37 ^{o}C with shaking in a humid chamber. The wells were blocked in 1% BSA in BBS for 15 min at 37 ^{o}C with shaking in a humid chamber. After washing in 0.05% Tween-20 in PBS, Anti-rabbit IgG functionalized A-PRENT was added to the well and incubated for 2h at 37 ^{o}C with shaking in a humid chamber. Excess PRENT was removed and the wells were washed in PBS-T, then in water. Chambers were removed and the slide was air dried before analysis by Raman spectroscopy.

The signal limit of detection (LOD) is defined as

$$\overline{x}_B + 3.29 \times \sigma_B \quad (3)$$

Where $\overline{x}_B$ is the mean of the blank and σ_B is the standard deviation of the blank. The blank is defined as an immunosorbent assay support containing no antigens and subjected to the exact same assay conditions as the antigen standards used to construct the calibration curve. The signal limit of quantification (LOQ) is defined as

$$\overline{x}_B + 10 \times \sigma_B \quad (4)$$

5.5 References

1. Yu H, Diamandis EP, Prestigiacomo AF, Stamey TA. Ultrasensitive Assay of Prostate-Specific Antigen Used for Early Detection of Prostate-Cancer Relapse and Estimation of Tumor-Doubling Time After Radical Prostatectomy. *Clinical Chemistry*. 1995;41(3):430-434.

2. Melegos DN, Diamandis EP. Is Prostate-Specific Antigen Present in Female Serum? *Clin Chem*. 1998;44(3):691-692.

3. Nam JM, Thaxton CS, Mirkin CA. Nanoparticle-based bio-bar codes for the ultrasensitive detection of proteins. *Science*. 2003;301(5641):1884-1886.

4. Georganopoulou DG, Chang L, Nam J, et al. Nanoparticle-based detection in cerebral spinal fluid of a soluble pathogenic biomarker for Alzheimer's disease. *Proceedings of the National Academy of Sciences of the United States of America*. 2005;102(7):2273-2276.

5. Etzioni R, Urban N, Ramsey S, et al. The case for early detection. *Nature Reviews Cancer*. 2003;3(4):243-252.

6. Maddalena A, Papassotiropoulos A, Muller-Tillmanns B, et al. Biochemical Diagnosis of Alzheimer Disease by Measuring the Cerebrospinal Fluid Ratio of Phosphorylated tau Protein to beta-Amyloid Peptide42. *Arch Neurol*. 2003;60(9):1202-1206.

7. Chen S, Xu Y, Ip MP. Electrochemical Enzyme Immunoassay for Serum Prostate-Specific Antigen at Low Concentrations. *Clin Chem*. 1997;43(8):1459-1461.

8. Zhang Z, Barnhill SD, Zhang H, et al. Combination of multiple serum markers using an artificial neural network to improve specificity in discriminating malignant from benign pelvic masses. *Gynecologic Oncology*. 1999;73(1):56-61.

9. Woolas RP, Conaway MR, Xu FJ, et al. Combinations of Multiple Serum Markers Are Superior to Individual Assays for Discriminating Malignant from Benign Pelvic Masses. *Gynecologic Oncology*. 1995;59(1):111-116.

10. Kitano H. Cancer as a robust system: implications for anticancer therapy. *Nat Rev Cancer*. 2004;4(3):227-235.

11. Banholzer M, Millstone J, Qin L, Mirkin C. Rationally designed nanostructures for surface-enhanced Raman spectroscopy. *Chemical Society Reviews*. 2008;37(5):885-897.

12. Rosi NL, Mirkin CA. Nanostructures in Biodiagnostics. *Chem. Rev.* 2005;105(4):1547-1562.

13. Moskovits M. Surface-enhanced Raman spectroscopy: a brief retrospective. *Journal of Raman Spectroscopy*. 2005;36(6-7):485-496.

14. Kneipp J, Kneipp H, Kneipp K. SERS - a single-molecule and nanoscale tool for bioanalytics. *Chemical Society Reviews*. 2008;37(5):1052-1060.

15. Porter M, Lipert R, Siperko L, Wang G, Narayanana R. SERS as a bioassay platform: fundamentals, design, and applications. *Chemical Society Reviews*. 2008;37(5):1001-1011.

16. Grubisha D, Lipert R, Park H, Driskell J, Porter M. Femtomolar detection of prostate-specific antigen: An immunoassay based on surface-enhanced Raman scattering and immunogold labels. *Analytical Chemistry*. 2003;75(21):5936-5943.

17. Driskell J, Kwarta K, Lipert R, et al. Low-level detection of viral pathogens by a surface-enhanced Raman scattering based immunoassay. *Analytical Chemistry*. 2005;77(19):6147-6154.

18. Xu S, Ji X, Xu W, et al. Immunoassay using probe-labelling immunogold nanoparticles with silver staining enhancement via surface-enhanced Raman scattering. *ANALYST*. 2004;129(1):63-68.

19. Gong J, Jiang J, Yang H, et al. Novel dye-embedded core-shell nanoparticles as surface-enhanced Raman scattering tags for immunoassay. *Analytica Chimica Acta*. 2006;564(2):151-157.

20. Su X, Zhang J, Sun L, et al. Composite organic-inorganic nanoparticles (COINs) with chemically encoded optical signatures. *Nano Letters*. 2005;5(1):49-54.

21. Loebke C, Sueltmann H, Schmidt C, et al. Infrared-based protein detection arrays for quantitative proteomics. *Proteomics*. 2007;7(4):558-564.

22. Zhao XY, Shippy SA. Competitive immunoassay for microliter protein samples with magnetic beads and near-infrared fluorescence detection. *Analytical Chemistry*. 2004;76(7):1871-1876.

23. Aubin JE. Autofluorescence of Viable Cultured Mammalian-Cells. *Journal of Histochemistry & Cytochemistry*. 1979;27(1):36-43.

24. Zhao XY, Kottegoda S, Shippy SA. Solid-phase immunoassay detection of peptides from complex matrices without a separation. *Analyst*. 2003;128(4):357-362.

25. Patonay G, Antoine MD. Near-Infrared Fluorogenic Labels - New Approach to an Old Problem. *Analytical Chemistry*. 1991;63(6):A321-A326.

26. Hirsch LR, Jackson JB, Lee A, Halas NJ, West J. A whole blood immunoassay using gold nanoshells. *Analytical Chemistry*. 2003;75(10):2377-2381.

27. Ulman A. Formation and Structure of Self-Assembled Monolayers. *Chem. Rev.* 1996;96(4):1533-1554.

28. Brewer SH, Glomm WR, Johnson MC, Knag MK, Franzen S. Probing BSA binding to citrate-coated gold nanoparticles and surfaces. *Langmuir*. 2005;21(20):9303-9307.

29. Rodwell JD, Alvarez VL, Chyi L, et al. Site-Specific Covalent Modification of Monoclonal-Antibodies - Invitro and Invivo Evaluations. *Proceedings of the National Academy of Sciences of the United States of America*. 1986;83(8):2632-2636.

30. Hermanson GT. *Bioconjugate Techniques*. San Diego: Academic Press; 1996.

31. Zhi ZL, Powell AK, Turnbull JE. Fabrication of carbohydrate microarrays on gold surfaces: Direct attachment of nonderivatized oligosaccharides to hydrazide-modified self-assembled monolayers. *Analytical Chemistry*. 2006;78(14):4786-4793.

32. Zhelev Z, Ohba H, Bakalova R, et al. Fabrication of quantum dot-lectin conjugates as novel fluorescent probes for microscopic and flow cytometric identification of leukemia cells from normal lymphocytes. *Chemical Communications*. 2005;(15):1980-1982.

33. Schena M ed. *Protein Microarrays*. Sudbury, MA: Jones and Bartlett; 2005.

34. Wild D ed. *The Immunoassay Handbook*. 3rd ed. Elsevier Science; 2005.

35. Kusnezow W, Syagailo YV, Ruffer S, et al. Optimal design of microarray immunoassays to compensate for kinetic limitations - Theory and experiment. *Molecular & Cellular Proteomics*. 2006;5(9):1681-1696.

36. Squires TM, Messinger RJ, Manalis SR. Making it stick: convection, reaction and diffusion in surface-based biosensors. *Nature Biotechnology*. 2008;26(4):417-426.

37. Currie L. Nomenclature in Evaluation of Analytical Methods Including Detection and Quantification Capabilities (iupac Recommendations 1995). *Pure and Applied Chemistry*. 1995;67(10):1699-1723.

38. Currie LA. Limits for Qualitative Detection and Quantitative Determination - Application to Radiochemistry. *Analytical Chemistry*. 1968;40(3):586-&.

39. Long G, Winefordner J. Limit of Detection. *Analytical Chemistry*. 1983;55(7):A712-&.

40. Zimmermann T, Rietdorf J, Pepperkok R. Spectral imaging and its applications in live cell microscopy. *Febs Letters*. 2003;546(1):87-92.

41. Garini Y, Young IT, McNamara G. Spectral imaging: Principles and applications. *Cytometry Part A*. 2006;69A(8):735-747.

42. Gammon STM, Leevy WM, Gross S, Gokel GW, Piwnica-Worms D. Spectral unmixing of multicolored bioluminescence emitted from heterogeneous biological sources. *Analytical Chemistry*. 2006;78(5):1520-1527.

43. Thaler C, Vogel S. Quantitative linear unmixing of CFP and YFP from spectral images acquired with two-photon excitation. *Cytometry Part A*. 2006;69A(8):904-911.

44. Ghazani A, Lee J, Klostranec J, et al. High throughput quantification of protein expression of cancer antigens in tissue microarray using quantum dot nanocrystals. *Nano Letters*. 2006;6(12):2881-2886.

45. Xing Y, Chaudry Q, Shen C, et al. Bioconjugated quantum dots for multiplexed and quantitative immunohistochemistry. *Nat. Protocols*. 2007;2(5):1152-1165.

46. Mulvaney SP, Musick MD, Keating CD, Natan MJ. Glass-coated, analyte-tagged nanoparticles: A new tagging system based on detection with surface-enhanced Raman scattering. *Langmuir*. 2003;19(11):4784-4790.

47. Doering WE, Nie SM. Spectroscopic tags using dye-embedded nanoparticies and surface-enhanced Raman scattering. *Analytical Chemistry*. 2003;75(22):6171-6176.

48. Pelletier MJ. Quantitative analysis using Raman spectrometry. *Applied Spectroscopy*. 2003;57(1):20A-42A.

49. Shafer-Peltier K, Haka A, Motz J, et al. Model-based biological Raman spectral imaging. *Journal of Cellular Biochemistry*. 2002:125-137.

50. Haka A, Shafer-Peltier K, Fitzmaurice M, et al. Diagnosing breast cancer by using Raman spectroscopy. *Proceedings of the National Academy of Sciences of the United States Of*. 2005;102(35):12371-12376.

51. Larson RS, Menard V, Jacobs H, Kim SW. Physicochemical characterization of poly(ethylene glycol)-modified anti-GAD antibodies. *Bioconjugate Chemistry*. 2001;12(6):861-869.